EXTREME TEMPERATURE SENSING USING BRILLOUIN SCATTERING IN OPTICAL FIBERS

THÈSE N^{O} 2728 (2003)

PRÉSENTÉE À LA FACULTÉ DES SCIENCES ET TECHNIQUES DE L'INGÉNIEUR

SECTION D'ÉLECTRICITÉ

POUR L'OBTENTION DU GRADE DE DOCTEUR ÈS SCIENCES

PAR

Alexandre FELLAY

ingénieur physicien diplômé EPF
de nationalité suisse et originaire de Bagnes (VS)

acceptée sur proposition du jury:

Prof. Ph. Robert, directeur de thèse
Prof. M. Ilegems, rapporteur
Dr E. Picholle,rapporteur
Dr W. Scandale, rapporteur
Dr L. Thévenaz, rapporteur

Lausanne, EPFL
2003

Dorer des éléphants est la vraie fonction de l'homme. On ne le comprend jamais trop vite, on ne commence jamais assez tôt.

Alexandre Vialatte

Abstract

Stimulated Brillouin scattering in silica-based optical fibers may be considered from two different and complementary standpoints. For a physicist, this interaction of light and pressure wave in a material, or equivalently in quantum theory terms between photons and phonons, gives some glimpses of the atomic structure of the solid and of its vibration modes. For an applied engineer, the same phenomenon may be put to good use as a sensing mechanism for distributed measurements, thanks to the dependence of the scattered light on external parameters such as the temperature, the pressure or the strain applied to the fiber.

As far as temperature measurements are concerned, Brillouin-based distributed sensors have progressively gained wide recognition as efficient systems, even if their rather high cost still restricts the number of their applications. Yet they are generally used in a relatively narrow temperature range around the usual ambient temperature; in this domain, the frequency of the scattered light increases linearly with the increase in temperature.

The extension of this range toward higher (up to 800°C) and lower (down to 1 K) temperature is the main aim of this thesis. In both cases, our measurements on various fiber samples show that the aforementioned linearity does not hold. Most notably, the characteristics of Brillouin scattering at low and very low temperature are strikingly different from those observed under normal conditions; they are directly related to the disordered nature of the silica that constitutes the fiber, what motivates the large place we here devote to the physics of amorphous solids.

Despite the observed nonlinearities, our results demonstrate the feasibility of thermometry based on Brillouin scattering over the full investigated temperature range. We can thus swap in the last part of this work the physicist's point of view for that of an engineer and present the setup and the performances of a sensor, or rather of a whole family of sensors we have tested and improved in the course of the last few years; moreover, some real measurement examples are given. Finally, we propose some possibilities of further enhancement, that remain right now at the preliminary stage of their development.

Version abrégée

La diffusion Brillouin stimulée dans les fibres optiques à base de silice peut être considérée selon deux points de vue différents mais complémentaires. Pour le physicien, cette interaction entre lumière et ondes de pression dans un matériau, ou entre photons et phonons si l'on préfère s'exprimer en termes quantiques, ouvre des perspectives sur la structure de la matière et sur ses modes de vibration. Pour l'ingénieur, elle est un phénomène dont on peut tirer avantage pour effectuer des mesures distribuées, puisque la fréquence de la lumière diffusée varie en fonction de paramètres externes à la fibre comme la température, la pression ou les forces exercées sur elle.

En ce qui concerne la mesure de la température, les capteurs distribués basés sur l'effet Brillouin ont peu à peu acquis le statut de technique reconnue. Cependant, ils ne sont en général mis en oeuvre que sur une plage de températures relativement restreinte, autour de la température ambiante, où la fréquence diffusée augmente linéairement quand la température monte.

L'extension de cette gamme de températures vers le haut (800°C) et vers le bas (1 K) est l'objectif principal de cette thèse. Dans les deux cas, nos mesures sur différents échantillons de fibres montrent que le comportement linéaire disparaît. Les caractéristiques de la diffusion Brillouin à basses et très basses températures en particulier sont très différentes de celles observées sous conditions normales; elles sont directement liées à la nature désordonnée de la silice constituant les fibres, ce qui motive la place importante donnée ici à la physique des matériaux amorphes.

Dans la dernière partie de ce travail, nous troquons les lunettes du physicien pour celles de l'ingénieur et présentons la construction, le mode de fonctionnement et les performances d'un capteur, ou mieux d'une famille de capteurs testés et améliorés au cours des dernières années, ainsi que des exemples concrets de mesures aussi bien dans le domaine usuel de températures qu'en cryogénie. Enfin, deux pistes possibles de développement, sur lesquelles le travail n'en est encore qu'à la phase préliminaire, seront proposées.

TABLE OF CONTENTS

Introduction

When Léon Brillouin first suggested in 1922 that density fluctuations in condensed matter could cause light scattering [1], he could not foresee the practical impact of his theoretical work. Actually the interest in the scientific community was initially rather limited (admittedly, this topic could appear secondary with respect to the fundamental developments occurring in all the fields of physics in this period) and he had to wait for ten years until Debye experimentally verified [2] his predictions. Then spontaneous Brillouin scattering took a modest place in the textbooks at the intersection of optics and solid-state physics, while its limited applications seemed fated to never venture out of the laboratories.

Yet the march of science, albeit essentially cumulative, has its twists and turns : apparently unrelated progress can often lead to the revival of a semi-lethargic domain. This is most spectacularly exemplified by the advent of lasers in the early sixties. The sudden availability of high-intensity coherent lightwaves opened innumerable new directions of research. Among them, nonlinear optics attracted much attention. In this context, stimulated Brillouin scattering was experimentally observed in crystals [3].

A second technological breakthrough followed, with the invention of low-loss optical fibers made of silica in the early seventies. Brillouin scattering became then for the first time a subject of practical concern : it turned out that it was the major limiting factor in the optical power that can be carried by a fiber. Partly motivated by the necessity of tackling this limit, and partly with the intention of putting Brillouin scattering into use as a sensing mechanism, people began to thoroughly study the phenomenon [4, 5].

The subfield of Brillouin sensors grew a little bit later, beginning in the second half of the eighties. The basic idea is here to take advantage of the dependence of Brillouin scattering on external parameters as well as of the guiding properties of

the fiber to make distributed measurements [6, 7]. Our group has been involved with that kind of research for the last twelve years, developing setups and testing them in numerous field experiments.

The present thesis is the continuation of a collective work that already led to two Ph.D. theses [8, 9].[1] Actually, it may be considered as the closing volume of a research cycle. We do not assert that nothing is left to do; nevertheless, as things look now, further enhancements of our setup require industrial development and optimization rather than academic research. On the other hand, possible alternative ways of using Brillouin scattering exist but they imply a new start nearly from scratch.

With respect to the previous theses, the originality of this work is double :

- It highlights the characteristics of Brillouin scattering at so-called extreme temperatures. By ‘extreme’, we mean either the temperatures in the cryogenic range down to nearly absolute 0 K, or the temperatures up to the point where the very existence of the optical fibers is impossible (that is where they lose their mechanical integrity, or at least their guiding properties).

- It emphasizes the physics of silica. The characteristics of Brillouin scattering are rooted in the disordered nature of the glass constituting the fiber, and we will try to clarify some aspects of this relation. A complete explanation will remain out of reach, though, as the physics of disordered systems still keeps many open questions. Paradoxically enough, satisfying theories are available for the experimentally harder to reach low-temperature domain, while the behavior at ambient temperature remains largely unexplained.

The deepening of our knowledge concerning Brillouin scattering at extreme temperature in fibers is a prerequisite for the development of distributed sensing applications under these conditions. Such a development meets a demand, in particular for large structures at very low temperatures, where an alternative to the now available sensors is desirable.

1. Self-consistency requirements made a certain amount of redundancy between this document and the previous ones unavoidable.

Organization of the work

This work consists mainly in four chapters.

The chapter 2 is a review of solid-state physics literature about disordered systems in general and amorphous silica in particular.

The chapter 3 places Brillouin scattering into the more general context of light propagation in a medium; it then summarizes the theory of Brillouin scattering in general and discusses the specific case of the optical fibers.

In chapter 4, we extensively treat the dependence of Brillouin scattering on temperature.

The chapter 5 is devoted to the application of Brillouin scattering to distributed temperature sensing : experimental setups, performances and examples at usual and cryogenic temperatures.

Every chapter begins with its own introduction section, where more details about its contents are provided, as well as additional historical elements. Bibliographic references are given at the end of each chapter.

References

[1] *L. Brillouin*
Diffusion de la lumière et des rayons X par un corps transparent homogène : influence de l'agitation thermique
Annales de Physique, **17**, p. 88-122 (1922).

[2] *P. Debye, F.W. Sears*
On the scattering of light by supersonic waves
Proc. Nat. Acad. Sc., **18**, p. 409-414 (1932).

[3] *R.Y. Chiao, C.H. Townes, B.P. Stoicheff*
Stimulated Brillouin scattering and coherent generation of intense hypersonic waves
Phys. Rev. Lett., **12**(21), p. 592-595 (1964).

[4] *R.W. Boyd*
Nonlinear optics
Academic Press, San Diego (1992).

[5] *G.P. Agrawal*
Nonlinear fiber optics
2nd ed. Academic Press, San Diego (1995).

[6] *J.P. Dakin ed*
The distributed fibre optic sensing handbook
Springer, Berlin (1990).

[7] *J.P. Dakin, B. Culshaw ed*s
Optical fiber sensors. Vol. 4 : applications, analysis, and future trends
Artech House, Boston (1997).

[8] *M. Niklès*
La diffusion Brillouin dans les fibres optiques : étude et application aux capteurs distribués
Ph.D. Thesis EPFL, Lausanne (1997).

[9] *M. Facchini*
Distributed optical fiber sensors based on Brillouin scattering
Ph.D. Thesis EPFL, Lausanne (2001).

CHAPTER 2

Structure and vibrational properties of silica

2.1 Introduction

> To many persons a block of ice may seem of no more interest and beauty than a block of glass; but in reality it bears the same relationship to glass that orchestral harmony does to the cries of the marketplace. The ice is order, the glass is confusion. In the glass, molecular forces constitute an inextricably entangled skein; in ice they are woven to a symmetric texture...
>
> John Tyndall, 1863, quoted in [1].

Glass has accompanied mankind for millennia; the table 2.1 lists some of its most noticeable applications together with the date associated with their invention. But the above quotation gives testimony that these centuries of service did not suffice to be put on a equal footing as a mere block of ice in the eye of a typical Victorian scientist. This bias against amorphous materials lasted until well in the XX^{th} century. Now the situation has evolved : in the terms of Tyndall's comparisons, one could say that we can partly make sense of the cries of the marketplace[1], and take advantage of some of the favorable bargains. Most of the progress is however recent : the first Nobel prize to a searcher in this field was only awarded in 1977 to Nevill Mott [2].

This thesis is not a core contribution to the physics of amorphous solids. However, it deals abundantly with it, so that we feel it necessary to devote a rather

1. On the other hand, orchestral harmony is no longer what it used to be either, after Stockhausen and his likes... Interestingly, the musical metaphor of solid-state physics could be pursued further : dodecaphony for quasi-crystals, dissonances for impurities...

long initial chapter to a review of those aspects of it that are relevant to the understanding of our optics experiments.

Date	Event
~-3000	Invention (probably by accident) of the art of glassmaking in Egypt or Mesopotamia. Primary use of glass is jewelry.
~-100	Invention of the glass blower's pipe in the Roman empire. Glass vessels become commonplace, but the technology stagnates.
~1200	Great stained-glass windows of the gothic cathedrals
~1285	Some anonymous lens-maker puts them next to his eyes, and invents spectacles
1609	Galileo invents the telescope and aims it at the moon and the stars
1704	Newton publishes his *Opticks*
1865	Maxwell's laws link optics to electromagnetism
~1920	Quantum theory of light
1960	Demonstration of the first laser by Maiman
1970	First low-loss single-mode fiber developed at Corning by Maurer, Keck and Schultz

Table 2.1. Some outstanding dates in the history of optics and glasses.

We will begin with basic definitions centering on the nature of disorder in general and of the vitreous state in particular. Then we will address the question of the thermodynamic characteristics of glasses, with particular emphasis on the glass transition. The next section will be devoted specifically to the structure of vitreous silica, the archetypal glass former and, besides, the material optical fibers are made of. Finally, the vibrational properties of silica will be treated in some details, since they are very closely related to Brillouin scattering, and have thus a direct impact on our experimental measurements.

2.2 Disorder definition

By nature, disorder is versatile. It is thus not really surprising that people get somewhat confused when asked about the precise meaning of terms like random, amorphous, glassy or disordered, applied to physical systems. Even the distinction between solids and liquids becomes blurred for the class of materials we want to consider here. To clarify the ideas from the outset, here are some useful definitions, from the monograph of Elliott [3]. The easiest way to define disorder is to compare it to a standard of order, namely the crystalline state.

- *A perfect crystal is a solid in which the atoms are arranged in a pattern that repeats periodically in three dimensions to an infinite extent.*

Of course, with the drastic requirement of infinite periodicity, there is no perfect crystal in the real world. Real crystals end at surfaces and show other imperfections, like interstitial impurities or dislocation. But these perturbations are small enough not to hide the overall periodicity. That is no longer true in a number of situations, four of the most important being schematized in figure 2-1.

The case *a*, topological or geometrical disorder, encompasses glasses like silica and will be examined in details in the rest of this chapter. In *b*, the crystalline lattice is preserved but each atomic site possesses a randomly oriented magnetic moment or spin. The materials in this category, mostly magnetic alloys like Cu-Mn, are termed spin glasses, not to be confused with “true” glasses. Substitutional disorder (case *c*) arises when a second type of atoms randomly replaces the normal ones, creating an alloy without destroying the crystalline lattice. The last represented disorder is always present at finite temperature : even in a perfect crystal, the instantaneous positions of the atoms do not coincide with the lattice points; they rather oscillate around them as a result of the thermal agitation, although the time-averaged positions coincide with them.

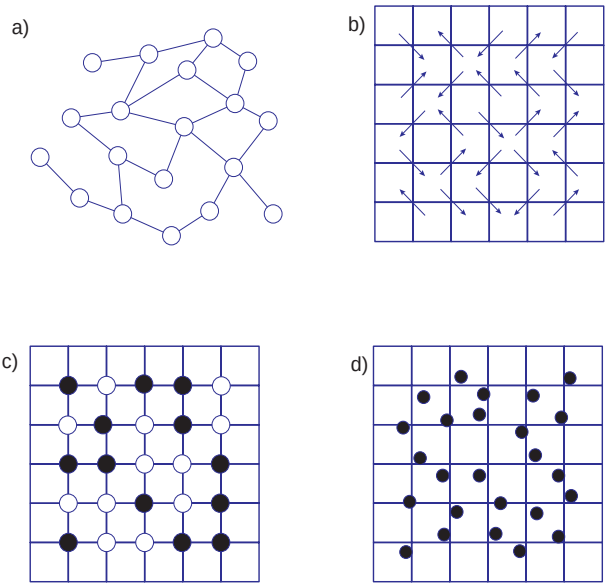

Figure 2-1. Types of disorder : a) topological, b) orientational, c) substitutional, d) vibrational

- *Amorphous materials do not possess the long-range order (periodicity) characteristic of a crystal.*

Under this definition, amorphous and non-crystalline are synonymous[1] and both adjectives describe a material with topological disorder (case *a* of figure 2-1). Nevertheless, to deserve the denomination “glass”, a solid needs other features. Many authors have proposed slightly different definitions, depending on the aspects they wanted to emphasize. The most general one, though disappointingly utilitarian and apparently close to tautology, seems to be :

- *A glassy (or synonymously vitreous) material is an amorphous solid that exhibits a glass transition.*

1. Note that “amorphous”, in this sense, has drifted away from its etymological meaning of “body without its own shape” that can not encompass solids.

Therefore all glasses are amorphous by definition, while all amorphous solids are not necessarily glassy. The glass transition is the subject of the next paragraph. In short, it is a phenomenon marked by a discontinuity in derivative thermodynamic properties (e. g. specific heat) as a function of temperature, while primary properties (e. g. volume) change continuously from solid to liquid state. The viscosity[1] varies continuously with temperature too, what raises an interesting question : where to set the boundary between a solid and a very viscous liquid ? The answer can only be arbitrary. According to Elliott [3],

a solid is a material whose shear viscosity exceeds $10^{14.6}$ poise (or $10^{13.6}$Pa s).

The numeric value has been chosen so that 1 cm^3 of material having this viscosity experiences a 0.02 mm deformation after application of a 100 N shear stress during 1 day. In other terms, a material is a solid if the application of a small force during one day produces no permanent deformation. Thus glasses below the glass transition temperature, specially silica at ambient temperature, are solids for all practical purposes, and not very slowly flowing liquids[2].

1. The viscosity is a measure of the internal friction, which results from the relative motion of different layers of a liquid. It appears as a factor of proportionality η in the relation $F = \eta A \frac{dv}{dx}$, where $\frac{dv}{dx}$ is a change of velocity of a layer, *A* the surface area of the layer and *F* the force acting between the layers.

   This equation proposed by Newton is only valid for so-called Newtonian liquids, but these are quite numerous, and include glass-forming melts.

   In the ISU, the viscosity is expressed in Pa s. The Poise is still widely used in the literature. 1 Poise = 0.1 Pa s.

2. The urban legend according to which the windowpanes of gothic cathedrals are thicker at the bottom because glass has flowed down in the course of centuries is simply unfounded.

2.3 Glass fabrication and thermodynamics

2.3.1 Thermodynamic phases and phase transformations

Thermodynamic phases are defined as different equilibrium forms of appearance of one substance. The notion is more restricted than that of states of aggregation : there are only three of the latter, namely gaseous, liquid and solid[1], while different phases of a substance can exist within the same state of aggregation (e. g. the polymorphs of water ice or of crystalline silica). Classical thermodynamics, which deals with such equilibrium states, is based on three famous postulates or laws :

1st law : energy conservation. The internal energy U of a closed system is changed only by a transfer of heat Q or of work A.

$$dU = dQ + dA \tag{2.1}$$

2nd law : entropy increase. In any transformation, the following inequality holds

$$dS \geq \frac{dQ}{T} \tag{2.2}$$

Introducing the pressure p and the volume V and taking (2.2) into account, (2.1) can be transformed into

$$dU \leq TdS - pdV \tag{2.3}$$

The equality sign in the last two equations is valid for so-called reversible or quasistatic processes, that follow a sequence of equilibrium states. Such states are distinguished by two properties :

1) for fixed external parameters, no macroscopic processes proceed in the system.
2) the macroscopic properties are determined only by the actual values of the external parameters and do not depend on the history of the system.

As will be seen later, glasses do not comply with the second part of this definition.

3rd law : approaching absolute zero temperature, the entropy of a system in internal thermodynamic equilibrium tends toward zero, for any pressure or state of aggregation.

1. Plasmas have some right to be seen as the fourth, ionized state of the matter; but the physics involved in their study is clearly out of the scope of this work.

$$\lim_{T \to 0} S = 0 \tag{2.4}$$

With Boltzmann's statistical interpretation of entropy as $S = k_B \ln \Omega$, where Ω is the number of microscopic realizations of one definite macroscopic state, the 3rd law can be reformulated as the statement that only one microstate corresponds to the macrostate $T \to 0$.

Two more thermodynamic functions, the enthalpy *H* and the Gibbs's free energy *G* are useful in practice when systems are investigated at constant external pressure. They are defined as $H = U + pV$ and $G = H - TS$. Like the internal energy *U*, both act as a thermodynamic potential steering the evolution of the considered system and the choice between them is a question of convenience depending on the experimental conditions. For instance, the experimentally easily measurable heat capacity at constant pressure C_p, defined by $C_p = \left(\frac{dQ}{dT}\right)_p$, is related to the enthalpy and to the entropy by

$$C_p = \left(\frac{dH}{dT}\right)_p = T\left(\frac{dS}{dT}\right)_p \tag{2.5}$$

for a closed system and isobaric conditions.

Transitions between states have been studied and classified by Ehrenfest. We limit ourselves to the so-called first and second order phase transitions, that include respectively crystallization and glass transition[1]. The left part of figure 2-2 shows schematically the variation of the thermodynamic potential *G* for two phases in a first order transition. At low temperatures, the phase 2 is energetically more favorable. At the critical temperature T_c, the curves cross and both phases coexist. With further increase of *T*, the phase 1 has the lower energy level and the system will eventually set to it. The actually followed path (i.e. branch 2 up to T_c and branch 1 afterwards) exhibits a discontinuity in the first order derivative of the temperature, hence the name of the transition.
In second order phase transitions (right part of the same figure) on the contrary, the tangents to the curves representing both possible phases coincide also at the critical temperature, but the second derivatives differ. Physically, this difference shows itself in the thermodynamic coefficients like the heat capacity and the ther-

1. To summarize explicitly all the restrictions we make : we consider isobaric transformations of closed, one-component systems.

mal expansion, while the discontinuity in the first derivative reflects qualitative changes of the structure itself.

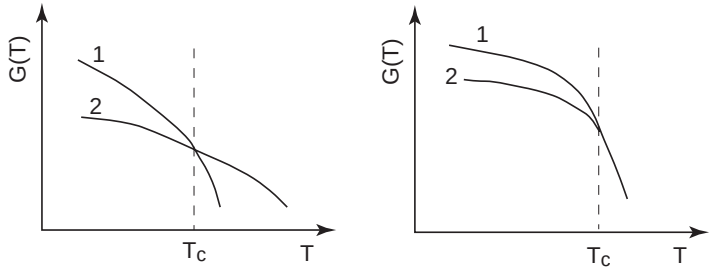

Figure 2-2. Schematic dependencies of thermodynamic potential on temperature in the case of first (left) and second (right) order transitions.

2.3.2 Crystallization vs. glass transition

After the generalities of the previous paragraph, we now consider more precisely what happens when a liquid is cooled down. The common experience tells us that it will end up a solid, sooner or later[1]. But solidification can take different paths. Let us assume that we have a crucible containing a pure melt at a temperature above the melting point T_m, and that we remove energy from it at a constant rate. The resulting decrease in temperature, as a function of time, will follow one of the three curves of figure 2-3. The melt may start to crystallize immediately at temperature T_m (case *a*). Then a time interval is found during which the temperature remains a constant, the external cooling being compensated by the release of the latent heat of fusion. At the end of this stage, the material is fully crystallized and continues its cooling down process as a solid. The case *b* exemplifies another often observed behavior[2]. This time, the initial cooling curve of the liquid is extended into a metastable, undercooled region. After a critical undercooling $\Delta T_{max} = T_m - T_{min}$ is reached, a spontaneous and sudden crystallization begins. The release of the latent heat is quick and causes an increase of temperature up to T_m again. From this point on, the cooling process replicates that of case *a*.

1. The exception of superfluid helium is - well, an exception.

2. An ubiquitous example is the water, where T_m=*273 K and* T_{min}=*233K*.

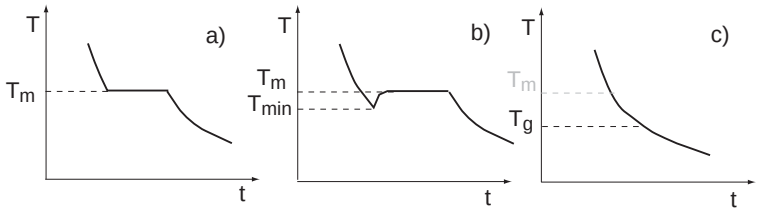

Figure 2-3. Temperature evolution of a melt at constant cooling rate for three situations : (a) immediate crystallization, (b) crystallization after undercooling, and (c) no crystallization.

The two previous *T(t)* curves show only slight transitory variations, since their end results are identical : crystal in both cases. The story in *c* is totally different. The melt becomes undercooled but the material, before reaching the critical temperature of spontaneous crystallization, is in a way trapped by its viscosity. The temperature T_g, below which the melt behaves like a solid (see section 2.2) is denoted as the glass transition temperature. There is no release of latent heat, and thus no discontinuous change of the structure of the system. By definition, the solid resulting from such a cooling curve is a glass.

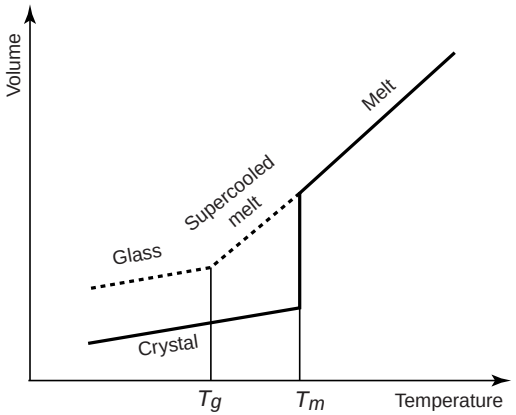

Figure 2-4. Schematical diagram of the temperature dependence of volume in different thermodynamic phases. After [4].

The absence of discontinuities in the glass transition, in sharp contrast with what occurs in crystallization, is most clearly highlighted in a volume vs. temperature plot like that of figure 2-4. Looking at the expansion coefficients of the different

phases, we notice that the curve describing the metastable supercooled melt prolongs of the thermodynamically stable liquid above T_m down to T_g, while the slopes of the crystalline phase and of the glassy part below this turning point are more or less equal. Such a plot could give the impression that T_g is a unique, well-defined temperature for any given material. Actually it is rather an arbitrarily chosen[1] value within an extended transition range between the two slopes. Moreover, the very position of this transition range depends on additional, external parameters, most noticeably on the cooling rate.

A very convenient way of taking this fact into account is to use the fictive temperature T_f, which is defined as the intersection of the extrapolated liquid and glass curves in figure 2-4. As can be seen in figure 2-5, it is found that a smaller rate of cooling results in a lower fictive temperature. The variation can easily reach as much as 10 or 20% for widely different cooling rates.

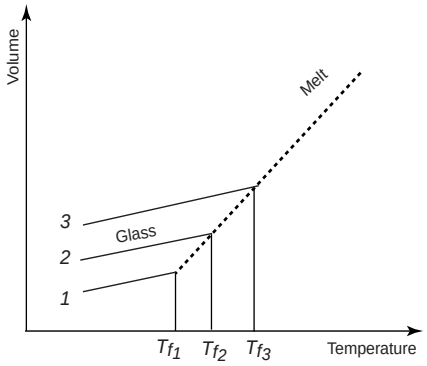

Figure 2-5. Dependence of the fictive temperature on the cooling rate. The slower the cooling, the lower the fictive temperature.

As was mentioned in section 2.3.1, glass transition can be considered as a second-order transformation in Ehrenfest's classification. As such, it should exhibit discontinuities in derivative thermodynamic variables like coefficient of thermal expansion and heat capacity. Figure 2-6 shows that it is indeed the case : the value of the heat capacity for the glass is comparable to that of the crystal, but much smaller than that of the liquid. Incidentally, such a curve makes it possible to determine the glass transition temperature with considerably better accuracy than a volumetric measurement like that of figure 2-4. Note also that the heat

1. Usually by imposing the condition that it corresponds to the minimal viscosity of a solid.

capacity along the crystallization path presents a singularity, not represented here, at T_m, where it tends to infinity.

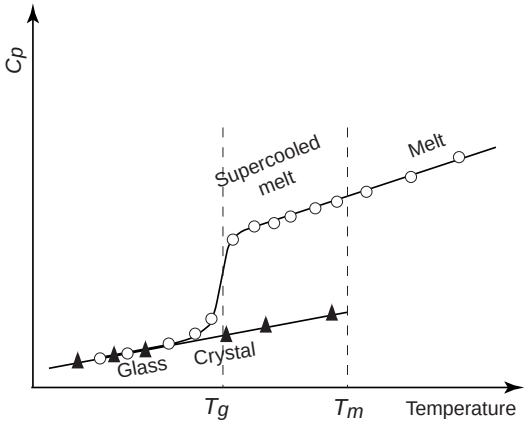

Figure 2-6. Typical heat capacity curves for the liquid, crystalline and vitreous states of a substance. The values of C_p for the crystalline state are symbolized by black triangles, while white circles specify values for the liquid and the glass. After [5].

The mechanical analogy proposed by Gutzow and Schmelzer [5] and sketched in figure 2-7 seems a suitable conclusion to this section on the thermodynamic nature of glasses, because it provides a visual and intuitive support to quite abstract statements. The thermodynamic states are represented as balls in a potential well. Three states are represented here :

a) At $T<T_m$, the crystalline state is an absolute minimum of the potential well, hence a stable state.

b) The undercooled melt in the temperature range $T_g<T<T_m$ corresponds to a local minimum of the potential, that is to a metastable state. It can not be transferred to the energetically more favorable crystalline state unless some energy is injected into the system to overcome the barrier ΔG.

c) The glass is not even in a local minimum. Below T_g, its viscosity, here pictured by the glue covering the walls of the well, prevents it from reaching any stable or metastable state.

This leads us to a definition of the vitreous state that is more precise than that of section 2.2 :

- *Glasses are frozen-in non-equilibrium systems.*

This definition is also more general than the other one since it does not mention the glass transition and therefore can be applied to system obtained by vapor deposition or other methods. As non-equilibrium systems, glasses do not follow the third law of thermodynamics, and they have a non-null residual entropy even for $T \to 0$ K.

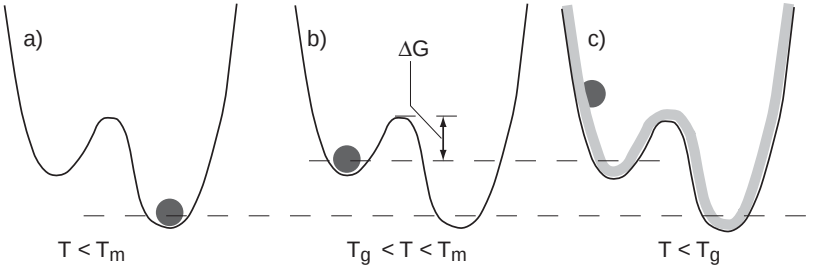

Figure 2-7. Mechanical analogy for an interpretation of the differences between the stable crystalline state (a), the metastable melt (b) and the glass (c). After [5].

2.3.3 Techniques of glass production

Melt quenching

As evidenced by the developments of the previous section, the secret of glass making is to avoid crystallization. The oldest, and for long centuries only established method of doing so is to cool down the molten form of the material quickly enough. "Quickly enough" means here that the span of time used to cross the critical temperature zone is too short to allow the structural reorganization of the atoms that creates the crystalline phase. Of course, the viscosity of the melt at the crystallization temperature is an essential parameter. Depending on it, crystallization occurrence can be anything between unlikely (for highly viscous melts) and unavoidable; accordingly, a vitreous phase forms easily in some materials such as the archetypal silicates while technological feats are required to obtain it in other cases, e.g. the metallic glasses. table 2.2 lists some typical cooling rates together with the quenching techniques that allow them. They range from 10^{-5} K/s for the annealing of large astronomical mirrors[1] to 10^{8} K/s for highly efficient heat extraction methods like chill-blocks applied to thin films. The still higher cooling rate obtained by using evaporation methods is shown here for compari-

son, but it relies on a radically different principle of glass fabrication, which is the subject of the next subsection.

Technique	Cooling rate [K/s]
Annealing	
large telescope mirror	10^{-5}
optical glass	$3x10^{-4}$
ordinary glass	10^{-3} to 10^{-2}
Air quenching	1 to 10
Liquid quenching	10^{2} to 10^{3}
Chill-block	10^{5} to 10^{8}
Evaporation	$\sim 10^{9}$

Table 2.2. A few quenching techniques and their characteristic cooling rates

Deposition methods

Technological advances in the last decades have made it possible to obtain novel glassy phases of materials that were previously always crystalline. Part of these advances consist simply in methods of increasing the cooling rate of a melt[1]. The other ones are conceptually new; in essence, they come down to directly building the solid glass, atom by atom, without the intermediate liquid stage. Generally, they involve deposition of gaseous forms of the glass-forming ions onto a substrate. There are many methods to get the desired gases, and each one presents its own intricate technical details for the control of the composition or for getting rid of impurities; one can cite thermal evaporation, glow-discharge decomposition, sputtering, chemical vapor deposition. The usual result is a thin film of amorphous material.

Of particular relevance for fiber optics is the so-called modified chemical vapor deposition (MCVD) technique depicted in figure 2-8, after [6]. To produce high purity amorphous silica, the reaction $SiCl_4 + O_2 \rightarrow SiO_2 + 2Cl_2$ is carried out

1. As long as crystal growth is avoided, the slower the cooling, the better the end product. For the stringent requirements of large telescopes, the duration of the cooling process reaches many months.

1. For example, the first amorphous metal, an alloy of gold and silicon, was produced in 1960 by “spat cooling”, that is by projecting small droplets of liquid on a cold surface.

in an oxhydrogen flame, and the resulting SiO_2 is deposited layer by layer in the inside of a fused silica tube. In order to get the desired refractive index profile, vapors of $GeCl_4$ or $POCl_3$ are added as required to the gaseous mix. When all layers have been deposited, the temperature of the whole tube is raised so as to collapse it into a solid rod of preform, subsequently drawn into a fiber.

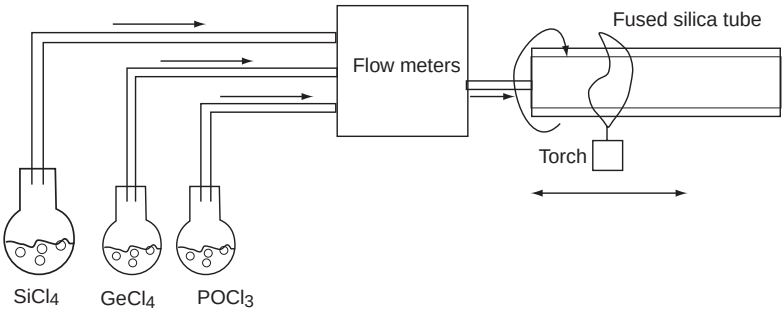

Figure 2-8. Schematic diagram of the MCVD process for fiber preform fabrication

Irradiation

The bombardment of a crystal by high-energy ionizing particles (ions, neutrons or electrons) results in an amorphization of the solid [7]. As an example, quartz is transformed into amorphous silica by irradiation of ~10^{20} neutrons/cm^2. Interestingly enough, the density of this form is 2.26 g/cm^3, to compare with 2.205 g/cm^3, density of the usual glass resulting from melt quenching. Moreover, usual silica glass submitted to the same amount of radiation also undergoes a transformation into this new phase. This could lead to problems for the applications of optical fibers in harsh radiative environments, like space or particle accelerators, since they lose their favorable properties in the process.

At first sight, this mechanism of glass production could seem different from those mentioned in the previous sections; in analyzing the process though, it must be taken into account that temperature changes of up to 10000 K are to be expected along neutron tracks in crystal[5]. In this sense, the transformation crystal → glass should be described as a sequence crystal → super-heated melt → glass.

2.4 Structure of amorphous silica

Silicon dioxide SiO_2 has been the main ingredient of glasses since the origin : the oldest known man-made glasses contain approximately 70% wt SiO_2, 20% wt Na_2O and 10% wt CaO. The presence of a relatively large amount of minority minerals has nothing to do with chance, but is related to the high fusion temperature (about 1800°C) of pure silica (See table 2.3 for a list of some physical properties of fused silica). The fusion point was markedly lowered by including sodium in the crucible, making it possible to shape the glass into vessels or jewels with the available heat sources of the time. Technological limitations proved indeed hard to overcome and they effectively prevented real single-component silica glass to be routinely produced before the XX^{th} century.

Density	2.2×10^3 kg/m^3
Bulk modulus	3.7×10^{10} N/m^2
Young's modulus	7.17×10^{10} N/m^2
Poisson's ratio	0.16
Elasto-optic coefficients	$p_{11} = 0.113$; $p_{12} = 0.252$
Fusion temperature	1800 °C
Glass transition temperature	~1450 °C
Refractive index	1.4585
Longitudinal sound velocity	5.9×10^3 m/s
Transverse sound velocity	3.75×10^3 m/s

Table 2.3. Some physical properties of fused silica in normal conditions

Due to the huge number of its applications, silica has been intensively studied and its properties thoroughly examined. Its structure is now satisfactorily understood, and this section will be devoted to the presentation of the way atoms are disposed in it. As will be shown, the length scale is the essential parameter that must be stipulated when looking at an amorphous material; depending on the zoom level, entirely different features are visible. Consequently, we will deal successively with short-range order (SRO) at the nm scale, medium-range order

(MRO)[1] up to 10 nm, and macroscopic properties. Incidentally, relevant experimental techniques will be mentioned.

2.4.1 Short-range order : SiO_4 tetrahedron

Silica minerals are far from rare, since they make up approximately for 12% of the Earth's crust, yet the overwhelmingly larger part of them are crystalline. Quartz, also known as rock crystal, is the most commonly occurring form, but there are several polymorphs under different conditions of pressure and temperature, indicated in figure 2-9. Natural amorphous silica can only be found in opals or as the result of quartz fusion by lightning strikes or meteorites impacts.

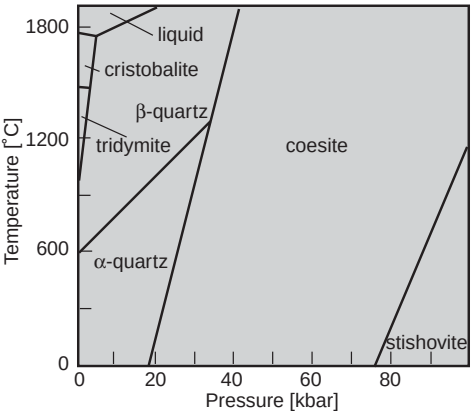

Figure 2-9. Temperature and pressure diagram of the stability zones of the silica crysalline polymorphs. After [8].

The common feature of all[2] the crystalline phases of silica is the fundamental tetrahedron made of four O atoms around one central Si. Two types of arguments can explain this shape :

- In terms of electronic orbitals of atoms, we know that silicon forms a sp^3 hybrid, in which four directed bonds span a tetrahedron.
- The larger O anions determine a dense packing (i. e. they are touching). The cations Si have to find their places in the remaining gaps. The structural arrangement of the atoms depends only on the ion radius ratio. Here $r_{Si}/r_O = 0.3$, result-

1. As will become apparent later, the amorphous nature of the solid shows itself here, and one should maybe speak of "ordered disorder" rather than of "order".
2. The very high pressure form stishovite is the only exception with its octahedral geometry.

ing in tetrahedral geometry; a ratio smaller than 0.225 would have led to a plane triangle, while 0.414 is the lower limit for octahedral geometry.
The angle O-Si-O for a perfect tetrahedron is 109°, and the distance Si-O is 0.161 nm. The figure 2-10 shows how the SiO_4 tetrahedra are disposed to build a sheet of ideal tridymite.

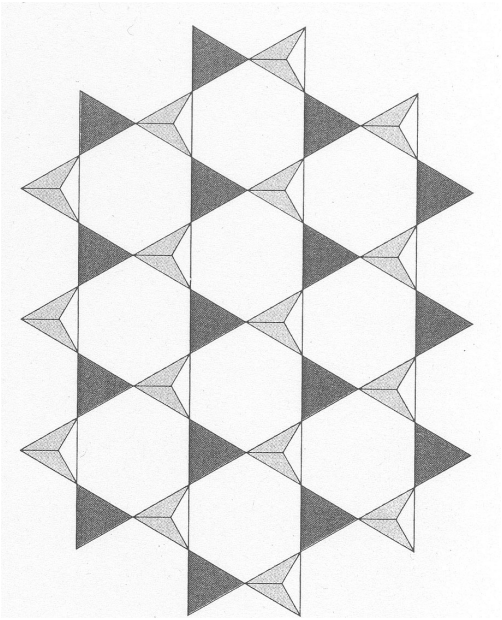

Figure 2-10. Portion of an idealized sheet of SiO_4 tetrahedra similar to that found in tridymite and cristobalite. The tetrahedra point alternatively in opposite directions. The relative disposition of adjacent planes depends on the crystalline phase.

The experimental techniques that allow the determination of the structure of crystalline solids make up an important topic in any solid-state physics textbook (see for example [9]). They include magnetic resonance [10] and vibrational spectroscopy, but the most versatile ones are based on the scattering of neutrons, electrons or X-ray. The interpretation of diffraction patterns relies on Bragg's law and is the primary task of crystallography. When the same experimental techniques are applied to the study of amorphous materials, their raw results differ strongly from the ordered case : instead of regularly disposed points[1], the diffraction produces diffuse haloes. The extraction of significant structural bits of information from such a blurred picture is still possible [3], though, and these are often

1. Or sharp concentric circles characteristic of randomly oriented crystals in a polycrystalline sample.

expressed in terms of density function $\rho(r)$ or of radial distribution functions (RDFs). The RDF $J(r) = 4\pi r^2 \rho(r)$ is defined such that the average number of atoms centers lying between r and $r+dr$ from an arbitrary origin atom is $J(r)dr$. The figure 2-11 illustrates schematically the appearance of the density function for a 2D amorphous structure. It can be seen that the first peak in $\rho(r)$ corresponds to the first shell of atoms (nearest neighbors), the second peak to the second shell, and so on. Beyond the first few peaks however, the atomic shells lose their meaning and the curve tends toward the average density of the solid. It must be kept in mind as well that the RDF is a 1D representation of a 3D structure, and as such is strictly valid for isotropic materials only.

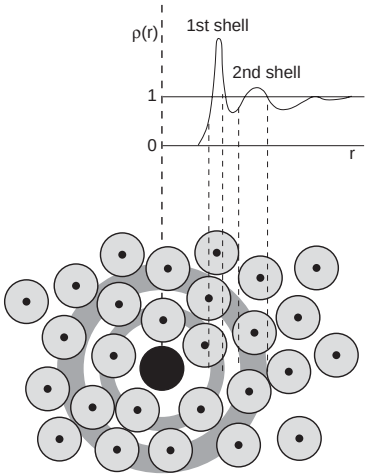

Figure 2-11. Schematic illustration of the physical meaning of the density function $\rho(r)$ for an amorphous solid.

It is now time to go back to the specific topic of amorphous silica (a-SiO_2) with the figure 2-12. It represents the experimental RDF of a sample of a-SiO_2, together with the calculated RDF for some specific numerical model. From the positions of the first two peaks, it can be inferred that vitreous silica is composed of the same SiO_4 tetrahedra as quartz or tridymite. For example, the angle θ between two Si-O links on an oxygen atom is given by

$$\sin\frac{\theta}{2} = \frac{d(O-O)/2}{d(Si-O)}. \qquad (2.6)$$

Introducing the measured distances of the first two peaks in (2.6), the tetrahedral angle of 109° is retrieved.

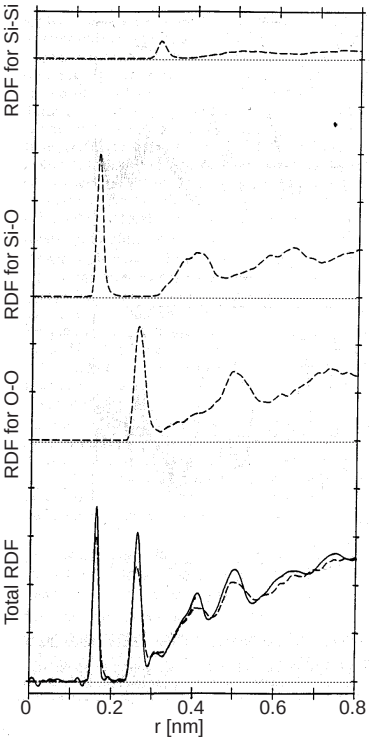

Figure 2-12. Radial distribution functions for vitreous silica. Full line indicates experimental data; dashed lines refer to molecular dynamics simulations. The three upper curves are partial RDFs for Si...Si (top), Si...O (2^{nd}) and O...O (3^{rd}). From [11].

2.4.2 Medium-range order : continuous random network

Since the difference between crystalline and amorphous silica does not show up at the nearest-neighbor scale, let us broaden our field of vision. A hint is given by the RDF of figure 2-12 : the peaks become wider as the distance grows. So the atoms should slowly depart from the ideal, crystalline positions : some kind of

residual order is still visible at short distances, but it is then blurred away. To account for this behavior, the most successful model dates back to 1932. When he published his famous article [12][1] in that year, W. H. Zachariasen began by the frank admission that "we know practically nothing about the atomic arrangement in glasses". He proceeded then by stating that :

- Mechanical properties of glasses are directly comparable with those of crystals. In both cases, the atoms must thus be linked by essentially the same forces and form extended 3D networks.
- X-ray diffraction experiments imply that this network is not periodic and symmetrical. Yet it can not be purely random, since all interatomic distances are not equally probable.

Zachariasen's suggestion to account for these facts in the case of a-SiO_2 was to keep the SiO_4 tetrahedra of the crystalline forms, but to bring in some liberty in the way they are linked together. Specifically, the angle Si-O-Si is allowed to vary within rather wide limits. The two pictures illustrating this seminal paper are probably the most reproduced in the history of amorphous solids science. To comply with the tradition, they are also presented here as figure 2-13.

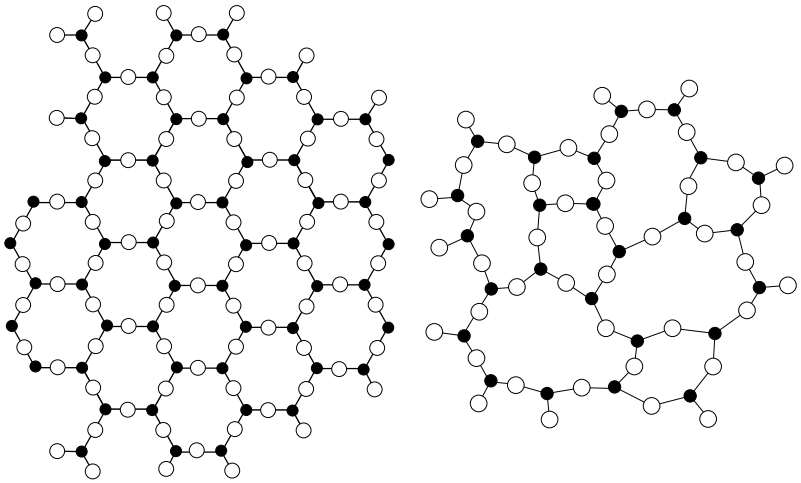

Figure 2-13. 2D analogy of the difference between a regular network (left) and a continuous random network (right) with the same chemical composition. After [12]

1. Incidentally, the posterity of this paper is fairly impressive : it seems that all publications in the domain make reference to it.

Models of this kind became known as continuous random networks (CRN). Seventy years after their introduction, after some refinements but no fundamental change, they remain the favorite frameworks used to describe glasses in general and a-SiO_2 in particular.

In a recent formulation [13], a CRN model of silica is made up by a remarkably limited number of statements (see figure 2-14) :

- a very narrow distribution of bond lengths *r* peaked at *r* = 0.161 nm
- a narrow distribution of O-Si-O angles ψ peaked at ψ = 109.5° [1]
- a broad distribution of Si-O-Si angles θ peaked at θ =144°
- a flat distribution of dihedral angles δ.

In addition, all parameters are uncorrelated and no structures appear at a larger scale.

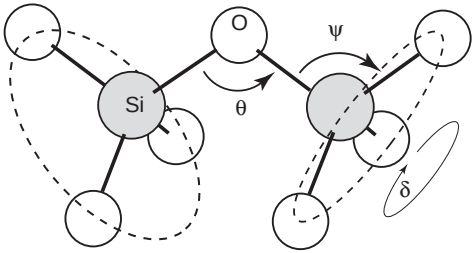

Figure 2-14. Two SiO_4 molecular units joined by a bridging oxygen atom. The Si-O-Si angle θ varies from bond to bond and may lie anywhere within a range of about 120° to 180°, with a maximum probability of 144°. Each molecular unit can lie in any of the positions obtained by rotating it around δ, so that the oxygens may assume many different sets of position on the dotted circles.

CRN models have been validated by numerous calculations, whose results agree well with the experimental ones. An example for the radial distribution function has been already presented (figure 2-12) here. In this case, the atoms are purely numeric, but the first calculations realized in the 1960's were based on real models [14, 15], that is on a few hundreds plastic balls and sticks patiently assembled by hand. It is no surprise that computers have taken over these initial attempts, in spite of their honorable successes. Depending on the exact properties that have to be calculated, many numerical methods are now available [3] : Monte Carlo or molecular dynamic simulations for RDFs, Bethe lattice or equation-of-motion methods for vibrational properties...[16, 17]

1. This requirement imposes the tetrahedral geometry.

2.4.3 Long-range order

Zachariasen's CRN model is widely accepted, its simplicity being perhaps as instrumental in its success as its explanatory capacities. Despite this success, some authors [18-22] argue that it is not fully satisfying and that its weakness lies in the total absence of specifications beyond the second-nearest neighbor distance. According to these authors, some kind of order at a larger scale should be included in the picture. By putting forth this requirement, they somewhat recall to life a long discarded description of glasses, namely the microcrystallite model. Under its original form by Lebedev in the 1920's [23], this model assumes that a glass consists of 'islands' of crystal-like disposed atoms separated by disordered zones. The size of the islands varies between 3-5 and 15 nm. These assumptions were early recognized as incompatible with X-ray diffraction patterns. But new, more subtle versions are now discussed, involving atomic clusters of ~10 nm, so-called microparacrystals or closed rings of 5 or 7 tetrahedra.

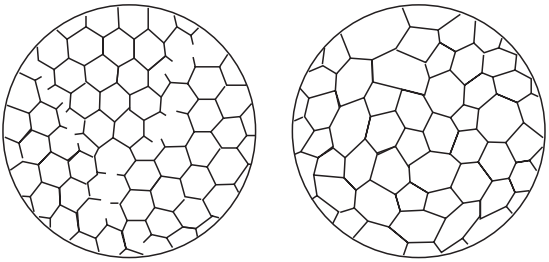

Figure 2-15. Microcrystalline (left) vs continous random network. After [4, 24]

Finally, there are necessarily macroscopic inhomogeneities in amorphous silica due to the method of fabrication of glass. As a frozen-in melt, the glass keeps the density fluctuations typical of a liquid. Rayleigh scattering (see next chapter) of light is precisely due to these fluctuations.

2.5 Vibrational properties

So far, we have discussed at length the static arrangement of atoms in an amorphous solid, with particular emphasis on a-SiO_2. Now we turn our attention to their dynamic behavior and try to determine the nature of their vibrational excitations. These excitations are involved in many phenomena : firstly sound and heat propagation, but electromagnetic waves can also interact with them under certain circumstances and the bulk of this thesis is devoted to some aspects of these interactions.

2.5.1 Density of states

In crystals, vibrational excitations are described in the 'language' of phonons. The decomposition of any vibration onto a basis of harmonic modes is a very powerful tool, even if the understanding of some properties requires extensions of the theory beyond the harmonic approximation. The annex 2 gives a brief derivation of the construction of phonons after standard textbooks. The one point we want to highlight here is the use of the crystalline structure of the solid in the course of the development. This leads us to the question whether phonons exist at all when the periodicity assumption is not fulfilled. Evidently, modes of vibration do still exist, since it is common experience that glass transmits sound and heat. Nevertheless, the absence of periodicity imposes some changes in the mathematics and, perhaps more important, a cautious use of the term 'phonons'.

In amorphous solids, the concept of Brillouin zones, central in the formalism sketched in the annex 2, loses its meaning. This can be simply seen : in a crystal, the size of the first Brillouin zone is given by $2\pi/a$, where a is the size of the unit cell. An amorphous solid, deprived of periodicity, has a structure equivalent to a unit cell of infinite size; hence the Brillouin zone reduces to the point $\boldsymbol{q} = 0$. It is still possible to experimentally ascertain the dependence of vibrational frequencies on scattering vectors, but the dispersion does not follow clean, singled-out curves like those in figure B.5 for example. The dispersion relation looks rather like that in figure 2-16 : for very low values of q, the locus of points may fall close to a single curve (here corresponding to an acoustic mode), while the curve becomes badly smeared out elsewhere.

Figure 2-16. Schematic representation of a dispersion relation $\omega(\boldsymbol{q})$ in a glass.

The shape of this dispersion 'curve' does not prevent the density of states (DOS) from being well defined for amorphous solids also. Indeed it can be seen in figure 2-17 that it bears a family likeness toward the density of states of the corresponding crystal. The general forms are strikingly alike, which is a new argument supporting the similarity of the short-range orders in both the amorphous and crystalline polymorphs. The difference is that the sharp Van Hove singularities, signatures of the periodicity, are now smoothed out.

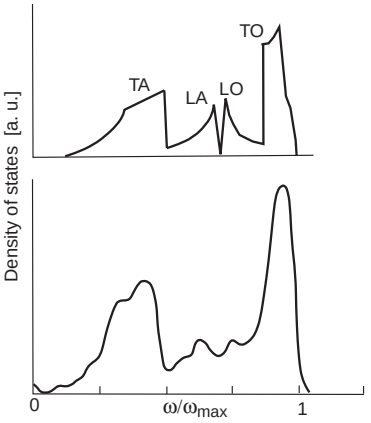

Figure 2-17. Comparison of the density of states calculated for diamond cubic Si (*up*) and a continuous random network model of amorphous Si (*down*) [3].

So some of the features found in periodic solids remain. In the low-frequency region of figure 2-17, glasses can be approximated by a continuum, exactly like the corresponding crystals. One can here speak of plane-wave (or quasi-plane-wave) acoustic phonons. A central question is up to which wavevector value *q*

such a description keeps its validity; in any case, the wavevectors involved in Brillouin scattering of infrared light fall within this range, vindicating the use of the term ‘phonon’ in this context. On the other hand, the structural units (i. e. the tetrahedra or some other small groups of atoms) can collectively execute their own vibrations in parallel; some kind of optical modes near $q = 0$ are therefore to be expected.

In itself, the density of states is a rather abstract concept, albeit susceptible of direct measurement. Its practical importance lies in the simplification it brings to the calculation of more applied lattice properties. The example of the specific heat[1] will illustrate that [9].
The lattice specific heat c_V is the derivative with respect to the temperature of the internal energy. For a crystal[2], it is given by

$$c_V = \frac{\partial}{\partial T}\sum_s \int \frac{d\boldsymbol{q}}{(2\pi)^3} \frac{\hbar\omega(\boldsymbol{q})}{\exp(\hbar\omega/k_B T) - 1}, \tag{2.7}$$

where the summation has to be carried out on all branches of the dispersion curves and the integration is over all vectors in the first Brillouin zone. By using the DOS $G(\omega)$, (2.7) is replaced by a much simpler integration over the frequency ω :

$$c_V = \frac{\partial}{\partial T}\int d\omega G(\omega) \frac{\hbar\omega}{\exp(\hbar\omega/k_B T) - 1}. \tag{2.8}$$

The well-known Debye approximation, that amounts to replacing the intricate dispersion relations $\omega(\mathbf{q})$ by a linear dependence $\omega = vq$, v being the sound velocity in the crystal, gives for example

$$G_D(\omega) = \frac{3\omega^2}{2\pi^2 c^3}. \tag{2.9}$$

The integral in (2.8) can then be evaluated for very low temperatures, yielding

1. We speak here of *lattice* specific heat, since the only solids considered are insulators. The electronic specific heat (in metallic glasses for example) is beyond the scope of this work.
2. But this definition can be readily extended to amorphous solids.

$$c_V \approx \frac{2\pi^2}{5} k_B \left(\frac{k_B T}{\hbar \rho v_D} \right)^3 , \qquad (2.10)$$

where v_D is given by a weighted average of longitudinal and transverse sound velocities[1] $\frac{3}{v_D^3} = \frac{1}{v_L^3} + \frac{2}{v_T^3}$, and

$$c_V = 3Nk_B \qquad (2.11)$$

in the limit of high temperatures (law of Dulong and Petit), with N the total number of atoms.

These relations have been cited here because the first experimental indication of the peculiar behavior of glasses was precisely a large deviation from the expected T^3 variation of the specific heat of silica in the temperature range $T \sim 1 - 10$ K (see section 2.5.3).

ν	λ	**W**	**E**	**T**
1 GHz	0.3 m	0.033 cm^{-1}	4.10^{-6} eV	0.05 K
10 GHz	30 mm	0.33 cm^{-1}	4.10^{-5} eV	0.5 K
100 GHz	3 mm	3.3 cm^{-1}	4.10^{-4} eV	5 K
1 THz	300 µm	33 cm^{-1}	4.10^{-3} eV	50 K
3 THz	100 µm	100 cm^{-1}	1.2 10^{-2} eV	150 K
10 THz	30 µm	330 cm^{-1}	0.04 eV	500 K
100 THz	3 µm	3300 cm^{-1}	0.4 eV	5000 K
200 THz	**1.5 µm**	6600 cm^{-1}	0.8 eV	10000 K
250 THz	1.2 µm	8250 cm^{-1}	**1 eV**	12000 K
1000 THz	300 nm	33000 cm^{-1}	4 eV	50000 K

Table 2.4. Vibrational energies in different units. Transformation relations :

$$E = h\nu = h\frac{c}{\lambda} = hcW = k_B T$$

1. Note that v_D can be viewed as the effective averaged group velocity of vibrations in the continuum limit. Is is also given by the ratio K/ρ of the bulk modulus and the density. In silica, $v_D \sim 4100$ m/s.

2.5.2 Techniques of investigation

Many different phenomena can be classified under the general heading 'vibrational properties'. Actually, it would be hardly exaggerated to say that the whole physics of amorphous insulators, apart from the static structure that was treated in section 2.4, is related to displacements of atoms, and thus to vibrations : heat transport, thermal expansion, macroscopic mechanical vibrations, sound and hypersound propagation, high and very high-frequency states,... all involve somehow the density of states. Yet with typical frequency scales ranging from quasi-DC to hundreds of THz, it comes as no surprise that the experimental techniques used to measure these properties are various.

High-frequency measurements

In view of the importance of the DOS, a logical way of tackling the description of the vibrational properties is to directly measure it. Three probing tools exist : infrared spectroscopy (IRS), Raman scattering and inelastic neutron scattering (INS) [3, 25]. They yield meaningful results for frequencies higher than ~1 THz[1], due to the small number of states at low frequencies. At the other extremity, the upper limit of vibrational spectra like figure 2-17 is about 1500 cm^{-1}, i.e. ~30 THz.

Infrared absorption by a vibrational mode takes place when the energy of the light photons corresponds to that of the latter. The explorable frequency range with IR spectroscopy lies between 3 and 300 THz, depending on the available sources. The interpretation of the resulting spectra is unfortunately not straightforward, because the IR absorption coefficient depends also on the dipole moment associated with the vibrational mode [26]:

$$\alpha_{IR}(\omega) \sim |M(\omega)|^2 G(\omega),$$

where $M(\omega)$ is the dipole moment matrix element, whose frequency dependency is usually not trivial.

Raman scattering (see section 3.2.2 for a few words about the physical process) has about the same domain of efficiency as IRS in terms of frequency. Here again, the raw spectra need heavy data reduction [25] in order to remove spurious

1. To facilitate the comparisons between figures of different origins, a few values of vibrational energies have been compiled in the various units frequently encountered in table 2.4.

effects that partly screen the intrinsic vibrational spectrum of the solid. A detailed discussion of the process, where the polarizability tensor of the vibration modes plays a key role, can be found in [26, 27], and the references therein.

On the contrary, one obtains clean spectra by inelastic neutron scattering. The drawback of the method is the scarce availability (and the price) of neutrons sources. Thermal neutrons have typically energies of the order of 25 meV, making them suitable for probing vibrations between 1 THz and 30 THz. Some examples of DOS obtained with the aforementioned methods will be given in the next section.

Low-frequency measurements

At frequencies below about 1 THz, the techniques described above become more or less useless and are supplemented by several additional ones [24]. Generally, the limited frequency ranges of these other methods do not allow the determination of any significant part of the DOS. Nevertheless, they complement ideally the information about the glasses by giving the values of the sound velocity, the heat capacity, etc. These results are interesting in themselves, often technologically significant, but they can also serve to test the validity of the structural and vibrational models. The methods include Brillouin scattering of visible or infrared light, with typical frequencies in the 10 to 100 GHz, which will be treated at great length in the next chapters.

At still lower frequencies, ultrasonic techniques take over : an ultrasonic pulse is applied to the sample through an appropriate transducer and the sound propagation is measured. In an early example [28], frequencies of 15 to 75 MHz were used. Plain mechanical measurements are also possible : in the vibrating reed technique for instance, the basic idea is to determine the resonance frequency and the amplitude of a small rectangular sample plate which is clamped on one end and driven electrically into forced vibrations on its free end [29]. Here the applied frequencies lie about 1-10 kHz.

Finally, there are the specialized techniques for the specific heat or the thermal conductivity, based on precisely calibrated cryostats, heating sources and thermometers [30].

The frequency domain that these various techniques encompass is huge, but it should be added that the temperature must also be varied over a very wide range.

To study the glass from essentially 0 K to the fusion temperature of a-SiO_2 (1800°C) or even further, quite heavy technical installations are necessary. And we do not even speak of the diamond anvils for hyper-high pressure experiments, or the whole chemistry laboratory that is necessary if the composition of the glass has to be considered on top of the physical parameters.

Numerical simulations

The physics of amorphous solids has long been a favorite playground for scientific programmers and it has enormously benefited from their work. We have already mentioned (section 2.4.2) the computer-built models of the static structure of glass; actually these are often merely a starting point for the simulation of dynamic properties [3]. The compatibility of calculated and measured spectra then strengthens the underlying assumptions of a model, while a clear discrepancy allows one to discard them. Moreover, the much more detailed knowledge gained by the simulations can shed a new light on the physical processes : since the movements of every atom are recorded, one can actually 'see' each mode of vibration, discriminate between rotation or twists, count the number of atoms involved...[17, 31, 32]. In this sense, numerical simulation deserves rightfully to be considered as a technique of investigation in the same way as neutron scattering.

2.5.3 Experimental results

An important turning point in the history of glass science is 1971. Before that date, people more or less consciously considered amorphous solids as 'over-defective' crystals. This was quite natural, since the theory of crystals was both elegant and successful and the effect of defects was well understood. Glasses were expected to be merely a quantitative extension, without new physics. Then a puzzling paper by Zeller and Pohl [30] came out, including the first detailed measurements of specific heat and thermal conductivity of silica below 5 K (see figures 2-18 and 2-19) and thus showing that there was definitely something new and interesting hidden in the box. Many research groups turned then to the subject, either to provide experimental results or to develop the theoretical models able to explain them.

From the outset, an attractive feature of the results was the universality of behavior : not only oxide glasses, but also inorganic and organic polymers

showed similar properties. Vitreous silica, though, kept a special position among the glasses. Its availability and its easy handling made it by far the most studied amorphous solid. Besides, its chemical simplicity opened widely the door to numerical simulations, although the progress was initially quite slow in this direction.

Three decades of intensive research have produced a great amount of data. A thorough review of the early works was published in 1981 [33]; at about the same time, Elliott did also a good job in putting knowledge of disparate sources into the unified framework of his already cited monograph [3]. An updated equivalent of these books, including the results of the more recent experimental and theoretical works, is unfortunately still to write, although one can find good reviews of specialized sub-areas of the domain [34, 35] or conference proceedings [11, 36-38].

Here we will restrict ourselves to a tiny sample of the experimental results concerning SiO_2. The properties we are interested in are either those we were directly able to measure with our Brillouin scattering experiments in optical fibers or those necessary to understand them. Inevitably, the presentation of these data will often take the form of a comparison between the crystalline and the vitreous states. For the interpretative models, please refer to the next section.

Heat capacity

The heat capacity of a-SiO_2 does not differ notably from that of c-SiO_2 at high temperatures, both tending toward the same constant value predicted by the law of Dulong and Petit. But it presents peculiarities in the low-temperature range (figure 2-18) :

- below 1K (not visible here), c_V varies nearly linearly as a function of T in the amorphous state, while it follows the expected T^3 curve in the crystalline one. Actually, the cubic term does exist in glass too, and the variation has to be expressed in the form

$$c_V = aT + bT^3. \qquad (2.12)$$

- the hump of the crystalline c_V above the value predicted by the Debye approximation can be readily explained by the higher density of states of the lowest TA phonon branch near the edge of the Brillouin zone (see annex 2). This excess heat

capacity is much more important in the amorphous state, and is besides slightly shifted to lower temperatures.

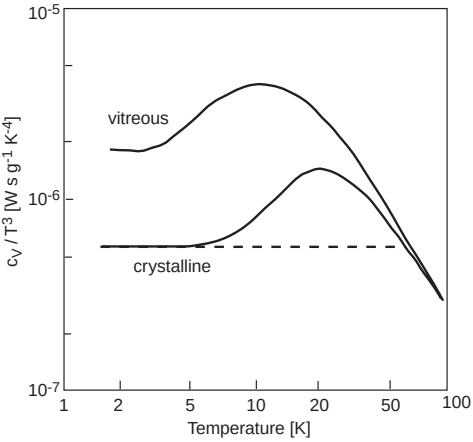

Figure 2-18. Specific heat of vitreous SiO_2 and crystal quartz plotted as c_V/T^3 vs *T*. The dashed horizontal line shows c_V/T^3 for quartz in the Debye approximation [30]

Thermal conductivity

In non-metallic crystals, the thermal transport is due to propagating phonons; the thermal conductivity κ may be written as

$$\kappa = \frac{1}{3}\sum_i \int d\omega G_i(\omega) v_i(\omega) l_i(\omega), \qquad (2.13)$$

where the sum is over all the phonon modes, *G* is the density of states, *v* the phonon velocity and *l* the mean free path. Typically, the temperature dependence of κ is peaked. To the right of the maximum, the increase in the rate of intrinsic phonon-phonon scattering results in a decrease of the mean free path; to its left, the DOS dominates the aspect of the curve, giving the famous T^3 behavior. In the figure 2-19, the differences in thermal conductivity κ between amorphous and crystalline solids are quite obvious :

- a-solids do not exhibit a peak in the curve κ*(T)*, but a monotonous increase.
- around 10 K, a near-zero slope zone or plateau is observed.
- the temperature dependence below 1 K is close to T^2.

Notice also the wide gap in the order of magnitude of κ in this region.

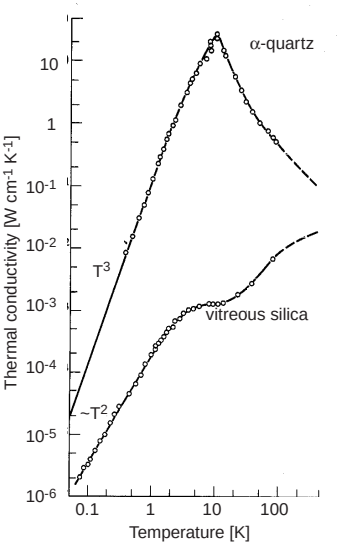

Figure 2-19. Thermal conductivity of vitreous silica compared with that of quartz [30].

Sound velocity and sound attenuation

First, let note that by sound we also mean here the vibrations sometimes classified as ultrasounds (MHz range) and hypersounds (GHz range). The figures 2-20 and 2-21 summarize the evolution of the sound velocity and of the ultrasonic absorption from very low *T* up to 1000 °C. These were recorded with Brillouin scattering experiments, that will be explained at length in the next chapter. For the time being, suffice it to say that the sound velocity is proportional[1] to the frequency shift and the attenuation proportional to the linewidth, thus enabling a quasi continuous reading of the curves in the left and right parts of the pictures despite the change of vertical scales.

1. At least as long as the refractive index can be considered a constant. Over such a wide temperature range, this is questionable, but the error is still reasonably small. See section 4.3.5.

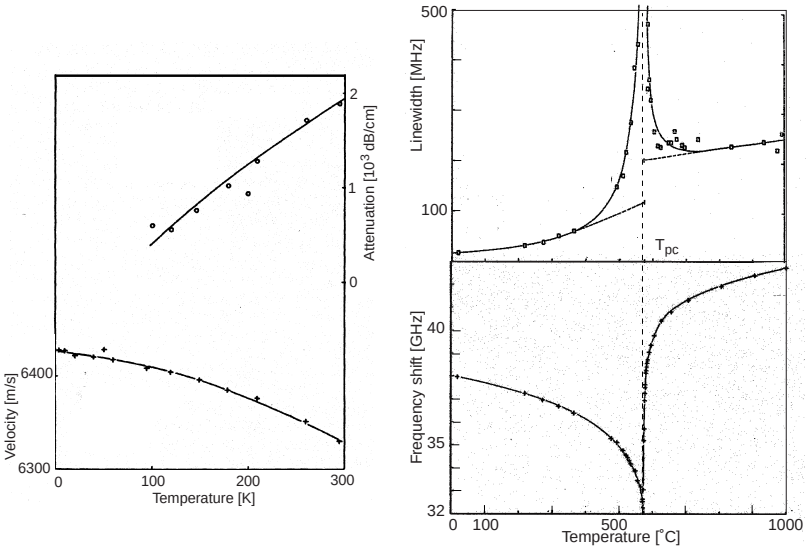

Figure 2-20. Velocity and attenuation of longitudinal hypersound waves in crystal quartz measured by Brillouin scattering. Left : cryogenic measurements at 40 GHz [39]; right : high-temperature measurements at 35 GHz [40]. T_{pc}=573°C corresponds to the phase transition between α- and β-quartz.

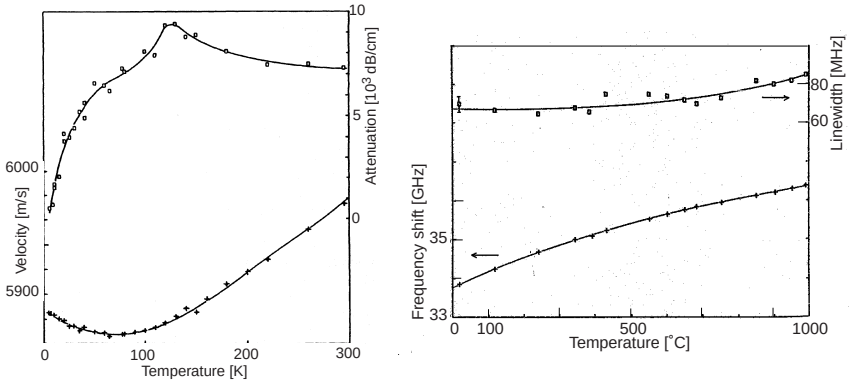

Figure 2-21. Same measurements on vitreous silica, from the same sources.

We will not lay stress on the singularities at T=573°C in 2-20, since the change of crystalline phases are out of the scope of this work. Besides, the behavior in the highest temperature range does once again not deserve any particular attention here, since there are no qualitative discrepancies between the two cases : both sound velocity and sound absorption increase slightly and continuously. For the glass, this smoothness carries on even through the glass transition into the viscous melt : measurements [41] up to 2300°C gave a mere prolongation of the curve in the right part of 2-21.

Below the ambient temperature, the sound velocity (and incidentally the dielectric constant that mimics closely its behavior) in a-SiO_2 shows variations which are large compared with those of pure crystal. The most evident difference in 2-21 is the broad minimum around 70 K instead of the weak quasi-constant negative coefficient of quartz. Below, the increase of velocity with decreasing temperature continues until a frequency dependent maximum is reached (not represented). For the experiments reported here this maximum occurs at 6 K, but it is for example shifted to 1.5 K at 30 MHz. At still lower temperatures the relative variation of velocity varies with the logarithm of T until a second shallow minimum.

As far as the attenuation is concerned, the first thing to notice is that it is strongly enhanced in glasses compared to crystals (do not overlook the different vertical scales). Moreover an absorption peak occurs at about 110 K. The position of this maximum is also frequency dependent, drifting toward lower temperatures for smaller frequencies : by plotting the frequency vs. the inverse of the peak temperature (a so-called Arrhenius plot), one gets a straight line [33] (see also section 4.3.5).

Density of states

As promised in section 2.5.2, we finish this short review of experimental results about a-SiO_2 with two examples of measured densities of states. The first one (figure 2-22) was obtained with a Raman scattering experiment. The figure shows also for comparison the Raman spectrum of crystalline silica. The expected transformation of a discrete spectrum into a continuous one, that is a fingerprint of the apparition of disorder, is obvious. The second example spans a wider wave number range up to 1500 cm^{-1} and is the result of neutron scattering. The effective lower limit of the spectrum is imposed by the installation providing

the neutrons and is evaluated at 120 cm^{-1}.The overall agreement of the curves in the region of superposition is pretty fair in this case.

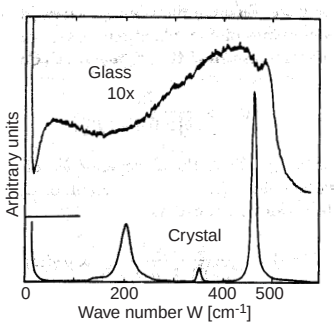

Figure 2-22. The reduced Raman spectra of vitreous and crystalline silica. [26].

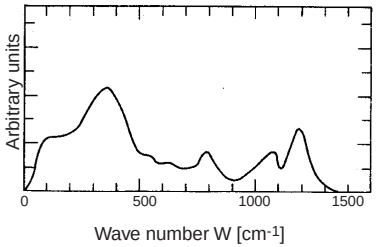

Figure 2-23. Vibrational DOS of vitreous silica measured by inelastic neutron scattering. From [25]

It is clear that there is indeed a lot of information about the structure of glasses and other physical features in the details of the spectra obtained with neutron, X-ray or Raman scattering, but it is also a formidable task to disentangle it. This can be undertaken with modern high quality simulations [42].

2.5.4 Theoretical models : extended and localized states

The new experimental evidences published in the early 1970's triggered immediately a considerable theoretical effort [43] aimed at understanding the properties of glasses, especially in the low-temperature range where they are on the one hand strikingly different from those of crystals and on the other hand universal among the amorphous solids. The most successful model was proposed independently by Anderson [44] and Phillips [45] and has been known since then as 'tunneling state' or 'two-level systems' model (TLS). Under its initial form, it was already able to explain qualitatively the anomalous heat capacity and thermal

transport coefficient, as well as other measured peculiarities. Subsequent experiments showed the necessity of refining and completing it, but it remains today by far the most used framework for the interpretation of the measurements on glasses. Next to the unavoidable book edited by Phillips [33], several monographs and many review papers are devoted to the presentation of this family of models, for example [34, 35, 42, 46]. For the present short survey, we mainly rely upon Galperin [46] and Elliott [3].

Two-level systems and low-temperature heat capacity

The tunneling state model[1] takes as its central hypothesis the assumption that, in a glassy system, a certain number of atoms (or groups of atoms) can occupy one of two local equilibrium positions; the atoms can tunnel between these positions and therefore move within a double-well potential such as that shown in figure 2-24. In general, such a potential will be asymmetric, characterized by an asymmetry energy Δ and a barrier height *V*, both of which being random quantities in view of the variable local structure of glass. The energy difference *E* between the two lowest states E_0 and E_1 of the double well (which is its excitation energy) is given by

$$E^2 = \Delta^2 + \Delta_0^2, \tag{2.14}$$

where Δ_0, the barrier strength is related to the parameters of the well by

$$\Delta_0 = \hbar\omega_0 \exp(-\lambda), \text{ with } \lambda = d\sqrt{(2mV)/\hbar^2}. \tag{2.15}$$

Here ω_0 is the frequency of oscillation in an individual well. Δ and λ are distributed randomly over an interval, their distribution being described by

$$P(\Delta, \lambda)d\Delta d\lambda = \bar{P}d\Delta d\lambda \text{ , for } |\Delta| \le \Delta_{max} \text{ and } \lambda_{min} \le \lambda \le \lambda_{max}. \tag{2.16}$$

With this distribution, the density of states for the TLS exhibits only a logarithmic dependence on energy, and it can be often considered as uniform :

$$n(E) = \bar{P}\log\left(\frac{2E}{\Delta_{0min}}\right), \text{ with } \Delta_{0min} = \hbar\omega_0 \exp(-\lambda_{max}). \tag{2.17}$$

1. Here we will use indifferently the expressions ‘tunneling state’ and ‘two-level system’, although a two-level system is strictly speaking only a particular case of tunneling state (see chapter 1 of [33] or [3], p. 165).

If the only present vibrational modes in a solid are TLSs, it can be shown that the specific heat is given by the following integration over them :

$$c_V = k_B \int_0^\infty n(E) \left(\frac{E}{2k_B T}\right) \operatorname{sech}^2 \left(\frac{E}{2k_B T}\right) dE . \qquad (2.18)$$

According to (2.17), *n(E)* can be taken to be a constant n_0 for the range of energies of interest ($10^{-5} < E < 10^{-4}$ eV). The evaluation of (2.18) gives then

$$c_V = \frac{\pi^2}{6} k_B^2 n_0 T , \qquad (2.19)$$

which accounts naturally for the linear variation of the specific heat of glasses at very low temperatures.

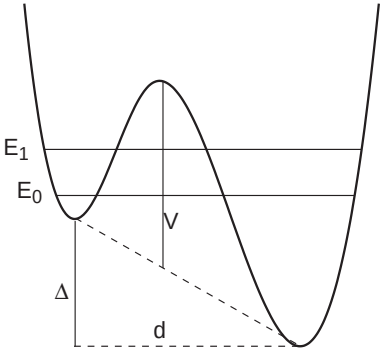

Figure 2-24. Schematic illustration of the double-well potential characterizing a two-level system plotted as a function of a suitable generalized coordinate, what is an elegant way of hiding the fact that the microscopical nature of the state is unknown.

Thermal conductivity and sound transport

To obtain the thermal conductivity and the acoustic absorption, we must take into account the interaction of the TLSs with the phonons[1]. It is mediated by the strain generated by the displacement u of the medium, described by the tensor $u_{ik} = \partial u_i / \partial x_k + \partial u_k / \partial x_i$. It is usually written in terms of the deformation potentials [46]

1. In accordance with section 2.5.1, phonon takes here its loose meaning of propagating vibrational mode of low frequency.

$$\begin{aligned} D_{ik} &= \frac{\partial E}{\partial u_{ik}} = \frac{\Delta}{E}\frac{\partial \Delta}{\partial u_{ik}} + \frac{\Delta_0}{E}\frac{\partial \Delta_0}{\partial u_{ik}} \\ 2M_{ik} &= \frac{\Delta_0}{E}\frac{\partial \Delta}{\partial u_{ik}} - \frac{\Delta}{E}\frac{\partial \Delta_0}{\partial u_{ik}} \end{aligned} \quad . \tag{2.20}$$

The first quantity describes the modulation of E under the influence of a deformation, while the second describes the direct transition between the states of the TLS.

This interaction results in a scattering of propagating phonons by the localized TLSs and limits the mean free path l of the former. Actually phonons of energy $\hbar\omega = E$, corresponding to the tunnel splitting, can be scattered by a process of excitation from the ground state (absorption of a phonon) and subsequent spontaneous decay (emission of an incoherent phonon). Such a process is called 'resonant scattering' and the resulting mean free path takes the form

$$l_{res}(\omega) = \frac{\rho v^3}{\pi n_0 M^2 \omega} \coth\left(\frac{\hbar\omega}{2k_B T}\right), \tag{2.21}$$

where ρ is the density of material, n_0 is the constant density of tunneling states already used in (2.19), v the average velocity of phonons and M the average value of the deformation potential (2.20). Since $\hbar\omega \sim k_B T$ for thermal phonons, the mean free path is proportional to T at low temperatures : $l_{res} \propto T$. Substituting this relation into the equation for thermal transport κ (2.13), we get the temperature dependence $\kappa \sim T^2$ in accordance with the measurements.

The resonant scattering mechanism is thus able to explain the initial growth of κ as a function of temperature represented in the figure 2-19, but not the subsequent plateau. For this, we have to resort to a second, non-resonant scattering mechanism initially considered by Jäckle [47] : the modulation of the interlevel spacing E of the tunneling systems due to the strain produced by the acoustic wave results in a periodic deviation of the level populations from their equilibrium value $\frac{1}{1+\exp(E/T)}$. The relaxation of the levels takes place at a rate τ. This process yields a relaxational mean free path $l_{rel} \propto T^{-3}$. The net mean free path given by $l_{TLS}^{-1} = l_{res}^{-1} + l_{rel}^{-1}$ explains qualitatively, when included in (2.13), the appearance of the plateau in thermal conductivity[1].

The variation of the sound velocity as well as that of acoustic absorption up to the plateau region can also be readily understood thanks to the mechanisms of resonant and relaxational scatterings of phonons by localized TLSs [33].

The frequency dependency of the mean free path of harmonic vibrations has not even be mentioned so far. This over-simplification can not be maintained anymore, if the nearly linear increase in $\kappa(T)$ above the plateau region is to be understood. It has been suggested [33] that $l(\omega)$ varies slowly at low frequency but undergoes a rapid drop for a frequency range close to the plateau ($\sim 10^{11}$ - 10^{12} Hz) and is essentially zero afterwards. The modes of vibration still exist at higher frequencies, as evidenced by the DOS spectra, but they become purely diffusive. Some authors introduce a new terminology at this point, speaking of diffusons or fractons [48] for this kind of modes. Amorphous materials behave thus as low-pass filters, and the vast majority of heat carriers should be low-frequency phonons typically characteristic of a temperature near 2 K, even if the actual temperature lies beyond 20 K. What is observed however is that the diffusons contribute to heat transport through a process called phonon-assisted fracton hopping. The process is anharmonic and its description requires a quantum treatment [49, 50]. This theory is able to explain the linear increase in $\kappa(T)$ between ~10 and 60 K, but also the linear decrease in the sound velocity and the related variation of the acoustic absorption measured over the same temperature span [48] (see figure 2-21).

The maximum of the acoustic absorption around 110 K, often called the boson peak, is attributed to thermally activated structural relaxations [51]. We will go back over it in the experimental part of this work.

Strangely, the linear increase of the sound velocity from its minimum around 60 K up to nearly the glass transition temperature (figure 2-21) is perhaps the least well understood part of all the experimental curves we have presented : only a vague link to a similar increase in elastic constants [48], presumably related to density fluctuations. There is clearly a gap in our knowledge here, a sadly ill-placed gap since many of the experiments we have realized concern this variation.

---

1. For quantitative agreement, more sophisticated models are required, including non-uniform distributions of the parameters τ, $n(E)$, Δ, M...

Microscopic nature of tunneling states

Tunneling states were initially proposed as an empirical ad-hoc model that allowed the calculation of physical quantities in glasses and the comparison of different experiments. But in spite of its success and of its wide acceptance in the scientific community, it has suffered for a long time from a quite embarrassing weakness : not only nobody had ever seen a real, physical TLS, but nobody knew for sure what it looks like. Of course there were numerous suggestions, but none of them could claim univocal support from the measurements. In a-SiO_2, the simplest candidate was a single oxygen atom flipping between two quasi-equivalent metastable positions, either along a Si-Si interval or perpendicular to it. Numerical simulations [17, 52] seem today to indicate that such a move, albeit not totally impossible, is much less probable than the coupled rotation of a small group of SiO_4 tetrahedra (figure 2-25).

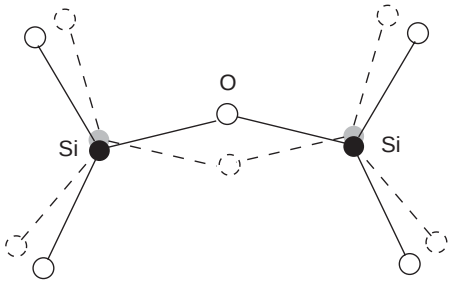

Figure 2-25. The two states of a possible two-level system in vitreous silica: coupled rotation of undeformed SiO_4 tetrahedra.

Shortcomings of the present models

The variety of the vibrational modes in a glass is baffling. To avoid confusion, some authors [42] even suggest the use of the following terminology, by increasing order of frequency :

- extended propagating modes are propagons
- extended diffusing modes diffusons
- localized diffusing modes locons.

On top of these harmonic modes come the tunneling states, localized by nature.

To understand the behavior of glasses, the intricate interactions between all these vibrational modes and, if necessary, external perturbations like electromagnetic fields or applied strains, have to be taken into account. In view of its complexity, the domain is a very active field, and it is likely to remain so for a while. For the

time being, most of the fundamental open questions are somewhat related to the intermediate spatial scale, say between 3 and 15 nm. We have seen that it is the scale at which disorder arises, yet there are indications of subsisting partial order. Unfortunately, this is also the scale at which all the available experimental techniques reach their limits or fail to deliver meaningful results.

It is certain that localized vibrations like tunneling state systems do exist in a-SiO_2. But it is also probable that the model in its present form is over-simplified. Some authors [53, 54] suggest to take into account the interaction between TLSs[1]; for others [46] the harmonic double-well have to be replaced by anharmonic potentials.

Other problems involve non-uniformity of the material : some measurements [55] seem to indicate that the often encountered OH impurities create extrinsic tunneling states, which change the properties of the silica. GeO_2, routinely used as dopant in silica-based glass for optical fibers, has the same tetrahedral short-scale order as SiO_2, but the length of the Ge-O liaison is different. How to relate this microscopic discrepancy with macroscopic changes in the sound velocity or the refractive index ?

As our intent in this chapter was only to survey those aspects of the physics of amorphous physics relevant for the study of Brillouin scattering in silica, we leave these questions open and turn now to optics to tackle the main topic of this thesis.

1. They are usually considered as isolated.

References

[1] *D. Weaire, F. Wooten*
The inextricably entangled skein
in *Physics of disordered materials*, D. Adler, H. Fritzsche, and S.R. Ovshinsky, Editors, Plenum Press, New York (1985).

[2] *N.F. Mott*
Electrons in glass, 1977 Nobel Prize lecture
Science, **201**, p. 871-875 (1978).

[3] *S.R. Elliott*
Physics of amorphous materials
Longman Inc., New York (1983).

[4] *H. Scholze*
Glass : nature, structure, and properties
Springer, New York (1991).

[5] *I. Gutzow, J. Schmelzer*
The vitreous state : thermodynamics, structure, rheology, and crystallization
Springer, Berlin (1995).

[6] *G.P. Agrawal*
Nonlinear fiber optics
2nd ed. Academic Press, San Diego (1995).

[7] *J. Classen, I. Rohr, C. Enss, S. Hunklinger*
Low frequency elastic properties of neutron-irradiated quartz. Comparison with glasses
Europ. Phys. J. B, **10**(4), p. 623-633 (1999).

[8] **McGraw-Hill Encyclopedia of Science & Technology**
7th ed. McGraw-Hill, New York (1997).

[9] *N.W. Ashcroft, N.D. Mermin*
Solid state physics
Saunders, Philadelphia (1976).

[10] *J. Sanz*
NMR techniques for the study of crystalline and amorphous solids
in *Defects and disorder in crystalline and amorphous solids*, C.R.A. Catlow, Editor, Kluwer, Dordrecht (1994).

[11] *C.R.A. Catlow ed*
Defects and disorder in crystalline and amorphous solids
Kluwer, Dordrecht (1994).

[12] *W.H. Zachariasen*
The atomic arrangement in glass
J. Am. Chem. Soc., **54**, p. 3841-3851 (1932).

[13] *F.L. Galeener*
Current models for amorphous SiO2
in *The physics and technology of amorphous SiO2*, R.A.B. Devine, Editor, Plenum Press, New York (1987).

[14] *R.J. Bell, P. Dean*
Properties of vitreous silica : analysis of random network models
Nature, **212**, p. 1354-1356 (1966).

[15] *R.J. Bell, P. Dean*
The structure of vitreous silica : validity of the random network theory
Phil. Mag., **25**, p. 1381-1398 (1972).

[16] *G.N. Greaves*
Random network models
in *Defects and disorder in crystalline and amorphous solids*, C.R.A. Catlow, Editor, Kluwer, Dordrecht (1994).

[17] *S.N. Taraskin, S.R. Elliott*
Nature of vibrational excitations in vitreous silica
Phys. Rev. B, **56**(14), p. 8605-8622 (1997).

[18] *P.H. Gaskell*
Medium-range order and random networks
J. Non-Cryst. Solids, **293**, p. 146-152 (2001).

[19] *P.H. Gaskell, D.J. Wallis*
Medium-range order in silica, the canonical network glass
Phys. Rev. Lett., **76**(1), p. 66-69 (1996).

[20] *S.R. Elliott*
The origin of the first sharp diffraction peak in the structure factor of covalent glasses and liquids
J. Phys. Cond. Matter, **4**(38), p. 7661-7678 (1992).

[21] *S.R. Elliott*
Origin of the first sharp diffraction peak in the structure factor of covalent glasses
Phys. Rev. Lett., **67**, p. 711-713 (1991).

[22] *A.P. Sokolov, A. Kisliuk, M. Soltwisch, D. Quitmann*
Medium-range order in glasses : comparison of Raman and diffraction measurements
Phys. Rev. Lett., **69**(10), p. 1540-1543 (1992).

[23] A.A. Lebedev
Über Polymorphismus und das Kühlen von Glass (1921).

[24] *D. Weaire, P.C. Taylor*
Vibrational properties of amorphous solids
in *Dynamical properties of solids*, G.K. Horton and A.A. Maradudin, Editors, North Holland, Amsterdam (1980).

[25] *F.L. Galeener, A.J. Leadbetter, M.W. Stringfellow*
Comparison of the neutron, Raman, and infrared vibrational spectra of vitreous SiO2, GeO2, and BeF2
Phys. Rev. B, **27**(2), p. 1052-1078 (1983).

[26] *G.P. Srivastava*
The physics of phonons
Adam Hilger, Bristol (1990).

[27] *J. Jäckle*
Low-frequency Raman scattering in glasses
in *Amorphous solids : low-temperature properties*, W.A. Philips, Editor, Springer, Berlin (1981).

[28] *S. Ballaro, G. Cubiotti, M. Cutroni, S. Frassica, W. Wanderlingh*
Sound velocity and absorption in amorphous silica
Nuovo Cimento, **25B**(1), p. 13-27 (1975).

[29] *S. Rau, C. Enss, S. Hunklinger, P. Neu, A. Würger*
Acoustic properties of oxide glasses at low-temperatures
Phys. Rev. B, **52**(10), p. 7179-7194 (1995).

[30] *R.C. Zeller, R.O. Pohl*
Thermal conductivity and specific heat of noncrystalline solids
Phys. Rev. B, **4**(6), p. 2029-2041 (1971).

[31] *S.N. Taraskin, S.R. Elliott*
Phonons in vitreous silica: Dispersion and localization
Europhys. Lett., **39**(1), p. 37-42 (1997).

[32] *C. Oligschleger*
Dynamics of SiO2 glasses
Phys. Rev. B, **60**(5), p. 3182-3193 (1999).

[33] *W.A. Phillips ed*
Amorphous solids : low-temperature properties
Topics in current physics. Vol. 24, Springer, Berlin (1981).

[34] *P. Esquinazi ed*
Tunneling systems in amorphous and crystalline solids
Springer, Berlin (1998).

[35] *A. Würger*
From coherent tunneling to relaxation
Springer tracts in modern physics. Vol. 135, Springer, Berlin (1997).

[36] *R.A.B. Devine ed*
The physics and technology of amorphous SiO2
Plenum Press, New York (1987).

[37] *D. Richter, A.J. Dianoux, W. Petry, J. Teixera ed*
Dynamics of disordered materials
Springer, Berlin (1989).

[38] *L.D. Pye, W.C. LaCourse, H.J. Stevens ed*
The physics of non-crystalline solids
Taylor & Francis, London (1992).

[39] *R. Vacher, J. Pelous*
Behavior of thermal phonons in amorphous media from 4 to 300 K
Phys. Rev. B, **14**(2), p. 823-828 (1976).

[40] *J. Pelous, R. Vacher*
Thermal Brillouin scattering in crystalline and fused quartz from 20 to 1000 degrees C
Solid State Commun., **18**(5), p. 657-661 (1976).

[41] *A. Polian, D. Vo-Thanh, P. Richet*
Elastic properties of a-SiO2 up to 2300 K from Brillouin scattering measurements
Europhys. Lett., **57**(3), p. 375-381 (2002).

[42] *E. Courtens, M. Forêt, B. Hehlen, R. Vacher*
The vibrational modes of glasses
Solid State Commun., **117**(3), p. 187-200 (2001).

[43] *M.R. Vukcevich*
A new interpretation of the anomalous properties of vitreous silica
J. Non-crystal. Solids, **11**, p. 25-63 (1971).

[44] *P.W. Anderson, B.I. Halperin, C.M. Varma*
Anomalous low-temperature thermal properties of glasses and spin glasses
Philos. Mag., **25**, p. 1-9 (1972).

[45] *W.A. Phillips*
Tunneling states in amorphous solids
J. Low Temp. Phys., **7**(3/4), p. 351-360 (1972).

[46] *Y.M. Galperin, V.G. Karpov, V.I. Kozub*
Localized states in glasses
Adv. Phys., **38**(6), p. 669-737 (1989).

[47] *J. Jäckle*
Ultrasonic Attenuation in Glasses at Low-Temperatures
Z. Phys., **257**(3), p. 212-223 (1972).

[48] *A. Jagannathan, R. Orbach*
Temperature and frequency dependence of the sound velocity in vitreous silica due to scattering off localized modes
Phys. Rev. B, **41**(5), p. 3153-3157 (1990).

[49] *S. Alexander, C. Laermans, R. Orbach, H.M. Rosenberg*
Fracton interpretation of vibrational properties of cross-linked polymers, glasses, and irradiated quartz
Phys. Rev, B, **28**, p. 4615-4619 (1983).

[50] *S. Alexander, O. Entin-Wohlman, R. Orbach*
Phonon-fracton anharmonic interactions: The thermal conductivity of amorphous materials
Phys. Rev, B, **34**, p. 2726-2734 (1986).

[51] *J.P. Bonnet*
On the thermally activated structural relaxation in glasses
J. Non-Cryst. Solids, **127**(2), p. 227-231 (1991).

[52] *A. Heuer, R.J. Silbey*
Collective dynamics in glasses and its relation to the low-temperature anomalies
Phys. Rev. B, **53**(2), p. 609-619 (1996).

[53] *C. Enss, S. Hunklinger*
Incoherent tunneling in glasses at very low temperatures
Phys. Rev. Lett., **79**(15), p. 2831-2834 (1997).

[54] *S. Hunklinger, C. Enss, P. Strehlow*
Quantum phenomena in glasses at low temperatures
Physica B, **280**(1), p. 271-275 (2000).

[55] *B. Golding, M. v. Schickfus, S. Hunklinger, K. Dransfeld*
Intrinsic electric dipole moment of tunneling systems in silica glasses
Phys. Rev. Lett., **43**(24), p. 1817-1821 (1979).

CHAPTER 3

Brillouin scattering

The developments in this chapter owe much to the monographs *Nonlinear fiber optics* [1] by G. P. Agrawal and *Nonlinear optics* [2] by R. W. Boyd, and still more to the Ph.D. theses of M. Niklès and M. Facchini [3, 4].

3.1 Introduction

Bluntly asked whether sound can deflect light, very few people would spontaneously answer yes. Indeed, in our everyday experience, there are no signs of a possible interaction of optical and acoustic waves, both living in well separated domains. Nevertheless, the interaction of light (by which we also mean those frequencies of the electromagnetic spectrum that do not belong to the visible range) and matter (mostly atoms, but other scales have to be taken into account, from nuclei and electrons to molecules or macroscopic samples) makes up for most of the physical sciences; since sound waves are simply variations of material quantities, equivalently expressed in terms of thermodynamic values like pressure, density, entropy, or in terms of microscopic atomic positions, an influence of these variations upon the mechanisms of the light-matter interaction cannot be ruled out. Actually, it should even be expected.

Due to the weakness of this influence[1], it was not suspected, even less studied, before the XXth century. Léon Brillouin first considered theoretically in 1922 the thermal density fluctuations as a mechanism responsible for the scattering of light by an homogeneous medium [5]. He emphasized the case of X-ray scattering and suggested relevant experiments in this frequency range. This application turned out to be wrongly chosen, since electronic density changes due to the molecular structure are there much more important than thermal fluctuations. However, his theory led to remarkable results for visible light and was experi-

1. For a few more lines, we stick to general terms, intending to be more precise further.

mentally proved right by Debye [6] in 1932, with measurements on liquids : in the spectrum of the scattered light, he found the predicted components due to the scattering of the incident lightwave by an externally applied sound wave.

The Brillouin effect, or spontaneous Brillouin scattering, as this phenomenon became named, remained essentially a laboratory curiosity until the 1960's. At most, it provided a way to measure the sound velocity in some mediums The advent of lasers changed the situation. Among the fields of research that were opened by the wide availability of intense coherent lightwaves, nonlinear optics was prominent. Stimulated processes, much more efficient than their spontaneous counterparts, were observed, including stimulated Brillouin scattering (SBS) in crystals by Chiao *et al.* [7]. Finally, to get closer to our subject, SBS was also observed in optical fibers shortly after the invention of the first low-loss fibers [8].

To put Brillouin scattering into perspective, we will begin far upstream in the theory, namely with Maxwell's equations in vacuum, and stride along the polarizability of a medium and the overall spontaneous scattered spectrum. After the description of spontaneous Brillouin scattering, we will proceed with the stimulated one, emphasizing the role of electrostriction, and derive the equations describing the Brillouin gain in general. The peculiarities of SBS in optical fibers will be the topic of the next section, while the last part of the chapter will be devoted to the influence of external parameters on SBS in fibers, with the exception of the dependence on temperature, which is the subject of chapter 4.

3.2 Linear light scattering

3.2.1 Generalities

In the course of history, speculations about the nature of light have been numerous and diverse. The importance of light in the way we perceive the everyday world is impossible to overstate, as can not be neglected the innumerable metaphors and myths it becomes involved in. Actually it is such a central topic that an historical essay on its nature like that of Park [9] comes very close to be a survey of the evolution of human culture as a whole. The present understanding of light, albeit safely anchored in the scientific method, is perhaps as odd as the most

baroque mythological constructions of the past : since Young's interference experiments, we know that light is a wave, and the great unification of phenomena related to electricity and magnetism engraved in Maxwell's laws specifies that it is an electromagnetic propagating wave [10]. In the same time, light behaves also as discrete particles, and devices as common as lasers originate in the quantum theory of photons [11]. We have to live with this disturbing duality[1]; we can even take advantage of it by choosing between the two points of view the best suited one to the description of a given phenomenon.

For the light propagation in vacuum, there is no doubt that the wave description is adequate. Starting from Maxwell's equations in differential form

$$\begin{aligned} \nabla \boldsymbol{E} &= \frac{\rho}{\varepsilon_0} \\ \nabla \times \boldsymbol{E} &= -\frac{\partial \boldsymbol{B}}{\partial t} \\ \nabla \boldsymbol{B} &= 0 \\ \nabla \times \boldsymbol{B} &= \mu_0\left(\varepsilon_0 \frac{\partial \boldsymbol{E}}{\partial t} + \boldsymbol{J}\right) \end{aligned} \quad , \tag{3.1}$$

we get, in the absence of charges and currents, the wave equation

$$\nabla^2 \boldsymbol{E} - \frac{1}{c_0^2} \cdot \frac{\partial^2 \boldsymbol{E}}{\partial t^2} = 0 \tag{3.2}$$

with $c_0 = (\mu_0 \varepsilon_0)^{-1/2} \approx 3 \times 10^8 \mathrm{m} \cdot \mathrm{s}^{-1}$ the velocity of light.

The presence of matter alters the propagation. A polarization field $\boldsymbol{P}$ appears, describing the reaction of the material to the wave :

$$\nabla^2 \boldsymbol{E} - \frac{1}{c_0^2} \cdot \frac{\partial^2 \boldsymbol{E}}{\partial t^2} = \mu_0 \frac{\partial^2 \boldsymbol{P}}{\partial t^2} \tag{3.3}$$

In an homogeneous isotropic medium, the polarization is proportional[2] to the applied electric field : $\boldsymbol{P} = \varepsilon_0 \chi \boldsymbol{E}$. The proportionality factor χ is the dielectric

1. The discussions about this apparent duality, the presumed unicity of nature and the way the mind works are fascinating, but they would pertain to the philosophy of sciences, and thus not to this work.

susceptibility of the medium. Taking into account this linear dependence, (3.3) becomes

$$\nabla^2 \boldsymbol{E} - \frac{n^2}{c_0^2} \cdot \frac{\partial^2 \boldsymbol{E}}{\partial t^2} = 0. \tag{3.4}$$

Here $n = \sqrt{1+\chi} = \sqrt{\varepsilon/\varepsilon_0}$ is the refractive index, ε being the dielectric constant. The only difference between (3.2) and (3.4) is the light velocity : in a medium c_0 has to be replaced by $c = c_0/n$, but the light propagates always straight ahead. Nevertheless, a real medium is neither homogeneous nor isotropic; liquids for example, although homogeneous at the macroscopic scale, present microscopical variations of density. Moreover, all matter is ultimately made of atoms, so it is inhomogeneous at the corresponding scale ($\sim 10^{-10}$ m). The constant scalar dielectric susceptibility χ must be replaced by a tensor $\chi + \underline{\Delta\chi}(\boldsymbol{r}, t)$, so that $\boldsymbol{P} = \varepsilon_0 \chi \boldsymbol{E} + \varepsilon_0 \underline{\Delta\chi} \boldsymbol{E} = \varepsilon_0 \chi \boldsymbol{E} + \underline{\Delta\varepsilon} \boldsymbol{E}$, adding a source term in (3.4) :

$$\nabla^2 \boldsymbol{E} - \frac{n^2}{c_0^2} \cdot \frac{\partial^2 \boldsymbol{E}}{\partial t^2} = \mu_0 \frac{\partial^2}{\partial t^2} (\underline{\Delta\varepsilon} \boldsymbol{E}) \tag{3.5}$$

The right hand side of this perturbed wave equation conceals different scattering mechanisms. To disentangle them, it is useful to distinguish between scalar and tensorial contributions in each element $\Delta\varepsilon_{ij}$ of $\underline{\Delta\varepsilon}$:

$$\Delta\varepsilon_{ij} = \Delta\varepsilon\delta_{ij} + \Delta\varepsilon_{ij}^t \tag{3.6}$$

The diagonal, scalar term $\Delta\varepsilon$ describes the fluctuations in thermodynamic quantities like density, temperature, entropy or pressure. It generates Brillouin and Rayleigh scatterings.

The purely out-of-diagonal terms can in turn be decomposed in a symmetric and an anti-symmetric contributions, both statistically independent. The symmetric part is responsible for Rayleigh-wing scattering, while the anti-symmetric one causes Raman scattering. Both are related to the optical polarizability of the medium [12].

2. If the light intensity is kept low enough so that the linear approximation remains valid. For the opposite case, see section 3.3.1.

3.2.2 Scattered spectrum

Under the most general circumstances, the spectrum of the light scattered by a medium has the form schematized in figure 3-1. Rayleigh, Brillouin, Raman and Rayleigh-wing features are present. Note that the peaks are not properly scaled, as evidenced by the parameters gathered in table 3.1: Raman peaks for instance should be 10^3 times more distant from the incident frequency than the Brillouin peaks, and their linewidths should present the same ratio. By definition, components that are down-shifted in frequency are called Stokes components, the label anti-Stokes being quite logically attached to those components shifted to higher frequencies than that of the incident lightwave.

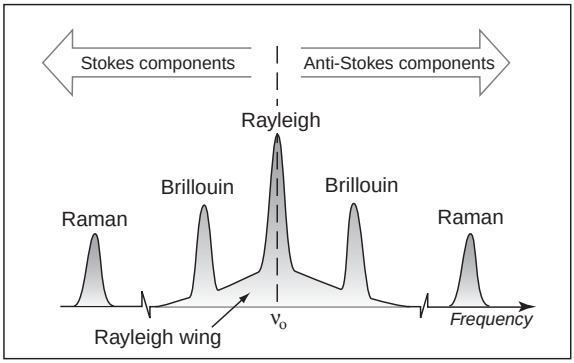

Figure 3-1. Typical components of the spectrum of scattered light (not scaled; see text and table 3.1).

Process	Shift [cm^{-1}]	Linewidth [cm^{-1}]	Relaxation time [s]	Gain [m/W]
Raman	1000	5	10^{-12}	10^{-13}
Brillouin	1	5×10^{-3}	10^{-9}	2×10^{-11}
Rayleigh	0	5×10^{-4}	10^{-8}	
Rayleigh-wing	0	5	10^{-12}	

Table 3.1. Typical values of the parameters describing several light scattering processes in fluids. The gain concerns the stimulated version of the processes in silica.

The percentage of light that gets scattered remains usually low, even when the effect of all mechanisms add up. It can be expressed in terms of scattering coeffi-

cient R or scattering cross section σ. R is the constant of proportionality relating the scattered intensity I_s, measured at a distance L of an interaction volume V, and the incident intensity I_0 :

$$I_s = \frac{I_0 R V}{L^2}. \tag{3.7}$$

R is in general a function of the scattering angle. As a numerical example, $R = 2 \times 10^{-8}$ cm^{-1} in air (for visible light and through an angle of 90°) and $R = 1 \times 10^{-6}$ cm^{-1} in water. Integrated over all the scattering angles, this last value amounts to saying that approximately one part in 10^5 of the power contained in a beam would be scattered in passing through 1 cm of water. The total scattering cross section σ has the dimensions of an area and is defined simply by $P = \sigma I_0$, where P is the total power of scattered radiation. The more informative differential cross section describes the power dP scattered in some particular direction into the solid angle $d\Omega$:

$$\frac{dP}{d\Omega} = I_0 \frac{d\sigma}{d\Omega}. \tag{3.8}$$

The diversity of the values of parameters in table 3.1 implies that entirely different processes come into play, differences in the time scales being specially notable. Here is a brief review of the physical origins of the features in the scattered spectrum.

Rayleigh scattering is due to non propagating density fluctuations. Formally, it arises from fluctuations of the entropy (see section 3.2.3). Since there is no frequency shift induced by the process, the energy of the lightwave is conserved and the scattering is elastic.

Brillouin scattering is generated by travelling density perturbations, i. e. by sound waves. In the language of phonons[1], it can be considered as the result of the interaction of light with acoustic phonons. The relatively low frequencies of these modes induce a limited frequency shift, in the 10^{10} Hz region.

Raman scattering results from the interaction of light with high-frequency vibrational modes of the molecules of the medium, or equivalently the optical phonons

1. A language that has to be cautiously used in amorphous solids (see section 2.5).

of the structure. The process is highly inelastic, yielding frequency shifts as high as 10^{14} Hz.

Rayleigh-wing scattering is scattering from fluctuations in the orientation of anisotropic molecules. The process is elastic and very rapid, hence the large spectral width of the corresponding peak.

The full description of the last two processes entails considerable difficulties and is anyway not directly relevant here. So letting them to the dedicated chapters in the books of Shen [12] or Fabelinskii [13], we concentrate on the scattering processes related to static and propagating density fluctuations.

3.2.3 Rayleigh scattering

In a dilute gas, the interaction of the molecules are sufficiently limited so that a microscopic theory of light scattering by individual molecules can be successful.[1] In a solid however a thermodynamical treatment is better-suited.

In the perturbed wave equation (3.5), we assume that the fluctuation of the dielectric constant $\Delta\varepsilon$ is scalar. Since the dielectric constant is mainly a function of density (the temperature dependence is much weaker), we can write

$$\Delta\varepsilon = \frac{\partial\varepsilon}{\partial\rho}\Delta\rho . \tag{3.9}$$

This is a good place to introduce the electrostrictive constant γ_e, defined as $\gamma_e = \rho_0 \frac{\partial\varepsilon}{\partial\rho}$. We then represent the density fluctuation $\Delta\rho$ in terms of pressure p and entropy s as :

$$\Delta\rho = \left(\frac{\partial\rho}{\partial p}\right)_s \Delta p + \left(\frac{\partial\rho}{\partial s}\right)_p \Delta s . \tag{3.10}$$

The first term describes adiabatic density fluctuations and leads to Brillouin scattering. The second one corresponds to isobaric density fluctuations, that is temperature or entropy variations at constant pressure. We will deal at first with this term, responsible for Rayleigh scattering.

Entropy fluctuations are described by the following equation :

1. In particular, it explains why the sky is blue.

$$\rho c_p \frac{\partial}{\partial t} \Delta s - \kappa \nabla^2 \Delta s = 0 . \tag{3.11}$$

In this diffusion equation, c_p denotes the specific heat at constant pressure and κ the thermal conductivity. A solution of (3.11) is

$$\Delta s = \Delta s_0 \exp(-\delta t) \exp(-i \boldsymbol{q} \cdot \boldsymbol{r}) \ , \tag{3.12}$$

where $\boldsymbol{q}$ is the scattered wave vector and the damping rate is $\delta = \frac{\kappa}{\rho c_p} q^2$. We see that this entropy wave does not propagate.

Now we replace Δs by its expression (3.12) in (3.10), then in (3.9) discarding the first term of (3.10), and we put finally this expression of $\Delta\varepsilon$ into the wave equation (3.5). With the assumption of a monochromatic incident wave

$$\boldsymbol{E}(\boldsymbol{r}, t) = \boldsymbol{E_0} \exp[i(\boldsymbol{k} \cdot \boldsymbol{r} - \omega t)] + \text{c.c.} , \tag{3.13}$$

where $\omega = |\boldsymbol{k}| \frac{c_0}{n}$, it is easy to see that the right hand side of (3.5), i.e. the additional polarization term, has only components with the frequency ω of the incident wave.

3.2.4 Spontaneous Brillouin scattering

The equation of motion for a pressure fluctuation Δp, first term in equation (3.10), is well-known from the field of acoustics :

$$\frac{\partial^2}{\partial t^2} \Delta p - \Gamma \nabla^2 \frac{\partial}{\partial t} \Delta p - v^2 \nabla^2 \Delta p = 0 \tag{3.14}$$

The damping parameter Γ will be neglected in a first time. The velocity of sound v can be expressed using thermodynamic variables as

$$v = \sqrt{\frac{K}{\rho}} = \sqrt{\frac{1}{C_s \rho}} \ ,$$

with K the bulk modulus and C_s the compressibility.

A solution of (3.14) is the propagating wave

$$\Delta p(\boldsymbol{r}, t) = \Delta p_0 \exp[i(\boldsymbol{q} \cdot \boldsymbol{r} - \Omega t)] + \text{c.c.} , \tag{3.15}$$

where the dispersion relation $\Omega = v|\boldsymbol{q}|$ is satisfied.
Again with the hypothesis (3.13) of a monochromatic incident lightwave, we insert (3.15) into (3.5) and get :

$$\nabla^2 \boldsymbol{E} - \frac{n^2}{c_0^2} \cdot \frac{\partial^2 \boldsymbol{E}}{\partial t^2} = -\frac{\gamma_e C_s}{c^2} \Delta p_0 E_0 \left[(\omega - \Omega)^2 \exp[i(\boldsymbol{k} - \boldsymbol{q}) \cdot \boldsymbol{r} - i(\omega - \Omega)t] \right. \quad (3.16)$$

$$\left. + (\omega + \Omega)^2 \exp[i(\boldsymbol{k} + \boldsymbol{q}) \cdot \boldsymbol{r} - i(\omega + \Omega)t] \right] + \text{c.c.}$$

The first term in the left part of (3.16) is an oscillating component with wave vector $\boldsymbol{k}' = \boldsymbol{k} - \boldsymbol{q}$ and frequency $\omega' = \omega - \Omega$. It generates the scattered wave

$$\boldsymbol{E_B}(\boldsymbol{r}, t) = \boldsymbol{E_{B0}} \exp[i(\boldsymbol{k}' \cdot \boldsymbol{r} - \omega' t)] + \text{c.c.} \quad (3.17)$$

The wave vectors and the frequencies of the three interacting waves (3.13), (3.15) and (3.17) have definite values that depend on the scattering direction considered, as illustrated in figure 3-2. The frequency Ω of the acoustic wave being much smaller than the optical frequencies involved, $|\boldsymbol{k}'| \approx |\boldsymbol{k}|$. The inset of figure 3-2 shows consequently that $|\boldsymbol{q}| = 2|\boldsymbol{k}| \sin(\theta/2)$, so that

$$\Omega = 2n \frac{v}{c} \omega \sin(\theta/2) \quad (3.18)$$

We note that the forward-scattered wave undergoes no frequency change, while the frequency shift is maximal for backscattering.

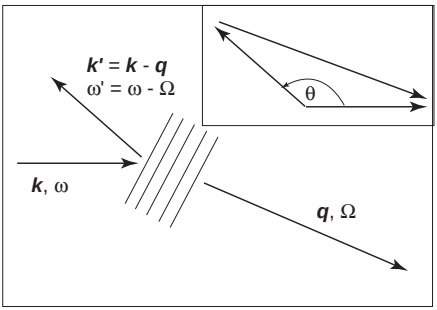

Figure 3-2. Illustration of Stokes scattering.

From a quantum point of view, the process may be considered as the absorption of an incident photon followed by the emission of a phonon and of a new photon with lower frequency. This last point explains why this is a Stokes scattering.

An analogous development can be carried out for the second term in (3.16). This time, the scattered wave has a wave vector $\boldsymbol{k}' = \boldsymbol{k} + \boldsymbol{q}$ and a frequency $\omega' = \omega + \Omega$. The relative orientations of the vectors are shown in figure 3-3.

This anti-Stokes scattering comes down to the simultaneous absorption of a phonon and an incident photon followed by the emission of a photon of higher energy.

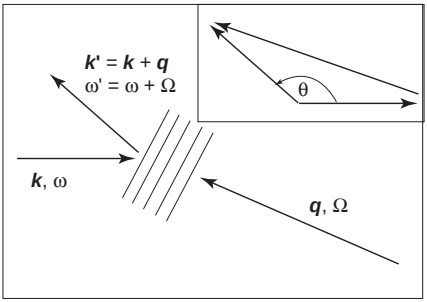

Figure 3-3. Illustration of anti-Stokes scattering.

If we remember now the damping parameter Γ in the sound wave equation (3.14), we find that the light scattered into direction θ has a frequency broadening with width

$$\delta\omega = \Gamma|\boldsymbol{q}|^2 = 4\Gamma n^2 \frac{\omega^2}{c_0^2} \sin^2(\theta/2). \tag{3.19}$$

The ratio of the linewidth to the frequency shift is given by

$$\frac{\delta\omega}{\Omega} = \frac{2n\Gamma\omega}{vc_0} \sin(\theta/2) \tag{3.20}$$

Due to the presence of Γ in (3.20), this experimentally easily measurable ratio is a direct measurement of the internal friction *Q* of a medium, itself inversely proportional to the acoustic absorption coefficient $\alpha = q^2\Gamma/v$. Alternative ways of describing the properties related to absorption are the phonon mean free path and the phonon lifetime $\tau_p = \frac{1}{q^2\Gamma}$.

3.3 Basics of Brillouin scattering

3.3.1 Nonlinear effects

Let us rewrite the fundamental equation describing wave propagation in a medium :

$$\nabla^2 \boldsymbol{E} - \frac{1}{c_0^2} \cdot \frac{\partial^2 \boldsymbol{E}}{\partial t^2} = \mu_0 \frac{\partial^2 \boldsymbol{P}}{\partial t^2} \tag{3.21}$$

In the previous sections, we confined ourselves to the linear approximation in which the induced polarization is proportional to the applied field. Each spectral component of the radiation (of the form (3.13)) remains unaffected by the presence of other components. But nature is never strictly linear, although its nonlinearities can sometimes be neglected. For high-intensity electromagnetic field, this is no longer possible. The relation between polarization and incident field has to be written as

$$\boldsymbol{P} = \varepsilon_0 [\chi^{(1)} \boldsymbol{E} + \chi^{(2)} \boldsymbol{E}^2 + \chi^{(3)} \boldsymbol{E}^3 + \ldots] \tag{3.22}$$

With this form of the polarization, (3.21) can be rewritten

$$\nabla^2 \boldsymbol{E} + \frac{\varepsilon^{(1)}}{c_0^2} \cdot \frac{\partial^2 \boldsymbol{E}}{\partial t^2} = \mu_0 \frac{\partial^2 \boldsymbol{P}^{NL}}{\partial t^2} \tag{3.23}$$

where $\varepsilon^{(1)} = 1+\chi^{(1)}$. All the linear terms lie on the left side of the equation. The nonlinear polarization (i.e. the terms of order 2 and more in $\boldsymbol{E}$) causes a coupling between the individual spectral components and, depending on the conditions, various physical effects : generation of new frequencies, modification of the refractive index, four-wave mixing, stimulated scatterings in several flavors... All of them are the core subjects of nonlinear optics and make the bulk of the books in the domain. To illustrate the impact of the introduction of the nonlinear susceptibilities $\chi^{(2)}$, $\chi^{(3)}$,... into (3.21), let us have a look at the simplest imaginable case, where we assume that the incident lightwave consists only of two monochromatic waves.

$$\boldsymbol{E}(\boldsymbol{r}, t) = \boldsymbol{E_1}(\boldsymbol{r}) \exp(-i\omega_1 t) + \boldsymbol{E_2}(\boldsymbol{r}) \exp(-i\omega_2 t) + \text{c.c} \tag{3.24}$$

Then the second order nonlinear polarization is

$$\begin{aligned}\chi^{(2)}\boldsymbol{E}^2 = \chi^{(2)}\boldsymbol{E_1}^2[&\exp(-2i\omega_1 t) + \boldsymbol{E_2}^2\exp(-2i\omega_2 t) \\ &+ 2\boldsymbol{E_1}\boldsymbol{E_2}\exp(-i(\omega_1+\omega_2)t) + 2\boldsymbol{E_1}\boldsymbol{E_2}^*\exp(-i(\omega_1-\omega_2)t) + \text{c.c.}] \\ &+ 2\chi^{(2)}[\boldsymbol{E_1}\boldsymbol{E_1}^* + \boldsymbol{E_2}\boldsymbol{E_2}^*]\end{aligned} \tag{3.25}$$

The first line of (3.25) contains two oscillating terms at frequencies $2\omega_1$ and $2\omega_2$. It is responsible for s*econd-harmonic generation* (SHG), the effect that actually put nonlinear optics in the limelight when it was first measured in 1961 [14]. In the second line, we find components oscillating at the sum and at the difference of the original frequencies. They correspond to the so-called *sum-frequency* (SFG) and *difference-frequency generations* (DFG) [15]. The last two terms are constant and cause *optical rectification*, what amounts to the presence of a static electric field in the medium.

All of the processes mentioned so far are examples of what are known as *parametric* processes. The term is far from self-explanatory, but it is widely used to denote a process that leaves the quantum-mechanical state of the medium where it takes place unchanged. Some energy may be exchanged in the course of the interaction between photons and, say, electrons or phonons, allowing them to reside in a virtual level, but the duration of this stay is limited by the uncertainty principle relating energy and time. Conversely, processes that result in a net modification of the energy state of the medium are termed *nonparametric*. Brillouin scattering belongs to this category.

3.3.2 Coupled-wave equations

Stimulated Brillouin scattering (SBS) was first observed in 1964 by Chiao *et al.* in quartz and sapphire [7]. SBS, contrary to the spontaneous version of the phenomenon, is a nonlinear process that obeys the equation (3.23). Yet the nonlinear polarization that is responsible for the coupling of the two optical frequencies involved is not due to nonlinear susceptibility as in the parametric processes, but to the presence of a sound wave.

The most convenient way of tackling the description of SBS is to write down the equations of propagation for the three involved waves.

$$\nabla^2 \boldsymbol{E}_1 + \frac{\varepsilon^{(1)}}{c_0^2} \cdot \frac{\partial^2 \boldsymbol{E}_1}{\partial t^2} = \mu_0 \frac{\partial^2 \boldsymbol{P}_1^{NL}}{\partial t^2} \tag{3.26}$$

$$\nabla^2 \boldsymbol{E}_2 + \frac{\varepsilon^{(1)}}{c_0^2} \cdot \frac{\partial^2 \boldsymbol{E}_2}{\partial t^2} = \mu_0 \frac{\partial^2 \boldsymbol{P}_2^{NL}}{\partial t^2} \tag{3.27}$$

$$v^2 \nabla^2 \Delta\rho + \Gamma \nabla^2 \frac{\partial}{\partial t} \Delta\rho - \frac{\partial^2}{\partial t^2} \Delta\rho = \operatorname{div} \boldsymbol{f} \tag{3.28}$$

In (3.28), the density variation $\Delta\rho$ has been chosen to describe the acoustic wave, instead of the pressure variation as in (3.14). Γ is the acoustic damping coefficient, while the optical attenuation is considered negligible. For simplicity, we will only consider the case of backscattering and assume that the polarizations of the two lightwaves are parallel to the unitary vector $\mathbf{e}_1$. We choose to describe the Stokes scattering[1], where $\omega_1 = \omega_2 + \Omega$; consequently, the sound wave propagates in the same direction as $\boldsymbol{E}_1$, namely $+z$. $\boldsymbol{E}_1$ and $\boldsymbol{E}_2$ and $\Delta\rho$ can then be written as

$$\begin{aligned} \boldsymbol{E}_1(\boldsymbol{r}, t) &= \boldsymbol{e}_1 E_1(z, t) \exp[i(k_1 z - \omega_1 t)] + \text{c.c.} \\ \boldsymbol{E}_2(\boldsymbol{r}, t) &= \boldsymbol{e}_1 E_2(z, t) \exp[i(-k_2 z - \omega_2 t)] + \text{c.c.} \\ \Delta\rho(\boldsymbol{r}, t) &= A(z, t) \exp[i(qz - \Omega t)] + \text{c.c.} \end{aligned} \tag{3.29}$$

The rapidly oscillating parts of (3.29) describe the plane waves that would be solutions of (3.26) to (3.28) in the absence of the source terms. E_1, E_2 and A are the slowly-varying envelopes of the waves, caused by the coupling.

To proceed further, we have now to give explicitly the nonlinear polarizations and the driving force $\boldsymbol{f}$. They are closely related to the physical effect actually responsible for the coupling of light and sound in a medium, namely the electrostriction, on which we need to elaborate.

Electrostriction

Electrostriction is basically the tendency of materials to become compressed in presence of an electric field. When the density of a material increase by $\Delta\rho$, its dielectric constant changes too by an amount

1. The anti-Stokes case may be obtained by inverting the adequate signs.

$$\Delta\varepsilon = \frac{\partial\varepsilon}{\partial\rho}\Delta\rho . \tag{3.30}$$

As the potential energy per unit volume u depends on the dielectric constant as

$$u = \frac{\varepsilon \boldsymbol{E}^2}{8\pi}, \tag{3.31}$$

the increase in energy induced by the densification is

$$\Delta u = \frac{\boldsymbol{E}^2}{2}\Delta\varepsilon = \frac{\boldsymbol{E}^2}{2}\frac{\partial\varepsilon}{\partial\rho}\Delta\rho . \tag{3.32}$$

According to the first law of thermodynamics, this change must be equal to the work performed in compressing the material, given by

$$\Delta w = p_{st}\frac{\Delta V}{V} = -p_{st}\frac{\Delta\rho}{\rho}. \tag{3.33}$$

Here p_{st} denotes the contribution of the electric field to the pressure of the material. By equating (3.32) and (3.33), we find that

$$p_{st} = -\rho\frac{\partial\varepsilon}{\partial\rho}\frac{\boldsymbol{E}^2}{2} = -\gamma_e\frac{\boldsymbol{E}^2}{2}, \tag{3.34}$$

where we use the electrostrictive constant $\gamma_e = \rho\dfrac{\partial\varepsilon}{\partial\rho}$ already defined in (3.9). Due to the minus sign of the electrostrictive pressure p_{st}, the total pressure is reduced in regions of high electric field. The molecules of the material are drawn toward these regions. However, this move requires a time interval that is quite large compared to the typical oscillation time of optical waves. The material is therefore unable to follow the instantaneous field E, but is sensible to the time-averaged value $\langle \boldsymbol{E}^2 \rangle$ instead.

Slowly-varying amplitude approximation

We can now be more specific about the driving force $\boldsymbol{f}$ whose divergence appears in (3.28). It is an electrostrictive force that is given by the gradient of the electrostrictive pressure. So

$$\operatorname{div}\boldsymbol{f} = \operatorname{div}(\nabla p_{st}) = -\frac{\gamma_e}{2}\nabla^2\langle \boldsymbol{E}^2 \rangle . \tag{3.35}$$

In our case, the total electric field in the medium is the sum $\boldsymbol{E}_1 + \boldsymbol{E}_2$. Using the expressions (3.29) for this fields, (3.35) yields terms oscillating at differences

frequencies. We are only interested in the term of frequency[1] $\Omega = \omega_1 - \omega_2$, since it is the only one that has the same frequency as the left side of (3.28) :

$$\text{div}\, \boldsymbol{f} = \gamma_e q^2 [E_1 E_2^* \exp[i(qz - \Omega t)] + \text{c.c.}] \tag{3.36}$$

The nonlinear polarizations in (3.26) and (3.27) are, according to (3.5),

$$\boldsymbol{P}_j^{NL} = \Delta\varepsilon \boldsymbol{E}_j = \frac{\gamma_e}{\rho} \Delta\rho \boldsymbol{E}_j \tag{3.37}$$

where the second identity ensues from (3.30) and from the definition of γ_e. As in (3.36), we substitute the expressions (3.29) for the waves and we only keep in the product $\Delta\rho\, \boldsymbol{E}_j$ the terms whose frequency matches that of the left side of the corresponding inhomogeneous equation :

$$\frac{\partial^2 \boldsymbol{P}_1^{NL}}{\partial t^2} = \frac{\gamma_e \omega_1^2}{\rho} A E_2 \exp[i[k_1 z - \omega_1 t] + \text{c.c.}] \tag{3.38}$$

$$\frac{\partial^2 \boldsymbol{P}_2^{NL}}{\partial t^2} = \frac{\gamma_e \omega_2^2}{\rho} A^* E_1 \exp[i[-k_2 z - \omega_2 t] + \text{c.c.}] \tag{3.39}$$

Gathering the parts of the jigsaw[2], we could write three rather intricate coupled equations for Brillouin scattering, including second derivative in time and spatial coordinate. By chance, the slowly-varying-amplitude approximation is generally valid[3] in this context and the system of coupled equations becomes simpler :

---

1. The full development of $\boldsymbol{E}^2$ can be found in equation (3.25). The selected term corresponds to that responsible for difference-frequency generation through quadratic susceptibility.
2. By substituting (3.29), (3.36), (3.38) and (3.39) into (3.26) to (3.28).
3. The condition of validity is $\left|\frac{d^2 X}{dz^2}\right| \ll \left|k_X \frac{dX}{dz}\right|$, $X = A, E_1, E_2$. It amounts to requiring that the fractional change in any of the envelopes of the waves in a distance of an optical wavelength is much smaller than unity.

$$\begin{aligned}
\frac{\partial E_1}{\partial z} + \frac{n}{c_0}\frac{\partial E_1}{\partial t} &= \frac{i\omega\gamma_e}{2nc_0\rho}AE_2 \\
\frac{\partial E_2}{\partial z} - \frac{n}{c_0}\frac{\partial E_2}{\partial t} &= -\frac{i\omega\gamma_e}{2nc_0\rho}A^*E_1 \\
\frac{\partial A}{\partial z} + \frac{1}{v}\frac{\partial A}{\partial t} + \frac{\Gamma q^2}{v}A &= \frac{iq\gamma_e}{v^2}E_1E_2^*
\end{aligned} \tag{3.40}$$

A small additional simplification has been incidentally included by stating that the optical frequencies are very close to each other : $\omega_1 \approx \omega_2 = \omega$.

We will soon go on with the mathematics, but before diving into the possible ways of solving (3.40), let us have a look at figure 3-4, which gives an alternative, more graphical and so maybe more intuitive presentation of SBS. The interplay of $\boldsymbol{E}_1$, $\boldsymbol{E}_2$ and $\Delta\rho$ is depicted as a self-sustaining loop. The interference pattern of $\boldsymbol{E}_1$ and $\boldsymbol{E}_2$ is transformed by the electrostriction into a density variation of the medium, i.e. a sound wave. The diffraction of $\boldsymbol{E}_1$ on this sound wave reinforces $\boldsymbol{E}_2$, what in turn increases the interference, and so on.

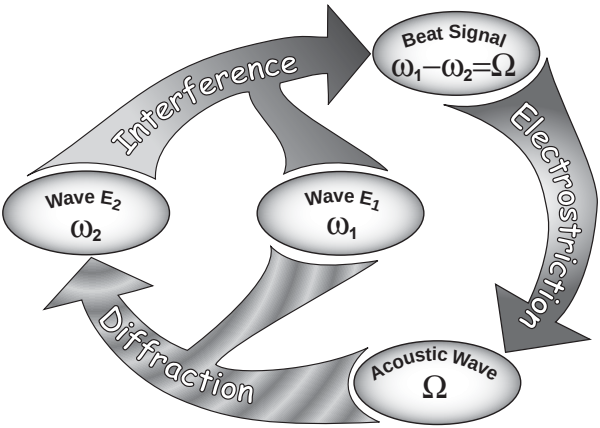

Figure 3-4. Graphical representation of the waves and of the processes involved in SBS. By courtesy of M. Facchini [4].

Steady-state solutions

The first step in solving (3.40) is made possible by the rapid attenuation of hypersonic acoustic waves : as the mean free path of the phonons is usually very small (~10^{-6} m) compared to the typical distance over which the source term varies significantly, it is customary to drop $\frac{\partial A}{\partial z}$ in the third equation of (3.40). The time derivative also vanishes if we assume steady-state conditions, what allows the determination of A in this case :

$$A = \frac{iq\gamma_e}{\Gamma_B \nu} E_1 E_2^* . \tag{3.41}$$

$\Gamma_B = \Gamma q^2$ denotes the Brillouin linewidth. The introduction of this value into the other equations of (3.40), always for steady-state conditions, gives

$$\begin{aligned} \frac{\partial E_1}{\partial z} &= -\frac{i\omega q\gamma_e^2}{2nc_0\rho\Gamma_B\nu}\left|E_2\right|^2 E_1 \\ \frac{\partial E_2}{\partial z} &= \frac{i\omega q\gamma_e^2}{2nc_0\rho\Gamma_B\nu}\left|E_1\right|^2 E_2 \end{aligned} \tag{3.42}$$

It is interesting to note that SBS turns out to be a third-order susceptibility process, as demonstrated by the third power of the electric fields appearing in (3.42). The system (3.42) can be transformed into a more tractable system of coupled differential equations for the easily measurable intensities of the fields $I_i = 2n\sqrt{\varepsilon_0/\mu_0}\left|E_i\right|^2$. The result is

$$\begin{aligned} \frac{dI_1}{dz} &= -g_0 I_1 I_2 \\ \frac{dI_2}{dz} &= -g_0 I_1 I_2 \end{aligned} , \tag{3.43}$$

where g_0 is the Brillouin gain coefficient. Different but equivalent expressions of g_0 are encountered in the literature :

$$g_0 = \frac{\gamma_e^2\omega^2}{nvc_0^3\rho\Gamma_B} = \frac{2\pi n^7 p_{12}^2}{c\lambda_1^2\rho v\Gamma_B} . \tag{3.44}$$

In this last expression, λ_1 is the wavelength of the wave E_1 and p_{12} is the longitudinal elasto-optic coefficient. In amorphous silica, the measured value of g_0 is $g_0 \sim 5 \times 10^{-11}$ m/W.

To understand the meaning of (3.43), let us assume that $I_1 >> I_2$, so that its variation can be neglected and $I_1(z) = I_1(0)$. This is the often occurring situation where a strong pump wave (this will be further denoted by the subscript *p* instead of 1) crosses a weak probe wave (denoted by *S*, for Stokes). The second differential equation in (3.43) can then be readily integrated and gives

$$I_S(z) = I_S(L)\exp[g_0 I_p(0)(L-z)]. \tag{3.45}$$

The Stokes wave launched at $z = L$ experiences an exponential growth as it propagates backwards through the medium.

Beyond the simplifications

To obtain the behavior described by (3.45), a number of simplifying assumptions have been made either explicitly or implicitly. We now state them clearly and discuss briefly the effect of their removal.

No linewidth

So far, we assumed that the identities $\boldsymbol{k}_S = \boldsymbol{k}_p - \boldsymbol{q}$ and $\omega_S = \omega_p - \Omega$ relating the wavevectors and the frequencies of the involved waves had to be strictly verified to allow SBS. These identities may be however relaxed and a small mismatch $\Delta k = \boldsymbol{k}_S - \boldsymbol{k}_p + \boldsymbol{q} \neq 0$, or equivalently $\Omega \neq \Omega_B = \omega_p - \omega_S$ is tolerable : SBS remains possible, but it is less efficient. This tolerance is ultimately due to the finite lifetime of the phonons. It manifests itself by the replacement of the gain factor g_0 in (3.43) by a gain curve depending on the frequency :

$$g(\Omega) = g_0 \frac{(\Gamma_B/2)^2}{(\Omega_B - \Omega)^2 + (\Gamma_B/2)^2} \tag{3.46}$$

The curve has a Lorentzian spectral profile centered on Ω_B, and its full width at half maximum (FWHM) is Γ_B. The tradition in the relevant literature is to express *g* as a function of $\nu = \Omega/2\pi$ rather than of Ω. To comply with it,

$$g(\nu) = g_0 \frac{(\Delta\nu/2)^2}{(\nu_B - \nu)^2 + (\Delta\nu/2)^2} \tag{3.47}$$

will be the form of the Brillouin gain curve we will use from now on.

Parallel polarizations

If the electric fields do not have the same polarization, the efficiency of SBS decreases : the scalar product of the polarization vectors $|\boldsymbol{e}_p \cdot \boldsymbol{e}_S|$ is no longer equal to unity and thus can not be dropped in the right hand side of the equation of the density wave. Consequently, (3.41) has to be replaced by

$$A = \frac{iq\gamma_e}{\Gamma_B \nu} |\boldsymbol{e}_p \cdot \boldsymbol{e}_S| E_1 E_2^* . \tag{3.48}$$

The generated acoustic wave has a smaller amplitude as before, leading to a smaller Brillouin gain. Usually, the dependence of g on the polarizations is expressed by an additional factor $\eta = |\boldsymbol{e}_p \cdot \boldsymbol{e}_S|^2$ in (3.47) :

$$g(\nu) = \eta g_0 \frac{(\Delta\nu/2)^2}{(\nu_B - \nu)^2 + (\Delta\nu/2)^2} \tag{3.49}$$

The effect of η is quite dramatic; for perpendicular polarizations, it leads even to the total suppression of SBS. The whole polarization issue has been thoroughly reviewed by van Deventer [16] and Niklès [17], to which we refer for further details.

Non-depleted pump

In view of the form of the spatial variation of I_S in (3.45), an exponential increase, it is evident, from obvious considerations of energy conservation, that the hypothesis of constant pump power can not hold very long and that the coupled equations (3.43) have to be solved exactly. Their general solution is [18] :

$$\begin{aligned} I_p(z) &= [D_0] \frac{I_p(0)\exp[gD_0 z]}{I_p(0)\exp[gD_0 z] - I_S(0)} \\ I_S(z) &= [D_0] \frac{I_S(0)}{I_p(0)\exp[gD_0 z] - I_S(0)} \end{aligned} \tag{3.50}$$

where $D_0 \equiv [I_p(0) - I_S(0)]$. The pump depletion is clearly evidenced in the pulsed case depicted in figure 3-5. As soon as SBS is under way (see the next section for details about the start of the process) and the Stokes wave has gained a significant power, energy is very efficiently transferred from the pump to the

Stokes. The medium behaves then like a mirror, reflecting the incident light - yet slightly shifting its frequency.

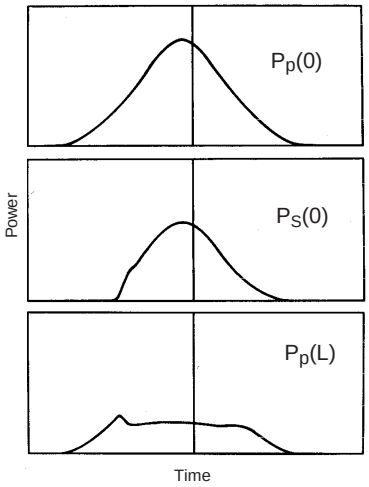

Figure 3-5. Oscilloscope traces of, from top to bottom : a pump pulse, the backscattered Brillouin pulse and what is left of the original pulse after SBS. The notation corresponds to the text. [12]

No optical attenuation

Even without Brillouin scattering, the lightwaves experience some attenuation in passing through a medium. This linear attenuation, mainly due to Rayleigh scattering, is described by a coefficient α (in units of m^{-1} or dB/m). In principle, α would depend on the frequency, but here it will be considered equal for the pump and the Stokes waves. Taking this attenuation into account brings the following modifications of the coupled intensity equations (3.43) :

$$\begin{aligned} \frac{dI_p}{dz} &= -g_0 I_p I_S - \alpha I_p \\ \frac{dI_S}{dz} &= -g_0 I_p I_S + \alpha I_S \end{aligned} \qquad (3.51)$$

Unfortunately, there is no exact analytical solution of this system [18]. Nevertheless, numerical implementations of (3.51) agree very satisfactorily with the experiments.

Steady-state conditions

In order to calculate the amplitude *A* of the density wave (3.41), we assumed that the lifetime of the acoustic wave was negligible compared to that of the light-

waves. This condition is obviously fulfilled for DC electromagnetic waves, and it holds also for pulses of long enough duration T_p. But if $T_p < T_a$, T_a being the typical phonon lifetime (approximately 10 ns), the Brillouin gain becomes time-dependent and it is necessary to include the dynamics of the acoustic wave. Due to the fact that we were experimentally interested only in the DC or quasi-DC regime, we give up describing the transient Brillouin effects in this place.

SBS start

The equations (3.50) provide admittedly a valid solution for the problem of the spatial variation of the pump and the Stokes waves. However they have something of the proverbial tail-biting snake by requiring the value of the backscattered wave at the position 0, i.e. at the end of its propagation. On the other hand, they do not give any clue about what occurs at the other extremity, say at L, of the scattering medium, the mathematical asymptote $\lim_{z \to \infty} I_S(z) = 0$ having no physical meaning.

Brillouin amplifier

The first way to deal with this difficulty is to launch purposely a (usually) small lightwave at the distant end of the medium. If its frequency and that of the pump wave are well tuned and satisfy the conditions of Brillouin scattering in that medium, the backscattering wave (also known as signal wave) undergoes an amplification. Obviously, the pump depletion sets an upper limit to the amplitude of the signal that can be amplified. Beyond that limit, the gain becomes saturated.

Brillouin generator

Without externally applied signal wave, SBS can still occur. In this case, the seed that triggers the build-up of the Stokes wave is provided by the spontaneous Brillouin scattering on the thermal phonons [19]. In normal cases, there is no shortage of phonons[1]; for instance, the Bose-Einstein statistic gives $k_B T/\hbar\omega \approx 600$ phonons at 10 GHz and ambient temperature. So the seeds of a possible Stokes wave are always readily available, and that is mainly[2] a question of intensity of the pump wave whether it will grow or not.

1. The case of extremely low temperatures may be different.

2. The linear optical attenuation and the mere size of the medium sample also come into play.

3.4 Stimulated Brillouin scattering in optical fibers

For a start, let us emphasize the fact that in the frame of this work we are only interested in single-mode fibers (SMFs). Two properties of multi-mode fibers are detrimental for non-linear effects : on the one hand, it is impossible to disentangle the contributions of each propagated mode to the non-linear effects; on the other hand, the sectional area of multimode fibers is much larger than that of SMFs, so that the light power remains spread enough not to reach the threshold where the nonlinearities become important. Therefore the words 'optical fibers' will always implicitly include the attribute 'single-mode' in this document.

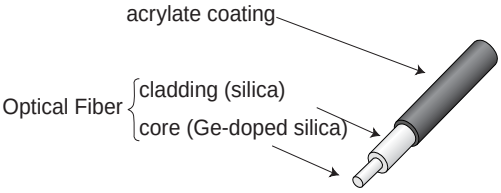

Figure 3-6. The three layers of an optical fiber

In its simplest form (step-index fiber, see above), an optical fiber consists of a central core of Germanium-doped silica surrounded by a cladding layer of pure silica whose refractive index is slightly lower than that of core. The table gives typical values of some of the basic properties of such fibers. More sophisticated index profiles (depressed-cladding, W-profile, graded-index,...) are also common, primarily aimed at tailoring the chromatic dispersion.

Core diameter	5-10 µm
Cladding diameter	125 µm
Refractive index difference between core and cladding	$(n_1 - n_2)/n_1 \sim 3\times10^{-3}$
Coating material	acrylate
Attenuation @1550 nm	0.17 dB/km
Maximal effective length for nonlinear effects @1550 nm	~25 km
Effective mode area	30-80 μm^2
Chromatic dispersion @1550 nm	17 ps/nm·km

Table 3.2. Typical values of some characteristics of a standard fiber for telecommunications (step-index). See also table 2.3 for additional physical parameters.

The most striking feature of single-mode fibers, actually their raison d'être, is their ability to guide lightwaves with extremely low losses over considerable distances. Historically, the path that led from the long-known principle of total reflection to the present highly effective waveguides entailed considerable technical difficulties, vividly reported by Hecht [20]. Now the field is technologically fully mature and fabrication processes like MOCVD (see section 2.3.3) allow the suppliers to precisely tune the characteristics of fibers for any given application.

How does the obvious difference in geometry between fibers and bulk silica modify the behavior of light ? The theory of linear wave propagation in fibers is well-known [21, 22] and we will only mention polarization or dispersion issues when they are relevant for the study of Brillouin scattering. Suffice it to remind that the intensity distribution of the fundamental HE_{11} mode is very close to a Gaussian curve, and that its wavefront can be approximated to a good accuracy by planes perpendicular to the axis of the fiber.

As far as nonlinear effects are concerned, SMFs can basically be considered as bulk samples. Typical dimensions of the core are admittedly small, especially when splicing fibers, but even a 5 μm diameter is large compared to interatomic distances (0.16 nm for the Si-O link). Hence measurements on fibers should give results that are also valid for the bulk case. Nevertheless occasional deviations from this parallelism can not be ruled out.

3.4.1 Relevant characteristics of optical fibers

- *Geometry*

Spontaneous Brillouin scattering radiates light in every direction in an homogeneous medium; the frequency shift experienced by the light in the process depends on the scattering angle as $\sin(\theta/2)$, making the forward-scattered light indistinguishable from the incident one. As for stimulated Brillouin scattering, it requires the superposition of a pump and a Stokes waves; in optical fibers, this is realized simply by making them contrapropagative guided waves. The diagram of the wavevectors is then that of figure 3-7, a particular case of figure 3-2.

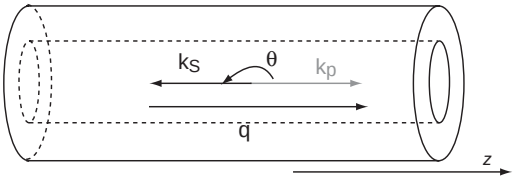

Figure 3-7. Geometry of Brillouin backscattering in fibers

Since $\theta = 180°$, the Brillouin frequency shift is maximal and given by

$$\nu_B = \frac{2n\nu_A}{\lambda_p}, \tag{3.52}$$

where λ_p is the wavelength of the pump, and the letter *A* has been added to remove the possible ambiguity of the notation *v* for the acoustic velocity.

• *Attenuation*

State-of-the art fibers reach levels of attenuation that are very close to the physical limits for solids. Different absorption and scattering mechanisms define transparency windows in the spectral domain (see figure 3-8). The real absorption minimum lies around 1550 nm, the so-called third window. In relation with this figure, note that the amplitude of the absorption peaks due to the presence of residual OH ions may be reduced; these peaks are even suppressed (AllWave™ fibers) by some recent fabrication processes.

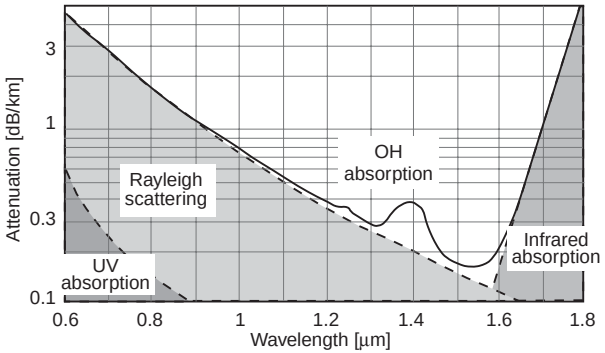

Figure 3-8. Total attenuation α_{dB} (full line) of a typical single-mode optical fiber, as well as its physical causes (grey regions and dashed lines).

As evidenced by the coupled equations (3.51), the linear attenuation[1] α modifies the intensities $I_p(z)$ and $I_S(z)$ through the appearance of an additional exponential decrease : $I_p(z) = I_p(0)\exp[-\alpha z]$. An elegant artefact that is often used to take the attenuation into account is the effective length defined by

$$L_{eff} = \frac{1-\exp(-\alpha L)}{\alpha}, \tag{3.53}$$

that tends to $1/\alpha$ for very long fibers. As a simple example of use, consider the situation where, as in (3.45), we neglect the pump depletion (due to SBS) but not the pump nor the Stokes attenuations (due to Rayleigh scattering); the intensity of the Stokes wave backscattered by a fiber of length L can be written as

$$I_S(0) = I_S(L)\exp[g_0 I_p(0) L_{eff}]\exp[-\alpha L]. \tag{3.54}$$

The Brillouin threshold, that is the critical pump power for which the Stokes backscattered power becomes equal to the pump power, may also be expressed using the effective length [23 p.32]:

$$P_{th} = \frac{I_{th}}{A_{eff}} \approx \frac{19 A_{eff}}{g_0 L_{eff}}. \tag{3.55}$$

For typical values of $g_0 \approx 5\times10^{-11}$ m/W, $L_{eff} \approx 25$ km and $A_{eff} \approx 50$ µm^2, this gives $P_{th} \sim 1$ mW. The significance of this figure for optical telecommunications will be discussed in section 3.4.3.

• *Birefringence*

A SMF, as its name does not precisely imply, carries *two* eigenmodes with linear orthogonal polarizations. In an ideal fiber, these modes are fully degenerate, in the sense that they have exactly the same propagation constant, and uncoupled. But the slightest deviation from the ideal geometry, unavoidable in any real case, creates some birefringence, that results in a difference in the constants of propagation[2] of the modes. This causes a variation of the state of polarization during the propagation. Fibers where this variation is slow are named low-birefringence

1. The conversion between α [m^{-1}] and α_{dB} [dB/km] is $\alpha_{dB} = 4.343\text{x}10^{-3}\,\alpha$.

2. The birefringence is defined as $B = |n_x - n_y|$, where n_x and n_y are the refractive indices actually viewed by the orthogonal modes.

fibers; they include standard telecom fibers. Conversely, there are some cases where a great amount of birefringence is introduced purposely, by giving an elliptical shape to the core for example; the large discrepancy in the constants of propagation effectively prevents the coupling between the modes, making the fiber polarization-maintaining.

Let us take a section of a high-birefringence, polarization-maintaining fiber, and launch a pump lightwave in an eigenmode. If the contrapropagating Stokes wave has the same polarization, the polarization efficiency parameter η appearing in (3.49) is equal to 1 and Brillouin gain is maximal, since the waves polarizations are perfectly aligned over the whole length of the fiber. In the opposite case of perpendicular polarizations, there will be no SBS at all.

For low-birefringence fibers, the polarization variation is usually modelled as a 3D random process. It can be shown that the resulting efficiency has a value that lies anywhere between 1/3 and 2/3, depending on the relative input polarizations of the two waves. An example of this behavior is shown in figure 3-9. In general, the polarization-related problems turn out to impose a two-stages measurement procedure of the Brillouin gain curves : first adjust the polarizations in order to get the maximal gain and carry out the measurement, and then search the state of polarization yielding minimal contrast and measure again [3, 24].

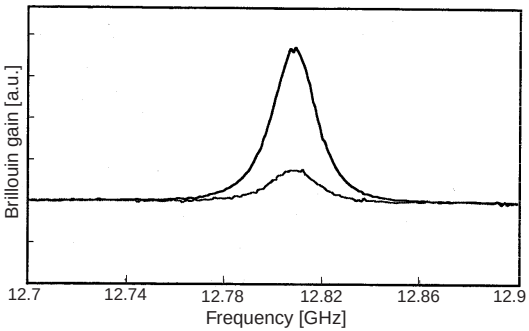

Figure 3-9. Minimal and maximal contrasts in a BGC measurement on a low-birefringence fiber. The polarization efficiency h is respectively equal to 1/3 and 2/3. From [3].

• *Sound propagation*

It should be kept in mind that SMF have finite numerical apertures. It means that a wave with a non-null, albeit very small, angle from the axis direction may be guided, if it falls in the acceptance cone of the fiber. Besides, optical SMF behave as highly multimode acoustic waveguides. The theory of sound wave propagation has many common points with that of lightwave propagation. The difference in refractive index is replaced by a change in the elastic constants and the density at the boundary core-cladding. However, acoustic modes show more diversity in the geometry and the typical dimensions of SMFs. One can find longitudinal, torsional or radial modes of vibration, or any mix of these. But stimulated Brillouin scattering effectively results in the selection and subsequent amplification of one acoustic mode, the fundamental longitudinal one. In usual conditions, all the other modes can be discarded from the description, as we did so far.

This is no longer possible in the case of Brillouin fiber lasers. If the fiber acts as the resonant cavity of a laser, even an effect that was negligible in a single-pass configuration may lead to dynamically instabilities. In this context, the process shown in figure 3-10 has to be taken into account [25]: the scattering on a transverse (i.e. radial) sound wave gives a forward-propagating Stokes wave. If the scattering angle is smaller than the numerical aperture of the fiber, this last wave is guided. Note that a backscattering of the same kind is also possible.

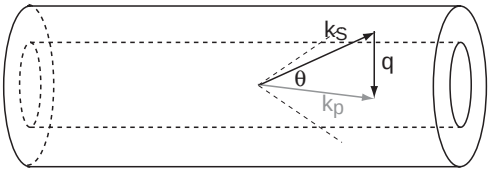

Figure 3-10. Geometry for transverse Brillouin scattering.

Another example of anomalous behavior related to sound waves is reported in figure 3-11. This is a measurement of the BGS of the ‘usual’ backscattered Stokes wave at 4 K and, for comparison, at 13 K. The chosen fiber has a pure silica core and a so-called depressed cladding, where the necessary decrease in the refractive index is obtained by adding fluorine dopant. The curve at 13 K shows the expected Lorentzian shape of the spectrum. At 4 K, the linewidth of the peak

is much smaller (that is a common behavior, see chapter 4) and, more surprisingly, there are smaller peaks corresponding probably to other modes of vibration. It is not clear how a decrease in temperature can cause this behavior, and why specifically in that type of fibers. Recent measurements [26] show that spon-

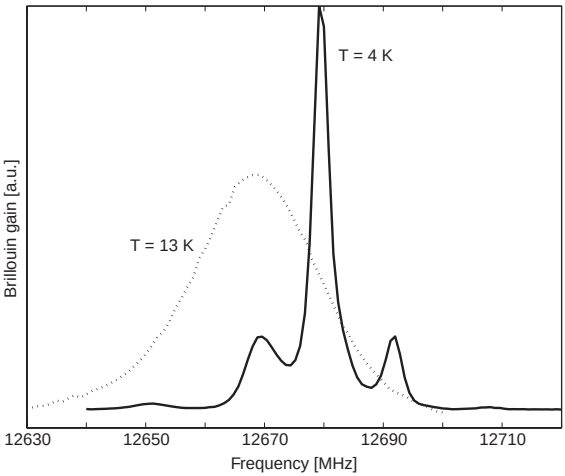

Figure 3-11. Brillouin gain spectra of a F-doped fiber at two different cryogenic temperatures.

taneous Brillouin spectra in fibers do indeed exhibit multiple peaks, each one corresponding to an acoustic mode, but that all but the main one usually vanish once the stimulated regime is reached. Clearly, this is no longer the case here. We will further discuss this peculiar behavior in section 4.3.4.

3.4.2 Influence of extrinsic parameters on Brillouin gain spectra

Many parameters are able to modify the properties of the Brillouin gain curves. The first one, as often in physics, is the temperature, but we postpone the study of the dependence on temperature of SBS until chapter 4, that will be entirely devoted to it. We here only briefly review the main results about the dependence on concentration of dopant, strain and pressure, more extensively addressed elsewhere [3, 24, 27].

- *Dopant concentration*

The measurements of the Brillouin frequency shift of several fiber samples with varying concentration of germanium oxide in the core are reported in

figure 3-12. The experimental points show an excellent correlation with the linear regression. The slope of the regression line, for a pump wavelength of 1550 nm, is -80 MHz/mol% GeO_2. The negative sign of the slope is not a surprise, as sound velocity in pure GeO_2 (~3780 m/s) is markedly lower than that in silica [28]. One can take advantage of this dependence on the chemical composition to identify the different fibers in a telecom network or to check the homogeneity of their composition [29]. The linewidth of the Brillouin gain is also found to vary linearly with the GeO_2 concentration, the constant of proportionality being close to 1 MHz/mol% GeO_2.

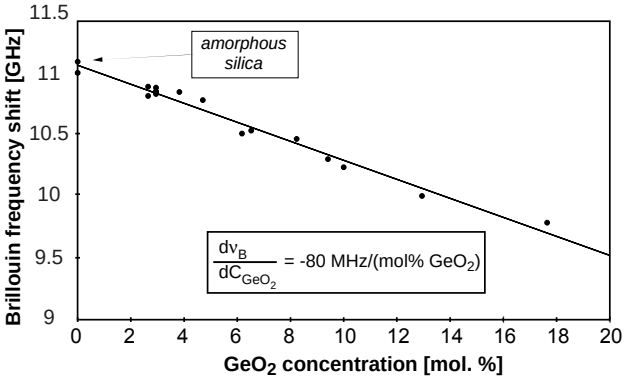

Figure 3-12. Brillouin frequency shift @ 1550 nm as a function of GeO_2 concentration in core. Data collected by Niklès [3].

- *Strain*

A longitudinal strain applied to a fiber elongates it and changes its density. Since the sound velocity depends directly on the material density, this implies a change in the sound velocity and eventually in the Brillouin frequency shift. When the frequency shift is plotted as a function of elongation (figure 3-13), the resulting curve is again a line practically up to the breaking limit of the fiber (~1% elongation). For the depicted fiber, the slope of the variation is measured to be, 505 MHz/%. In general, this slope depends on the fiber composition and on the coating material : some coatings take a part of the mechanical stress, while other let all the burden to the silica. As for the linewidth, it does not seem to be strain-dependent.

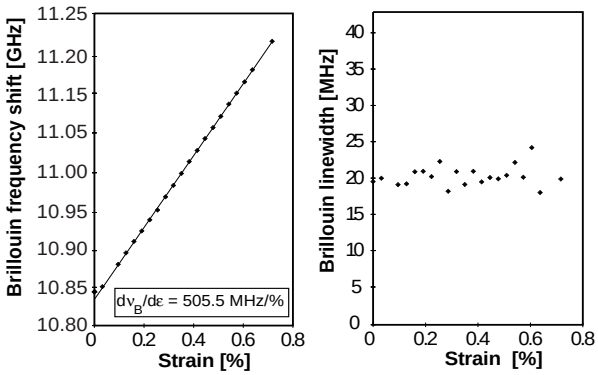

Figure 3-13. Brillouin frequency shift and Brillouin linewidth @ 1550 nm as a function of applied strain on a standard fiber. Data collected by Niklès [3].

- *Pressure*

When submitted to high pressures, an optical fiber exhibits a reduction of its Brillouin frequency shift, as evidenced by figure 3-14.

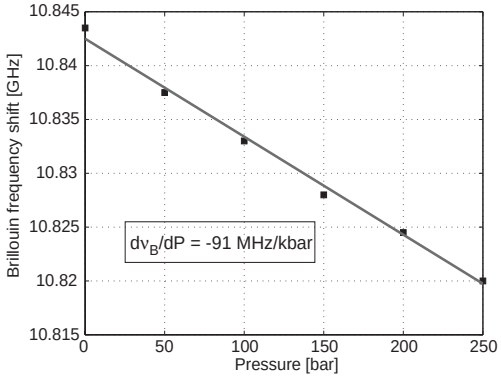

Figure 3-14. Brillouin frequency shift as a function of hydrostatic pressure. Measurements by Le Floch [27].

This is the opposite of the previous case, which can be simply explained by stating that the hydrostatic pressure compress the material and thus increases its density. Another hint toward an unified explanation for these two types of externally applied deformations is the fact that the Brillouin linewidth is constant in both cases. To compare the two slopes, one should convert the measurements to a fre-

quency shift variation as a function of the material density. The linear variation region is expected to extend over a considerable pressure range [28], at least up to ~1 GPa (10'000 bar), where atomic rearrangements related to the crystalline phase transition quartz-coesite take place.

3.4.3 Significance of SBS

- *SBS as a drawback*

Stimulated Brillouin scattering is a major concern in the design and installation of optical telecommunication networks. It has the lowest threshold among all the nonlinear effects (at best a few mW for a continuous wave); once the threshold is reached, a significant part of the power is converted to contrapropagating Stokes radiation, what is detrimental from two standpoints. First the information-carrying signal at the end of the link has less power, as a result of pump depletion. Second, the backward-propagating wave provides an unwanted feedback to the emitter laser that can destabilize it.

Telecom engineers deal with this issue by artificially increasing the Brillouin threshold. The basic scheme to do that is to widen the spectral width of the light, either by a dedicated direct modulation of the laser or by a proper choice of the bitrate and the format of the information-carrying pulses. Input powers of up to 100 mW can then be used without suffering from degradation of the system performance.

- *SBS as an advantage*

When amplification of a lightwave is required, SBS seems at first sight a suitable candidate with its low threshold and high efficiency. Some attempts have been made in this direction indeed. But its narrow linewidth turns out to limit considerably the performance of the proposed schemes, specially when compared to stimulated Raman scattering.

Placing the fiber in a cavity, one can realize fiber-Brillouin lasers. A possible geometry is a ring cavity, namely a closed loop of fiber where the pump lightwave is introduced and the Stokes wave is extracted by a unbalanced coupler [23]. The optical output may be a very coherent DC wave, whose spectral width

is in the kHz range, or short pulses. Practically, ring-cavity Brillouin lasers can act as sensitive gyroscopes.

Another application where SBS is put to positive use is the domain of distributed fiber sensors that constitutes the core subject of the chapter 5 of this document. Yet before addressing this subject, we still have to carefully study the influence on Brillouin scattering of the single most important parameter we have tossed aside so far, namely the temperature.

References

[1] *G.P. Agrawal*
Nonlinear fiber optics
2nd ed. Academic Press, San Diego (1995).

[2] *R.W. Boyd*
Nonlinear optics
Academic Press, San Diego (1992).

[3] *M. Niklès*
La diffusion Brillouin dans les fibres optiques : étude et application aux capteurs distribués
Ph.D. Thesis EPFL, Lausanne (1997).

[4] *M. Facchini*
Distributed optical fiber sensors based on Brillouin scattering
Ph.D. Thesis EPFL, Lausanne (2001).

[5] *L. Brillouin*
Diffusion de la lumière et des rayons X par un corps transparent homogène : influence de l'agitation thermique
Annales de Physique, **17**, p. 88-122 (1922).

[6] *P. Debye, F.W. Sears*
On the scattering of light by supersonic waves
Proc. Nat. Acad. Sc., **18**, p. 409-414 (1932).

[7] *R.Y. Chiao, C.H. Townes, B.P. Stoicheff*
Stimulated Brillouin scattering and coherent generation of intense hypersonic waves
Phys. Rev. Lett., **12**(21), p. 592-595 (1964).

[8] *E.P. Ippen, R.H. Stolen*
Stimulated Brillouin scattering in optical fibers
Appl. Phys. Lett, **21**, p. 11 (1972).

[9] *D. Park*
The fire within the eye
Princeton University Press, Princeton (1997).

[10] *M. Born, E. Wolf*
Principles of optics
7th ed. Cambridge University Press, Cambridge (1999).

[11] *R. Loudon*
The quantum theory of light
2nd ed. Oxford University Press, Oxford (1983).

[12] *Y.R. Shen*
The principles of nonlinear optics
Wiley, New York (1984).

[13] *I.L. Fabelinskii*
Molecular scattering of light
Plenum Press, New York (1968).

[14] *P.A. Franken, A.E. Hill, C.W. Peters, G. Weinreich*
Generation of optical harmonics
Phys. Rev. Lett., **7**(4), p. 118-119 (1961).

[15] *M. Bass, P.A. Franken, A.E. Hill, C.W. Peters, G. Weinreich*
Optical mixing
Phys. Rev. Lett., **8**(1), p. 18 (1962).

[16] *M.O. van Deventer, A.J. Boot*
Polarization properties of stimulated Brillouin scattering in single-mode fibers
J. Lightwave Technol., **12**, p. 585-590 (1994).

[17] *M. Niklès, L. Thévenaz, P.A. Robert*
Simple distributed fiber sensor based on Brillouin gain spectrum analysis
Opt. Lett., **21**(10), p. 758-760 (1996).

[18] *L. Chen, X. Bao*
Analytical and numerical solutions for steady state stimulated Brillouin scattering in a single-mode fiber
Opt. Commun., **152**, p. 65-70 (1998).

[19] *R.W. Boyd, K. Rzazewski, P. Narum*
Noise initiation of stimulated Brillouin scattering
Phys. Rev. A, **42**(9), p. 5514-5521 (1990).

[20] *J. Hecht*
City of light : the story of fiber optics
Oxford University Press, New York (1999).

[21] *B.E.A. Saleh, M.C. Teich*
Fundamentals of photonics
Wiley, New York (1991).

[22] *A.W. Snyder, J.D. Love*
Optical waveguide theory
Chapman and Hall, London (1983).

[23] *A. Küng*
L'émission laser par diffusion Brillouin stimulée dans les fibres optiques
Ph.D. Thesis EPFL, Lausanne (1997).

[24] *M. Niklès, L. Thévenaz, P.A. Robert*
Brillouin gain spectrum characterization in single-mode optical fibers
J. Lightwave Technol., **15**(10), p. 1842-1851 (1997).

[25] *I. Bongrand, E. Picholle, C. Montes*
Coupled longitudinal and transverse stimulated Brillouin scattering in single-mode optical fibers
Eur. Phys. J. D, **20**, p. 121-127 (2002).

[26] *A. Yeniay, J.-M. Delavaux, J. Toulouse*
Spontaneous and stimulated Brillouin scattering gain spectra in optical fibers
12(8), p. 1425-1432 (2002).

[27] *S. Le Floch*
Etude de la diffusion Brillouin stimulée dans les fibres optiques monomodes standard. Application aux capteurs de température et de pression
Ph.D. Thesis Université de Bretagne occidentale, Brest (2001).

[28] *J. Hertling, S. Baessler, S. Rau, G. Kasper, S. Hunklinger*
Internal friction and hypersonic velocity in vitreous germania under high pressure
J. Non-Crystal. Solids, **226**(1-2), p. 129-137 (1998).

[29] *L. Thévenaz, M. Niklès, A. Fellay, M. Facchini, P.A. Robert*
Applications of distributed Brillouin fibre sensing
Proc. of the SPIE International Conference on Applied Optical Metrology, Balatonfüred, Hungary, p. 374-381 (1998).

CHAPTER 4

Brillouin gain spectrum dependence on temperature

4.1 Introduction

The linear increase of the Brillouin shift with increasing temperature is probably the most hackneyed piece of information about Brillouin scattering in silica fibers. It was noticed very early, verified many times and has motivated to a large extent the development of the temperature sensors we will discuss in the chapter 5. Yet this is not the full picture, as the linearity does not extend up to the physical limits of the optical fibers. The purpose of this chapter is to look closely to the temperature ranges where the linear behavior is no longer observed, above and below the ambient temperature. Special attention will also be given to the linewidth of the Brillouin spectrum.

We begin with the description of the experimental setup we will use to measure these BGSs, followed by a few words about the fiber samples and the various facilities (ovens and cryogenic installations) at our disposal. Then come the experimental results, presented in three parts : the linear region, at and around the ambient temperature, the high-temperature region, and the cryogenic range. Among the three domains, the third one is by far the most interesting from a physical point of view, exhibiting features such as a maximum in the linewidth and a minimum in the Brillouin shift. These peculiarities are directly related to the disordered structure of the glass that was the subject of the chapter 2. In the last section we will thus make some links between our measurements in fibers, measurements carried out on bulk silica samples, and the theoretical models based on tunneling systems.

4.2 Experimental setup

The task of designing an experiment to measure the Brillouin gain spectrum of an optical fiber may seem at first glance relatively easy, in view of the characteristic features of both the phenomenon and the medium, as described in the previous chapter. The obvious first possibility is to measure the spectrum of the light that is backscattered when a lightwave propagates within a fiber. This rather 'brute force' approach yielded the first published results [1]. The main drawback of the method is the presence of the elastic Rayleigh scattering, much more efficient than spontaneous Brillouin scattering[1].

4.2.1 Principle

To enhance the intensity of Brillouin-scattered light, it is decidedly preferable to work in a Brillouin amplifier configuration rather than in the aforementioned generator configuration. This involves the use of a second lightwave as a seed of the scattered wave. The basic setup, sketched in figure 4-1, mainly consists in two light sources at the two ends of the fiber, a coupler to extract the useful signal and a photo-detector to convert the light intensity into an electric signal. The frequency difference between the crossing lightwaves must be tunable around the value of the Brillouin shift of the fiber. The BGS is then obtained by simply measuring the amplification of the probe wave as a function of the frequency difference.

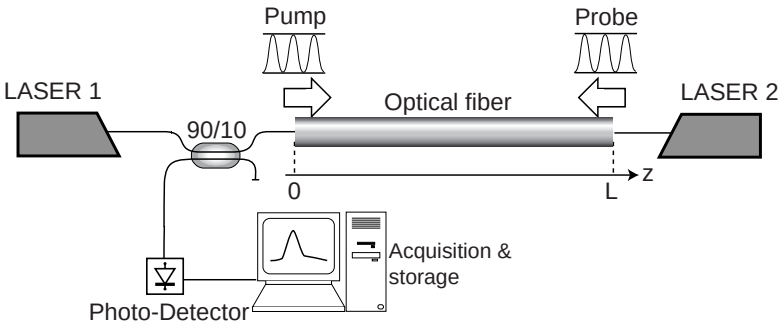

Figure 4-1. Basic principle of a BGS determination experiment.

1. The ratio I_{Ray}/I_B of the intensities scattered by respectively Rayleigh and Brillouin scatterings, sometimes called Landau-Placzek ratio, is equal to ~1000 in the spontaneous case.

The first reported measurements [2] based upon such a setup were published in 1987. The main practical requirement for the measuring process is a stable frequency difference between the two light sources. This can be hardly fulfilled with two independent lasers, as their wavelengths do vary slightly - yet significantly enough as far as Brillouin scattering is concerned - with scarcely controllable environmental parameters such as the temperature or the electrical current. Without long-term stability of the frequency difference, the acquisition of a BGS is tedious and the results strongly lack reliability.

4.2.2 Detailed setup

To overcome these limitations, Niklès *et al*. proposed [3] to generate both the pump and the probe waves from a single physical light source by using an electro-optical modulator (EOM). EOMs are essential parts of the optical telecommunication networks, since they are able to modulate the amplitude[1] of a monochromatic carrier wave in order to encode information. Basically, these devices consist in Mach-Zehnder interferometers realized in $LiNbO_3$ waveguides. Electrodes are fixed on one arm[2] of the interferometer; when a voltage is applied to them, the refractive index of the crystal is changed through Pockels effect [4, ch. 18]. Consequently, the phase of the propagating lightwave is modified in one arm, while staying unchanged in the other. This phase variation is converted into an amplitude variation when the two optical paths merge. Globally, the transmitted intensity varies sinusoidally as a function of the applied voltage (see also figure 5.3).

Two possible optical spectra after modulation by an EOM are represented in figure 4-2. In *a*, a radio-frequency (RF) signal of frequency $f_m \sim 12$ GHz is applied. It results in the generation of two new optical frequencies, symmetrically disposed on either side of the carrier. Now the carrier component may be totally suppressed[3], if a DC voltage bias is also applied, with a value precisely

1. Phase modulators also exist and are even simpler than amplitude modulators, as there is no need for an interferometric configuration in this case.
2. Actually, a configuration with inversely polarized electrodes on the two arms is more efficient and thus preferred. This technical point has no significance here.
3. At least in principles. Real EOM have ~30 dBm extinction ratios. That is not bad, but not infinite either.

chosen so that the interfering lightwaves have a 180° phase difference. The resulting spectrum is shown in *b*, and it will be used for measuring BGS.

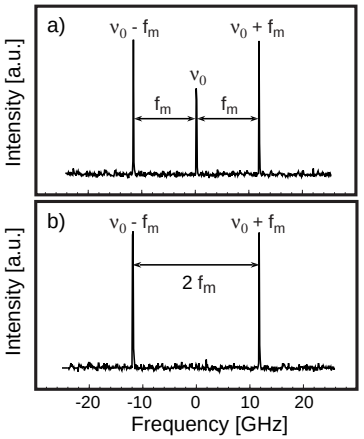

Figure 4-2. Optical spectra of a monochromatic lightwave modulated by an EOM. The modulation frequency is f_m. a) no particular DC bias applied; b) DC voltage tuned to suppress the carrier; the modulated spectrum consists in two sidebands.

As mentioned, Niklès and his followers in our group start with a single laser. The light is immediately separated in two parts by a unbalanced coupler. The larger part is used as the pump, while the other, after modulation, is launched backwards into the fiber to act as the probe wave. The small frequency variations of the laser can no longer have any impact on BGS measurements, because both pump and probe originate from the same source, and drift parallel therefore. Laser, EOM and coupler are sketched in figure 4-3, together with the additional ancillary devices we have to discuss now.

Polarization controller (PC). The influence of the polarization on the efficiency of Brillouin scattering has been highlighted in section 3.4. In order to maximize (or, if needed, to minimize) the gain, we have to be able to modify the polarization, what we do with Lefèvre's loops.
Optical isolator (ISO). It prevents the pump wave to hit the detector and to hinder the measurement of the amplified signal wave.
RF generator. The commercial instrument used (HP 8673H) supplies a high-quality microwave signal that is stable, reproducible and spectrally narrow. The quality of the measurements can be directly related to the quality of this RF signal.

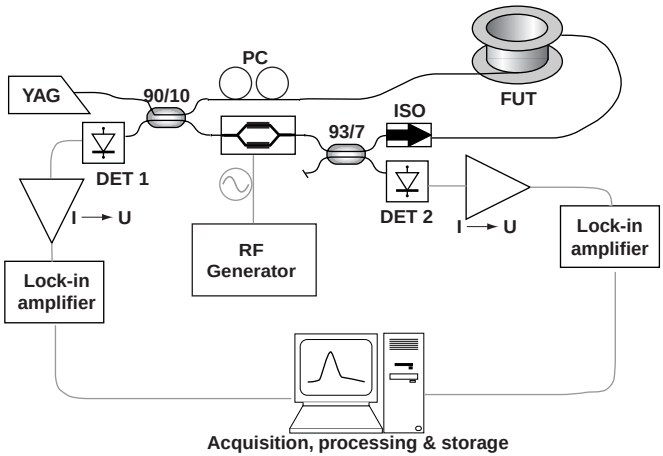

Figure 4-3. Detailed setup for the measurement of Brillouin gain spectra in fibers. ISO = optical isolator, PC = polarization controller, FUT = fiber under test, DET = detector.

Modulator DC bias setting (not represented). Unfortunately, the DC voltage that must be applied to the EOM in order to suppress the unmodulated carrier component from the spectrum of the signal wave (see figure 4-2 b) is temperature-dependent. To correct the induced drift, a feedback loop including a PID regulator has to be added.

Second coupler and second detector. The intensity of the amplified signal on detector 1 is proportional to the intensity of the input signal wave (see equation 3.54). As the latter turns out to be dependent on the RF frequency, it is necessary to measure it on detector 2 by extracting a few percents of the signal after the EOM with a second coupler. The Brillouin gain is then proportional to the ratio of the two measured intensities.

Lock-in detection. With the available pump power, the signal-to-noise ratio of the DC measured gain curves is found to be insufficient. Lock-in amplification has thus to be used.

Laser. The chosen light source is a Nd:YAG laser at 1319 nm. The effective pump power launched (after the modulator and the coupler) into the fiber is 35 mW. Its main advantage is its very narrow linewidth (~10 kHz) : the artificial broadening of the BGS schematized in figure 4-4 and resulting from the linewidth of the pump laser is practically negligible here.

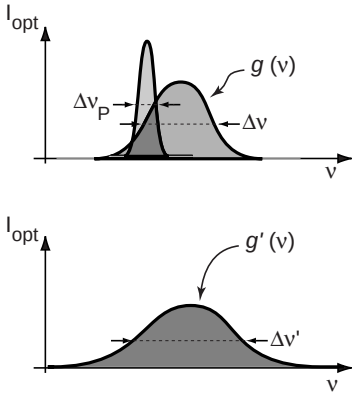

Figure 4-4. Apparent broadening of the BGS due to the linewidth of the pump laser. The measured BGS is the convolution of the intrinsic BGS and the spectrum of the pump. For explicit calculations, see [5, 6]

4.2.3 Pump-probe interaction

The power of the probe wave depends on the amplitude of the microwave signal. In any case, it remains low (~0.01 mW) when compared to the pump; moreover, it is always possible to choose a probe power small enough so that the pump depletion due to Brillouin scattering may be safely neglected[1] and $I_p(z) = I_p$. For a fiber of length L, the intensities of the upper and lower sidebands of the probe wave at the input end of the fiber $z = 0$ are then respectively given by

$$\begin{aligned} I_0^u &= I_L^u \exp[-g_B I_p L_{eff} - \alpha L] \\ I_0^d &= I_L^d \exp[g_B I_p L_{eff} - \alpha L] \end{aligned} \quad . \tag{4.1}$$

The lower sideband undergoes exponential amplification, and the upper one exponential depletion in the course of their interaction with the probe wave. In terms of energy transfers, we get the figure 4-5. The assumption of undepleted pump is all the more valid since the energy transferred from the upper sideband partially compensates for the energy lost in favor of the lower sideband.

1. The effect of linear attenuation upon the pump is taken into account, though, through the use of L_{eff} instead of L in (4.1).

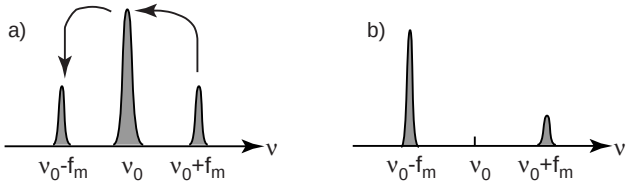

Figure 4-5. Schematic representation of the energy transfers between the pump wave and the two components of the probe wave, a) during the interaction, b) probe wave after the interaction.

Stating that the two sidebands have initially the same intensity $I_L^u = I_L^d = I_S$, the measured intensity at $z = 0$ is simply

$$I_{meas} = I_0^d + I_0^u = 2\exp[-\alpha L] I_S \cosh[g_B I_p L_{eff}], \tag{4.2}$$

and the BGS may be retrieved as

$$g_B(\nu) = \frac{\operatorname{acosh}\left[\dfrac{I_{meas}(\nu)}{2\exp[-\alpha L] I_S(\nu)}\right]}{I_p L_{eff}}. \tag{4.3}$$

4.2.4 Available facilities and fiber samples

	Temperature range	**Location**
Oven 1	293 - 1273 K	EPFL
Oven 2	293 - 550 K	CERN
Refrigerator	243 - 293 K	EPFL
Cryostat cooled by liquid nitrogen	77 - 200 K	CERN
Cryostat cooled by liquid helium	1[a] - 150K	CERN

Table 4.1. Available temperature-stabilized environments

a. Temperatures below 4.2 K (liquefaction point of He at atmospheric pressure) are obtained thanks to partial evaporation.

The aim of the present work was to measure the variation of Brillouin gain curves over the maximal temperature range, that is as long as light propagates within the optical fibers. It turns out that the fiber, despite its discouraging prone-

ness to untimely breaking due to ill-handling, can withstand temperatures as low as 1 K[1] and as high as 1000 K while still guiding light. To cover the whole span, different installations are obviously necessary. We had at our disposal the facilities summarized in table 4.1, either in Lausanne (EPFL) or in Geneva (CERN)

In all these installations, we tried to ensure the homogeneity of the temperature along the fiber, by disposing it on a metallic, heat conducting support and by letting a sufficient time for thermalization after each temperature modification. However, some abnormally broad BGS were also measured, meaning that our precautions were not always sufficient.

A second, more fundamental issue is the precise determination of the temperature. The thermometers were different for each facility and were not recently calibrated (apart from the thermistances in the cryostat); in the absence of an overall reference, some mismatch may arise at the junctures of the curves.

The third factor that somehow makes the measurement less unambiguous than we could wish is the fact that we sometimes used other measuring setups, namely distributed ones[2]. We refer to the chapter 5 for their description. Since they work with other light sources (DFB diodes at 1552 or 1555 nm), they give other values of the Brillouin shift and linewidth than the setup relying on the YAG laser. We can still make sense of these by 'scaling' them to their respective values for a 1319 nm lightwave, as explained in the next section, but the procedure does not ensure the same precision as a genuine measurement at 1319 nm.

We will present results about the five fibers described in table 4.2. Unfortunately, due to various causes such as accidental sample destruction or limited availability of the cooling facility, no single fiber can be considered as completely studied over the whole temperature range. Yet the obtained curve segments are enough to describe qualitatively the parameters of the BGS, since the general behavior turns out to be independent of the fiber type.

1. This limit is not set by intrinsic properties of the fiber, but rather by the practical difficulty of putting at least a few tens of meters of fiber inside the advanced cryogenic facilities required for further decrease in temperature.

2. In this case, the distributed nature of the measurement has no relevance, since the fiber is homogeneous. The BGS are identical at each position along it.

	Fiber type	GeO_2 in core[a]	Jacket	Temperature range [K]
F1	Standard SMF; jacket chosen for high-temperature applications	2.75%	polyimide	4.2 77-1050
F2	Standard SMF	3.15%	acrylate	1.5 - 140
F3	F-doped fiber; pure silica core	0%	acrylate	1.5 - 300
F4	Payout^{TM} fiber; smaller core, designed to enhance nonlinear effects	9%	acrylate	1.5 - 300
F5	Dispersion-compensating fiber; small core, high GeO_2 concentration	20%	acrylate	1.5 - 300

Table 4.2. Studied fiber samples

a. The values for F1 and F2 are only indicative, being retrieved from the Brillouin shift value at ambient temperature by applying the linear relation between GeO_2 concentration and Brillouin shift given by Niklès [7].

4.3 Experimental results

4.3.1 Parameters of the Brillouin gain curves

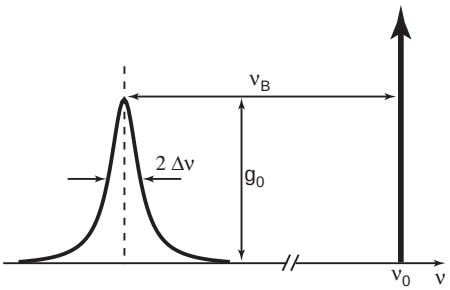

Figure 4-6. Definition of the parameters of the Brillouin gain curve. ν_0 is the pump frequency.

The Brillouin gain spectrum was shown to be Lorentzian-shaped :

$$g_B(\nu) = g_0 \frac{\Delta\nu^2}{(\nu - \nu_B)^2 + \Delta\nu^2} \tag{4.4}$$

In figure 4-6, the parameters of the curve are reported. Note in particular that, by convention, $\Delta\nu$ represents the half-width at half-maximum; this definition will remain valid for all subsequently presented results.

Once the experimental curves are obtained by equation (4.3), we retrieve the parameters of the Lorentzian by a standard fit procedure :

- the central frequency ν_B (Brillouin shift); it is inversely proportional to the pump wavelength.
- the half-linewidth $\Delta\nu$; contrary to the central frequency that is a relatively noise-immune value (in the sense that it can be determined with accuracy even from noisy measured data), the calculated half-linewidth depends crucially on the quality of the experimental curves. Notably the frequency span encompassed has to be broad enough; the fit procedure may otherwise yield aberrant values. As far as its dependency on the pump wavelength is concerned, we will assume for comparative purposes that $\Delta\nu \propto \lambda_p^{-2}$ but keep in mind that the real dependence is slightly different [8 p. 373] : experimentally reported dependences sway between $\Delta\nu \propto \lambda_p^{-1.2}$ and $\Delta\nu \propto \lambda_p^{-2.7}$.
- the gain value g_0; there will be no quantitative results about the peak value of the BGS here, apart from references to previous works; only qualitative trends will be indicated. The absence of systematic calibration of the optical powers involved in our measurements is the main cause of this regrettable absence. Besides, the effective area of the propagating modes in fibers are not known with precision, and the polarization issues were not consistently handled.

4.3.2 Linear domain

The linear variation of the Brillouin shift with temperature around the usual ambient temperature is very well documented [9-11]. As an example, figure 4-7 shows the Brillouin gain spectra of the fiber F5 for three temperatures. On top of the drift of the central frequency, we can notice the narrowing of the curves as the temperature increases, as well as the concomitant increase in the peak value of the gain.

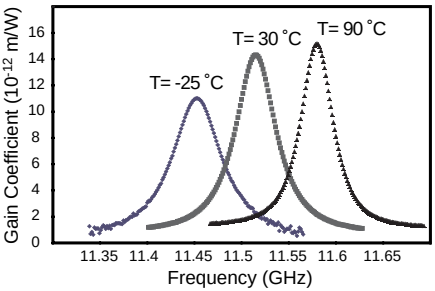

Figure 4-7. BGS of fiber F5 around ambient temperature @1319 nm. Measurements by Niklès [11].

This behavior is general, as was proved by Niklès' measurements on many fiber samples [7]. He demonstrated a quasi-perfect linearity over the temperature range -30 to 90°C (240 - 360 K), the slopes of the regression lines lying between 1.053 and 1.361 MHz/°C depending on the fiber type. Such a clean dependency on temperature makes the Brillouin shift an effective thermometer, and much work was indeed devoted to put it into practice; the distributed sensors like those that will be presented in the next chapter are the most promising examples. As far as the linewidth is concerned, Niklès and others [5] were also able to show that the increase in the gain peak value exactly compensates for the narrowing of the spectrum, so that the product $g_0(T)\Delta\nu(T)$ assumes a constant value.

Our measurements are not at variance with the previous literature; they rather supplement the already published results by extending the explored temperature range, thus enabling the determination of the limits of the linear domain. It turns out that the curves $\nu_B(T)$ closely follow a straight line from about -100°C up to 300°C. The next subsection will show how they depart from it in the high- and low-temperature regimes; in both cases, the transitions are rather gentle than abrupt. The figure 4-8 shows the Brillouin shift of four fibers as a function of temperature, and table 4.3 gives the associated numerical values. The slopes $d\nu_B/dT$ are compatible with the previously measured ones, as are the normalized slopes $\frac{d\nu_B}{dT}/\Delta\nu$ and the half-linewidths at ambient temperature.

	ν_B @ 25°C [GHz]	$\Delta\nu$ @25 °C [MHz]	Slope $d\nu_B/dT$ [MHz/K]	$\frac{d\nu_B}{dT}/\Delta\nu$ [ppm/K]
F1	12.808	12.2	1.142	89.1
F2[a]	12.766	-	-	-
F3	12.987	16.4	1.829	140.8
F4	12.133	20.1	1.359	112
F5	11.514	19.7	1.204	104.6

Table 4.3. Parameters of the BGS of the fibers under study

a. The data set for F2 is incomplete.

The narrowing of the BGS with increasing temperature was also found, and it is presented in figure 4-9. The slope of this variation increases as the temperature gets nearer to the acoustic absorption peak located around 110 K (see section 4.3.4).

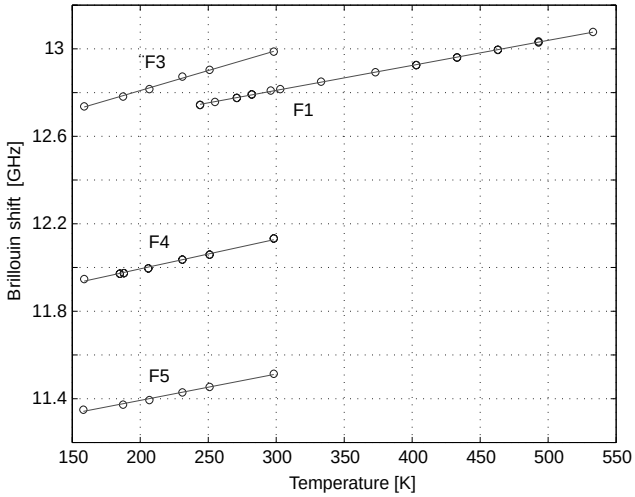

Figure 4-8. Brillouin frequency shift variation with temperature in the linear domain.
o measured data
—— linear regression

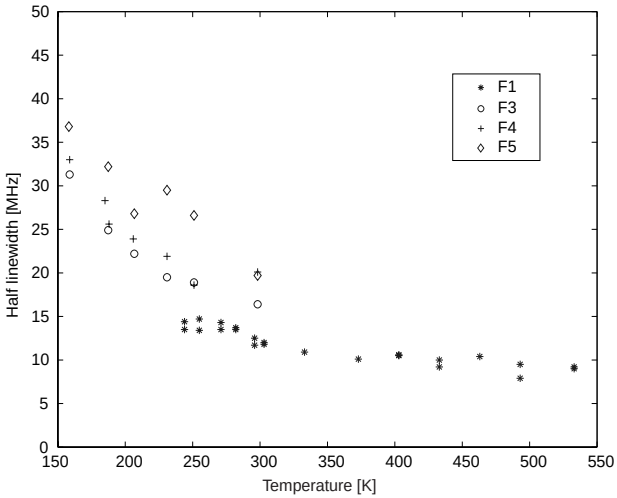

Figure 4-9. Brillouin linewidth variation with temperature in the linear domain

4.3.3 High-temperature domain

The Brillouin properties of optical fibers at high temperature (say above 100°C to give an approximate lower limit) have been much less investigated than those at quasi-ambient temperature. This is perhaps partly due to the smaller number of potential applications and to the fact that telecom fibers rarely experience such environmental conditions, but another reason was probably prevailing : most fibers do simply not survive these temperatures.

The silica or Ge-doped silica constituting the core and the cladding of the fiber is not to blame for this poor survival ability, at least in the initial heating phase. Its fusion point and even its glass transition temperature lie well above 1000°C, what effectively prevents any melting or softening up to this range of temperatures. On the contrary, the material making up the protective jacket lacks this enviable endurance; acrylate for example, the routinely used polymer for coating, melts at ~100°C. This leads the suppliers to indicating slightly lower maximal operating temperatures for their optical fibers. There are other available coating materials, some of them being summarized in table 4.4. Metals (aluminum or gold sheets) exhibit the best performance in terms of maximal temperature, but

they are rather expensive and their removal, necessary for splicing purposes, involves tedious handling of chemicals. Polyimide presents more attractive features. It can withstand pretty high temperatures at an affordable price, while its handling, albeit not as easy as that of acrylate-coated fibers, does not require a chemistry laboratory : a lighter or some matches suffice.

Jacket	Max. temperature	Indicative price	Removal method
Acrylate	85°C	Negligible	Mechanical fiber stripper
Polyimide	385°C	~5 $/m	Burning or sulfuric acid
Aluminum	400°C	~15 $/m	Chemical etch with sodium hydroxide
Gold	700°C	~30 $/m	Chemical etch with hydrochloric acid

Table 4.4. Some available jacket materials for high-temperature applications of fibers

The chosen polyimide coated fiber can be heated reversibly (that is without undergoing any permanent change) up to 400°C. Above this value, polyimide breaks down, but it turns out that it disappears very neatly; contrary to the acrylate, it evaporates in the oven, leaving the glassy central part of the fiber unmodified, in particular as far as its light guiding properties are concerned. With proper care[1], we could thus carry on with our measurements at higher temperatures.

Yet another phenomenon sets an upper limit to the experiment : between 750°C and 800°C, annealing begins; much accelerated diffusion of the Ge ions from the core to the cladding takes place, decreasing the refractive index difference and ultimately preventing light guiding. In parallel, small volumes of glass undergo crystallization, making the fiber partially polycrystalline and exceedingly brittle. As a matter of fact, it became so frail that it broke without any external mechanical intervention, effectively terminating the data acquisition.

The results of our measurements are presented in the figures 4-10 and 4-11. The Brillouin shift is shown to increase over the whole temperature range, following the trend observed at ambient temperature. But the slope $d\nu_B/dT$ can no longer be considered a constant. The linear regressions presented in figure 4-10 demonstrate this variation : the first one, calculated on the first few experimental points,

1. The absence of the mechanically protective layer obviously makes the fiber more fragile. Hence ‘proper care’ means basically ‘touching the sample as little as necessary’.

exhibits a slope 1.14 MHz/K that corresponds to that of the same fiber in the linear domain as represented in figure 4-8. The second one, calculated on the last few points, has a 0.81 MHz/K slope. How does the transition takes place from one to the other of these values ? Our measurements seem to support a smooth transition over an extended temperature range, but this is not certain. Further work would be needed to discriminate with confidence between the continuous transition we favor on the present limited basis or a possible abrupt change of slope. Such a discontinuity may be somehow related to the short-range order modifications that are known to cause a phase transition between α- and β-quartz at 573°C in crystalline SiO_2. But the disappearance of the polyimide coating[1] can more probably explain the change in the slope. It is known [7, p. 117] that temperature changes of the coating induce a strain in the fiber that participates in the overall drift of the Brillouin frequency shift of the fiber. When the jacket is suddenly (or progressively ?) removed, only the intrinsic variation of ν_B with T in silica remains.

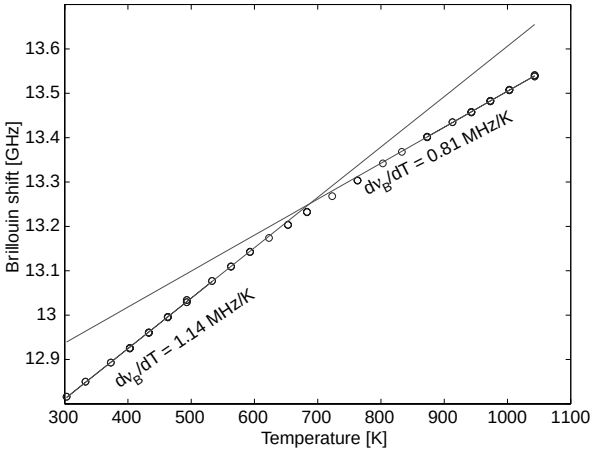

Figure 4-10. Brillouin shift @1319 nm in fiber F1 up to fiber destruction temperature. The indicative linear regression shown correspond to respectively the first and the last five experimental points.

1. We did not document the phenomenon, but it should occur at temperature slightly higher than the maximal operating temperature claimed by the supplier, that is 385°C, which correspond to the intersection of the two lines in figure 4-10.

As always, for reasons mentioned in section 4.3.1, the results concerning the linewidth are less clear than those about the Brillouin shift. However, figure 4-11 allows us to make a few statements over the evolution of the former at high temperature. First the decrease of the linewidth with increasing temperature observed at ambient or slightly higher temperature does not go on forever. The large dispersion of the experimental points prevents us from being too categorical, but it seems highly probable that a minimal value is reached somewhere between 500 K and 600 K. Then the linewidth remains constant at least up to 900 K.

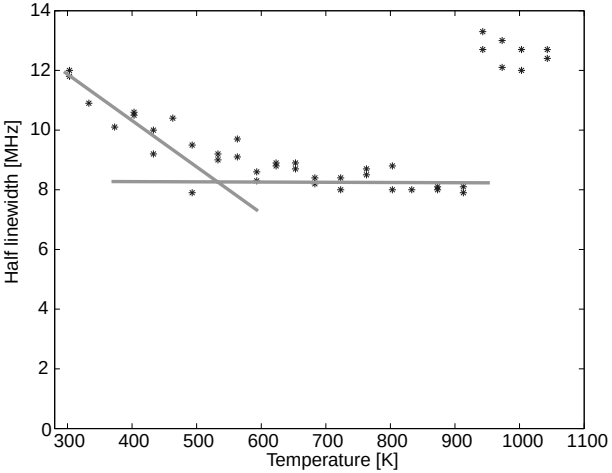

Figure 4-11. Brillouin linewidth @1319 nm in fiber F1 up to fiber destruction temperature. The lines are merely guides to the eye.

The last few points are hard to interpret. According to the literature [12], an increase in the sound absorption, and consequently in the Brillouin linewidth, is to be expected in this region. But we cannot make much sense of such an abrupt jump to a value clearly higher than the previously mentioned quasi-constant. Since they were measured on another sample[1] than the other points, they could be explained by a poorer homogeneity of this fiber, or by some different residual stress of undetermined origin. But the explanation could also be related to the first stage of the phenomena that later led to the fiber destruction; even a small variation of the refractive index profile may have an impact on the shape of Bril-

1. Another sample of the same fiber of course, as proved by the continuity of the $\nu_B(T)$ curve in figure 4-10.

louin gain spectra. Here again, further measurements would be needed, with a carefully chosen procedure : as the tests are destructive, one should first ensure that all samples are identical; besides, the thermal cycles (duration and slope of the temperature ramps, possible plateaus...) should be identical or at least modified in a controlled way, if such slow processes as ions diffusion do indeed intervene.

4.3.4 Low-temperature domain

The very low to low temperature domain has so far failed to arouse a great interest among the fiber optics specialists. This is quite understandable from telecom engineers, since they do not encounter such extreme conditions (that may still come, though, in spatial applications). But people dealing with fiber sensors could find here applications[1].

On the other hand, solid-state physicists have shown by investigation of bulk samples that vitreous silica, as was briefly reviewed in the chapter 2 of this work, far from extrapolating its properties measured at ambient temperatures, behaves differently below 150 K. Yet, to our knowledge, nobody has bothered to put an optical fiber, i.e. basically a cylindrical sample of silica, in a cryostat and to cool it down to liquid helium temperature in order to look at its evolution.

That we did, and the first thing we learned from it is that the fiber keeps its light guiding properties. Contrary to some fears, it does withstand the thermal variation without breaking; moreover, OTDR measurements have shown only a marginal increase of the linear light attenuation. It is probable that the fiber would not stand the same mechanical deformation as in normal conditions due to the cold-induced stiffness of its polymer jacket, but it was inaccessible when cooled in the facility at our disposal, so we could not check this point. In any case, when the fiber is re-heated, it assumes its initial mechanical properties again.

1. Admittedly not in the everyday life of the lambda consumer, but large cryogenic facilities are not that rare in the big laboratories.

We were able to measure the characteristic values of the Brillouin gain spectra down to 1.5 K; the figure 4-12 presents the results for the fiber F2.

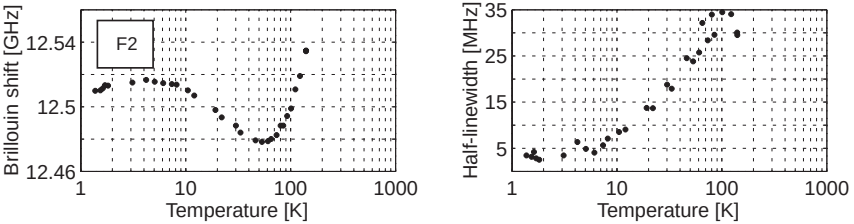

Figure 4-12. Brillouin frequency shift and linewidth in fiber F2 as functions of temperature from 1.5 K to 150 K. Original measurements @ 1555 nm.

The most striking features in the $\nu_B(T)$ curve are an absolute minimum around 60 K, the subsequent increase with decreasing temperature up to a maximum located at 4 K and a new decrease for still lower temperatures. As for the linewidth, $\Delta\nu(T)$ exhibits a maximum in the 110 K range (remember its negative slope in the so-called linear domain) and a steady decrease down to an exceedingly low value (<2MHz) at a few K. Confirming results obtained by Le Floch [5], the linewidth seems to be constant between 1 K and 4-5 K.

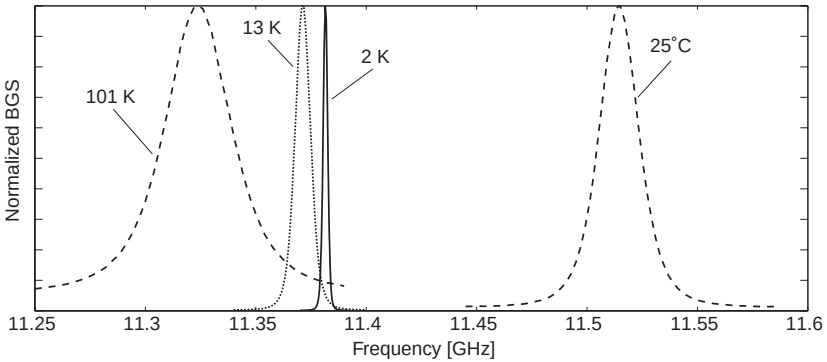

Figure 4-13. Measured Brillouin gain spectra in fiber F5 at three cryogenic temperatures and, for comparison, at ambient temperature. Each curve is independently normalized.

Such a large variation (more than one order of magnitude) of the linewidth necessitates some adaptations in the measuring setup : it is evident that the frequency range that has to be encompassed as well as the required frequency resolution differ strongly for the various curves shown in figure 4-13. What is not repre-

sented here, and has caused more practical difficulties, is the variation of the peak value of the Brillouin gain. Although we can neither confirm nor refute the empirical law, valid in the linear domain, according to which the product $\Delta\nu(T)g_0(T)$ is a constant, it was clear that the narrowing of the Brillouin linewidth goes always together with an increase in the Brillouin gain. Below 6 K, we had to manually decrease the pump power to avoid saturation of the detector, while this same power was scarcely enough to yield usable BGS at 100 K.

An unexpected problem related to the huge Brillouin scattering efficiency at the lowest end of the temperature range was the presence of such an amount of spontaneous Brillouin scattering that it hindered the measurement of stimulated scattering by depleting the pump. The figure 4-14 shows a part of the spectrum of the light that gets backscattered in the fiber without any probe signal to initiate stimulated processes. Beyond any doubt, these frequency components are the signature of spontaneous Brillouin scattering. It is not straightforward, to say the least, to explain this high efficiency precisely at very low temperature. The number of thermal phonons available to scatter the pump photons is small, and we would consequently rather expect a decreased efficiency. Notwithstanding the incomplete understanding of the phenomenon, sufficient attenuation of the pump power allowed us in practice to bypass this hindering peculiarity.

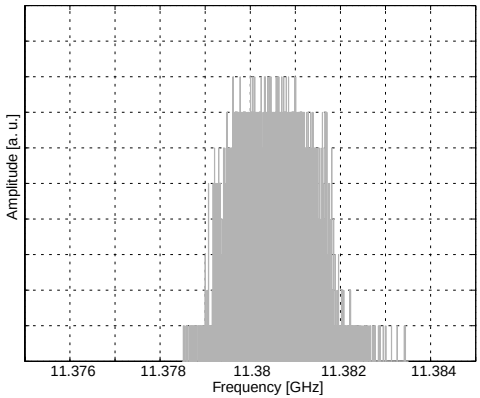

Figure 4-14. Spontaneous Brillouin backscattered spectrum at 2.6 K in fiber F5 without probe wave.

The overall look of the curves $\nu_B(T)$ and $\Delta\nu(T)$ is strikingly similar for various fibers. This is proved by the figure 4-15, which shows these curves for the three specialty fibers F3, F4 and F5. Still, some discrepancies are noticeable. The dif-

ference in the Brillouin shift between the maximum and the minimum increases with the concentration of GeO_2 dopant in core : it is roughly 40 MHz for pure silica core, 50 MHz for 9 % concentration and 60 Mhz for 20 % concentration.

In parallel, the positions of the extrema drift toward higher temperatures. This trend is clear for the minimum, only plausible for the flat maximum where experimental noise does not allow us to discard the possibility of an artefact. The special acoustic properties of the fiber F3 (F-doped cladding), mentioned in section 3.4.1, play here against us : due to the supplementary acoustic modes visible in the Brillouin gain spectra (see figure 3-11), the determination of the central frequency of the main peak is less precise, and that of its linewidth is impossible. To denote that reduced confidence in our results, we use empty circles for the concerned points in the top left frame of figure 4-15.

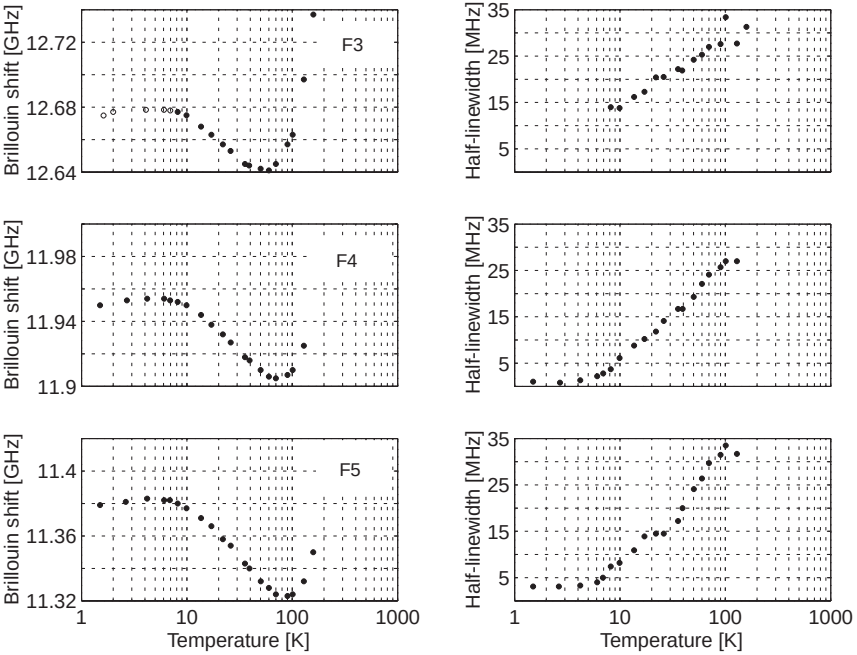

Figure 4-15. Brillouin frequency shift and linewidth in fiber F3, F4 and F5 as functions of temperature from 1.5 K to 150 K. Original measurements @ 1319 nm. The empty circles in the top left frame are derived from multi-peak spectra.

As far as the Brillouin linewidth is concerned, the quantity and quality of our data are insufficient to support any statement more detailed than the obvious general

agreement between the three fibers : all exhibit a maximum of 30-35 MHz around 110 K and the same linear decrease [13] as the fiber F2 for decreasing temperatures. The plateau region [14]is also present between 1 K and 5 K, only being unobservable in F3 for the aforementioned reason.

4.3.5 Summary and discussion

To summarize our experimental results, we present here in a single figure (figure 4-16) our measurements of the Brillouin shift in the fiber F1 over the whole investigated temperature range. In addition, figure 4-17 gives the same points on a logarithmic temperature scale, supplemented by data borrowed and adapted from measurements on the fiber F4. The adaptation consists in adding 700 MHz to the original measured values, so that they coincide with those of F1 at the reference temperature 4.2 K. Because of the already mentioned absence of measurements on F1 between 4.2 K and 77 K, this was the only reasonable way to show a complete curve from 1 to 1000 K. This rather cavalier procedure is partly justified by the approximate parallelism between the curves $\nu_B(T)$ for all the fibers visible in figure 4-15.

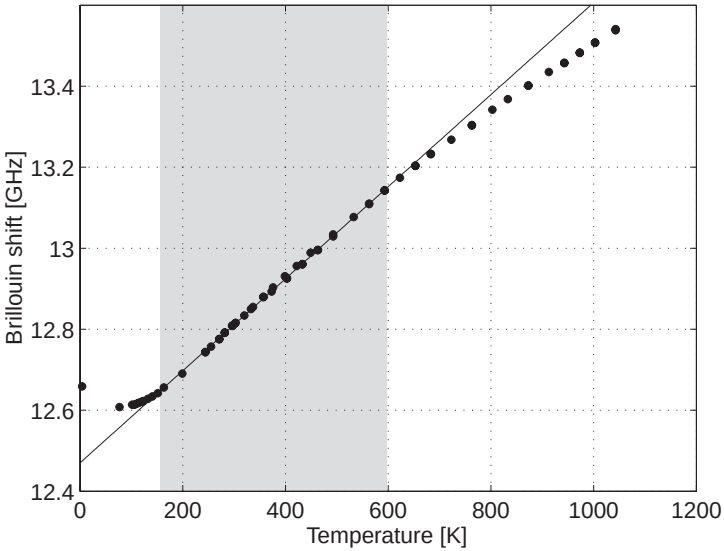

Figure 4-16. Brillouin shift vs temperature in fiber F1. The greyed zone indicates the linear region.

In order to facilitate comparisons with literature, especially with measurements in bulk silica, it would be useful to convert the Brillouin shift values into the proportional sound velocities (3.52). Yet this would require a complete knowledge of the refractive index *n* of our fiber at the wavelength of our light sources at each temperature. Unfortunately, we did not have an opportunity of measuring it, nor did we find a suitable calibration table. However, the available partial information [15-18] allows us to estimate this dependence : it is weak, of the order of 0.1% /100K at high temperatures, even less below 300 K. This is not enough to substantially alter the overall features of the curve 4-16, so we choose not to discuss this point here.[1] We will therefore further consider the refractive index as a constant.

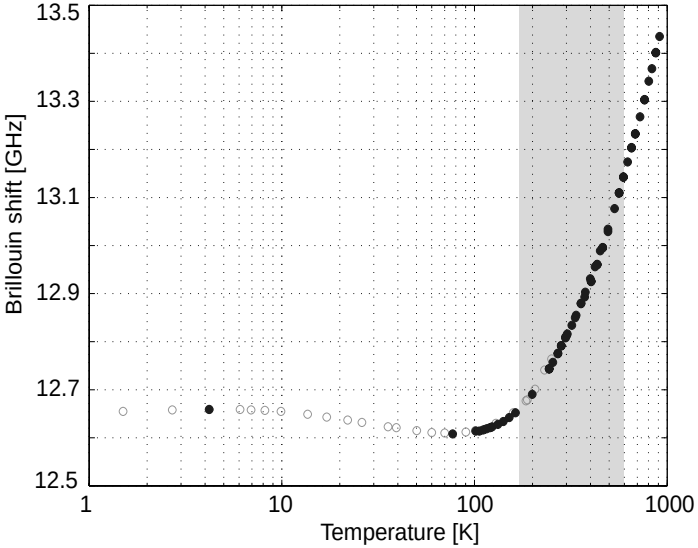

Figure 4-17. Brillouin shift vs temperature in fiber F1 (full circles) completed in the low-temperature range by *shifted* data for fiber F4 (empty circles). Due to the difference in dopant concentration, the real $\nu_B(T)$ curve for F4 lies 700 MHz below the represented one (see text). As in the previous picture, the linear region is denoted by the greyed surface.

1. Besides, in practical sensing applications, the sound velocity is kept a 'hidden variable', because the Brillouin shift (including its dependence on refractive index) is directly used as a measurement of the temperature.

The greyed region in figures 4-16 and 4-17 highlights the temperature range over which the Brillouin shift variation with temperature can be considered linear. It stretches out roughly from 150 K to 600 K. Beyond this upper limit, the slope decreases. Although we can not decide up to which extent this decrease is due to the removal of the fiber coating (see the discussion in section 4.3.3), comparison with measurements in bulk silica (figure 2-21) indicates that it is at least partly an intrinsic phenomenon.

Below the linear region, the now usual minimum in Brillouin shift is found. As a consequence of the abysmal gap in experimental data for F1, we discuss here the corresponding segments of the curves F3, F4 and F5 (figure 4-15), which have the additional advantage of allowing us to observe the effects of an increase in the Ge concentration.

Measurements of the sound velocity in pure a-SiO_2 and pure a-GeO_2 (figure 4-18) show a similar qualitative behavior. This is quite normal, since both materials share many similarities at the atomic scale (same covalent bindings of approximately the same length, same short-range order based on tetrahedra) as well as in their structure (continuous random network). Yet they show marked differences in the numerical parameters :

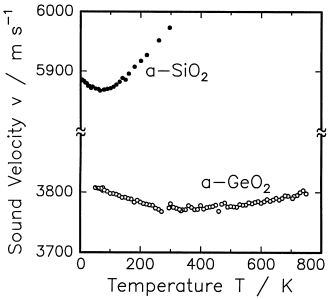

Figure 4-18. Sound velocity variation with temperature in amorphous silica and germanium dioxide. From [14]

	Temperature of the minimum	**Sound velocity**
a-SiO_2	~70 K	~5900 m/s
a-GeO_2	~300 K	~3800 m/s

In accordance with intuition, the behavior of the fibers F3 to F5 (with respectively 0%, 9% and 20% a-GeO_2 concentration in the core) exhibits intermediate

features between these two extreme cases : the temperature of the minimum drifts toward higher values, and the sound velocity decreases

The intrinsic property of glass that is related to the Brillouin linewidth is the internal friction Q^{-1}, which is directly retrieved from our measurements through

$$Q^{-1} = \frac{2\Delta\nu}{\nu_B}. \tag{4.5}$$

The measured curve $Q^{-1}(T)$ (figure 4-20) can be compared with measurements in bulk, as those of figure 4-19, again for pure a-SiO_2 and a-GeO_2. It is important to take into account the wavelength of the used lasers, as the internal friction strongly depends on it. Since $\Delta\nu \sim 1/\lambda^2$ and $\nu_B \sim 1/\lambda$ in the frequency and temperature range of interest, we expect a $Q^{-1} \sim 1/\lambda$ dependence[1]. Scaled to the same wavelength, the internal friction measured in 4-19 (Ar-ion laser @488 nm, i.e. acoustic frequency of 36 GHz) is smaller than that of 4-20 (Nd:YAG laser @1319 nm, i.e acoustic frequency of 12 GHz); that difference of about 25% may be explained by the presence of Ge in the fiber, as the right part of figure 4-19 shows that internal friction is greater in a-GeO_2.

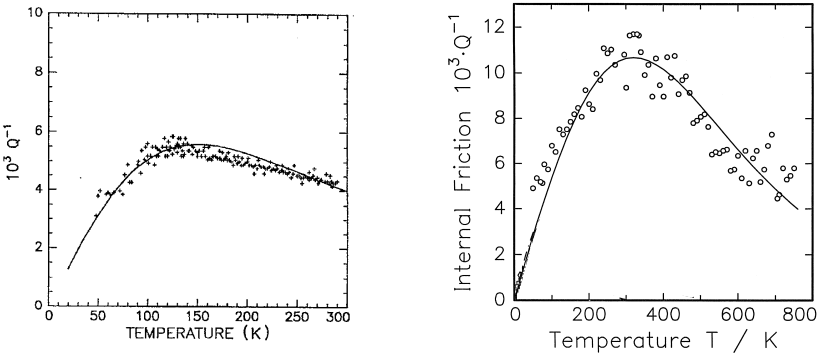

Figure 4-19. Internal friction variation in silica [19] (left) and germanium dioxide [14](right), measured by Brillouin scattering @ 488 nm.

The most conspicuous feature of all $Q^{-1}(T)$ or $\Delta\nu(T)$ curves in the cryogenic temperature range measured in our fibers is the broad maximum occurring at 110 K. This maximum is known as the absorption peak (also boson peak in certain

1. These approximations may no longer be valid at very low temperatures (below 10 K).

papers) and is a universal characteristic of glasses. Its position T_{max} in temperature varies with the acoustic frequency considered [5, 19, 20] according to the relation

$$\ln(\Omega) = \ln\left(\frac{1}{\tau_0}\right) - \frac{V_0}{k_B}\left(\frac{1}{T_{max}}\right), \tag{4.6}$$

where τ_0 and V_0 are parameters that must be determined from measurements. A dependence of the form (4.7) is the signature of a thermally activated relaxation process. The two-level systems model introduced in chapter 2 has been proposed precisely to explain this behavior[1].

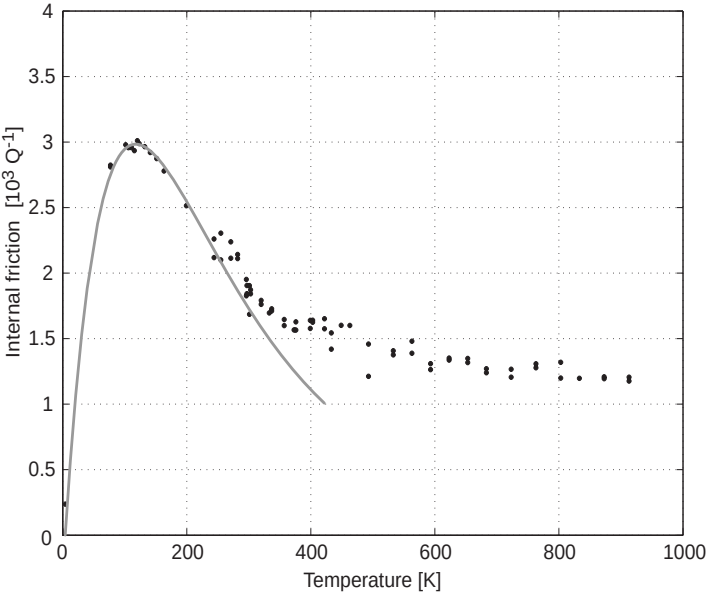

Figure 4-20. Internal friction vs temperature in fiber F1. Black dots : experimental points; grey line : fit of the absoption peak after equation (4.15).

It has been shown [21] very early in the history of the modern theory of glasses that the internal friction of a set of TLSs is given by

1. Not only the absorption peak, though, but also numerous properties at lower temperatures.

$$Q^{-1} = \frac{D^2}{\rho v_A^2}\int_0^\infty d\Delta \int_0^\infty dE P(E,\Delta)\frac{1}{k_B T}\left(\frac{\Delta}{E}\right)^2 \operatorname{sech}^2\left(\frac{E}{2k_B T}\right)\frac{\Omega\tau}{1+(\Omega\tau)^2}. \qquad (4.7)$$

We refer to the section 2.5, particularly the figure 2-24, for the definitions of the parameters of the double wells that constitute these TLSs. Δ is an asymmetry energy (difference in the depths of the wells), while E is the energy splitting of the two lowest levels of the system, dependent in particular on the barrier height V. Both quantities exhibit a distribution $P(E,\Delta)$, owing to the random nature of the solid. The constant D, defined in (2.20), is the deformation potential that describes how E reacts to a deformation of the structure, and ρ is the material density. The relaxation time τ depends on the barrier height as

$$\tau = \tau_0 \exp\left(-\frac{V}{k_B T}\right), \qquad (4.8)$$

that is its classical form for a thermally activated relaxation process.

Rewriting (4.7) in terms of barrier height, and with the reasonable assumption [19] that $E \approx \Delta$, we get,

$$Q^{-1} = \frac{D^2}{\rho v_A^2}\int_0^\infty d\Delta \int_0^\infty dV P(V,\Delta)\frac{1}{k_B T}\operatorname{sech}^2\left(\frac{\Delta}{2k_B T}\right)\frac{\Omega\tau}{1+(\Omega\tau)^2} \qquad (4.9)$$

A similar expression for the associated sound velocity variation may be derived :

$$\frac{\delta v_A}{v_A} = -\frac{D^2}{\rho v_A^2}\int_0^\infty d\Delta \int_0^\infty dV P(V,\Delta)\frac{1}{k_B T}\operatorname{sech}^2\left(\frac{\Delta}{2k_B T}\right)\frac{1}{1+(\Omega\tau)^2} \qquad (4.10)$$

The equation (4.10) describes satisfactorily the decreasing section of the sound velocity vs. temperature curves, between ~10 K and 50 K. Its validity range stops when a concurrent mechanism with inverse temperature dependence becomes prevailing, causing the minimum at 70 K and then the linear increase up to ambient temperatures and beyond. Unfortunately, this mechanism is still unknown, what regularly prompts the authors of the papers that mention this problem to set this aspect beyond the scope of their work. We follow their example.

To go further than (4.9) about the absorption peak, we have to define the distribution of the parameters Δ and *V*. In view of the homogeneity in randomness of the silica, a uniform distribution in the asymmetry energy makes sense. For the barrier heights, we choose as an attempt an exponentially decreasing distribution, so that

$$P(\Delta, V) = \frac{P_0}{V_0}\exp\left(-\frac{V}{V_0}\right) \tag{4.11}$$

With this distribution, the integration over Δ in (4.9) is straightforward :

$$\int_0^\infty d\Delta \operatorname{sech}^2\left(\frac{\Delta}{2k_BT}\right) = 2k_BT. \tag{4.12}$$

The second integration, over the barrier heights *V*, is more cumbersome. In most publications [14, 19], it is carried out numerically in order to fit experimental data. Nevertheless, after Le Floch [22], it can be solved analytically using special functions as

$$\int_0^\infty dV \frac{P_0}{V_0}\exp\left(-\frac{V}{V_0}\right)\frac{\Omega\tau_0\exp(V/k_BT)}{1+\Omega^2\tau_0^2\exp(2V/k_BT)} = \frac{k_BTP_0}{\Omega^2\tau_0^2(k_BT+V_0)} \times {}_2F_1\left[1, \frac{1}{2}\left(1+\frac{k_BT}{V_0}\right); \frac{1}{2}\left(3+\frac{k_BT}{V_0}\right); -\frac{1}{\Omega^2\tau_0^2}\right] \tag{4.13}$$

where ${}_2F_1[a, b; c; d]$ is the Gauss hypergeometric function defined by

$${}_2F_1[a, b; c; z] = \sum_{k=0}^{\infty} \frac{a \cdot b}{c}\frac{z^k}{k!}. \tag{4.14}$$

The internal friction variation as a function of temperature is then expressed as

$$Q^{-1} = \frac{D^2P_0}{\rho v_A^2}\frac{1}{\Omega^2\tau_0^2}\frac{k_BT}{(k_BT+V_0)} \times {}_2F_1\left[1, \frac{1}{2}\left(1+\frac{k_BT}{V_0}\right); \frac{1}{2}\left(3+\frac{k_BT}{V_0}\right); -\frac{1}{\Omega^2\tau_0^2}\right] \tag{4.15}$$

The conspicuous agreement between experimental points and the curve fitted according to (4.15) in figure 4-20 supports the validity of the model. Values of $\tau_0 = 4\times10^{-14}$ s and $V_0/k_B = 585$ K, deduced from reported measurements of

the temperature of maximal absorption with respect to frequency (see [14, 22]) were chosen. However, it must be added that acceptable agreement has also been reported with different forms (Gaussian or even uniform) of the distribution function $P(\Delta, V)$ [20], suggesting that measurements of the absorption peak are not sufficient to retrieve the details of the two-level systems model of silica.

Besides, as for the sound velocity, another mechanism has to be invoked to explain why (4.15), or the more general form (4.9) is no longer valid at temperatures above the absorption peak.

References

[1] *N.L. Rowell, P.J. Thomas, H.M. van Driel, G.I. Stegeman*
Brillouin spectrum of single-mode optical fibers
Appl. Phys. Lett., **34**(2), p. 139-141 (1979).

[2] *N. Shibata, R.G. Waarts, R.P. Braun*
Brillouin gain for single-mode fibers having pure silica, GeO2-doped and P2O5-doped cores
Opt. Lett., **12**, p. 269-271 (1987).

[3] *M. Niklès, L. Thévenaz, P.A. Robert*
Simple distributed fiber sensor based on Brillouin gain spectrum analysis
Opt. Lett., **21**(10), p. 758-760 (1996).

[4] *B.E.A. Saleh, M.C. Teich*
Fundamentals of photonics
Wiley, New York (1991).

[5] *S. Le Floch*
Etude de la diffusion Brillouin stimulée dans les fibres optiques monomodes standard. Application aux capteurs de température et de pression
Ph.D. Thesis Université de Bretagne occidentale, Brest (2001).

[6] *S. Le Floch, P. Cambon*
Study of Brillouin gain spectrum in standard single-mode optical fiber at low temperatures (1.4 to 370K) and high hydrostatic pressures (1 to 250 bars)
Opt. Commun., (to be published).

[7] *M. Niklès*
La diffusion Brillouin dans les fibres optiques : étude et application aux capteurs distribués
Ph.D. Thesis EPFL, Lausanne (1997).

[8] *G.P. Agrawal*
Nonlinear fiber optics
2nd ed. Academic Press, San Diego (1995).

[9] *T. Kurashima, T. Horiguchi, M. Tateda*
Thermal effects on the Brillouin frequency shift in jacketed optical silica fibers
Appl. Opt., **29**(15), p. 2219-2222 (1990).

[10] *T.R. Parker, M. Farhadiroushan, V.A. Handerek, A.J. Rogers*
Temperature and strain dependence of the power level and frequency of spontaneous Brillouin scattering in optical fibers
Opt. Lett., **22**(11), p. 787-789 (1997).

[11] *M. Niklès, L. Thévenaz, P.A. Robert*
Brillouin gain spectrum characterization in single-mode optical fibers
J. Lightwave Technol., **15**(10), p. 1842-1851 (1997).

[12] *D.B. Fraser*
Acoustic loss of vitreous silica at elevated temperatures
J. Appl. Phys., **41**(1), p. 6-11 (1970).

[13] *A. Jagannathan, R. Orbach*
Temperature and frequency dependence of the sound velocity in vitreous silica due to scattering off localized modes
Phys. Rev. B, **41**(5), p. 3153-3157 (1990).

[14] *J. Hertling, S. Baessler, S. Rau, G. Kasper, S. Hunklinger*
Internal friction and hypersonic velocity in vitreous germania under high pressure
J. Non-Crystal. Solids, **226**(1-2), p. 129-137 (1998).

[15] *R.M. Waxler, G.W. Cleek*
The effect of temperature and pressure on the refractive index of some oxide glasses
J. Res. Nat. Bur. Stand (US), **77A**(6), p. 755-763 (1973).

[16] *N. Matsuoka, N. Kitamura, S. Fujinaga, T. Kitaoka, H. Yamashita*
Temperature dependence of refractive index of SiO2 glass
J. Non-Cryst. Solids, **135**, p. 86-89 (1991).

[17] *G. Ghosh*
Temperature dispersion of refractive indexes in some silicate fiber glasses
IEEE Photon. Technol. Lett., **6**(3), p. 431-434 (1994).

[18] *G. Ghosh, M. Endo, T. Iwasaki*
Temperature-dependent Sellmeier coefficients and chromatic dispersions for some optical fiber glasses
J. Lightwave Technol., **12**(8), p. 1338-1341 (1994).

[19] *D. Tielbürger, R. Merz, R. Ehrenfels, S. Hunklinger*
Thermally activated relaxation processes in vitreous silica - an investigation by Brillouin-scattering at high-pressures
Phys. Rev. B, **45**(6), p. 2750-2760 (1992).

[20] *J.P. Bonnet*
On the thermally activated structural relaxation in glasses
J. Non-Cryst. Solids, **127**(2), p. 227-231 (1991).

[21] *J. Jäckle*
Ultrasonic Attenuation in Glasses at Low-Temperatures
Z. Phys., **257**(3), p. 212-223 (1972).

[22] *S. Le Floch, F. Riou, P. Cambon*
Experimental and theoretical study of the Brillouin linewidth and frequency at low temperature in standard single-mode optical fibres
J. Opt. A-Pure Appl. Opt., **3**(3), p. L12-L15 (2001).

CHAPTER 5

Distributed temperature sensing

5.1 Introduction

Sensors come in many shapes and sizes, depending on the quantity they are intended to measure. Conceptually, they are defined by their function : to translate some aspect of the physical reality into information that can be understood by the human brain. Hence our sense organs, chiefly our eyes, are the first and most important sensors. To complement them, human ingenuity has designed innumerable devices, from the medical thermometer to the oscilloscope and the force-field microscope.

In an attempt to classify the sensors, the distinction between distributed and point sensors is very useful. Point sensors give information about a quantity, say the temperature to be illustrative, at their position. On the contrary distributed sensors - albeit located at one defined place - are able to ‘read’ the value of a parameter over an extended region. A well-know example is the radar : it can discriminate between the presence or the absence of a plane everywhere within its working range. For this second class of sensors, the sensing process requires two stages : first the detection itself, as in point sensors but now away from the instrument, that translates the physical quantity of interest into a signal. Then the transportation of this signal to the instrument. For the radar, the detection is the reflection of an electromagnetic pulse on a metallic surface, and the backward-reflected pulse propagates freely down to the antenna.

Optical fibers are specifically designed to convey signals; on the other hand, they interact with their environment, in the sense that some of their properties are modified by changes in external parameters[1]. They were thus perfectly equipped

1. The characteristics of the Brillouin gain spectrum, to take an example (nearly) at random.

to become parts of distributed sensing schemes; the interest of these applications for fibers was recognized in the 1970's. In the last twenty years, numerous conferences have been devoted to this field (e.g. the fifteen or so OFS conferences on optical fiber sensors); on top of their proceedings, some in-depth reviews [1, 2] and loads of research papers attest the vitality of the domain.

This chapter is concerned only with distributed temperature sensing in fibers using Brillouin scattering, tossing aside the applications where the strain has to be measured that were reviewed elsewhere [3-5]. We will begin with the description of our actual sensing system, from the principles to the figures of merit of its commercial version; a discussion of the physical effects limiting the ultimate performances will show how close we are to them. Then some examples of measurements will be given, in the usual temperature range as well as in the cryogenic range. We will finish by the presentation of preliminary work on two innovative schemes; while the first one (based on injection-locking) is merely a technical trick that avoids the use of an electro-optical modulator, the second (correlation-based technique) is conceptually different and opens new paths to overcome limitations that previously appeared unassailable.

5.2 Experimental setup

5.2.1 Principle of the instrument

The archetypal fiber distributed sensor is the optical time-domain interferometer (OTDR). Invented as early as 1976 [6, 7], it relies on Rayleigh scattering to measure the attenuation characteristics of the fiber. Its radar-like time-of-flight analysis is straightforward [8-10]: an intense pulse is launched into the fiber and the backscattered light is recorded; knowing the velocity of light in the silica, the temporal variations of backscattered power can be read as spatial variations, enabling the detection of bad splices or other regions with abnormally high losses. OTDRs are nowadays routinely used in the field to check the integrity and quality of optical links.

Rayleigh scattering being essentially independent of the temperature, standard OTDRs are not suitable candidates for distributed temperature sensors. Hence people had to turn to Raman or Brillouin scatterings. A first kind of sensor relies

on Raman effect [11, 12]; the ratio between the Stokes and the anti-Stokes backscattered Raman lines being highly sensitive to temperature, it is possible to retrieve this usable information behind the much more intense Rayleigh light, thanks to the large Raman frequency shift that makes it relatively easy to filter out the screening Rayleigh. Commercial systems based on this principle are currently available.

As for Brillouin scattering, this lacks the latter favorable feature. Other methods than simple filtering are thus necessary to dig out the weak signal from the Rayleigh noise. In the so-called Brillouin OTDR [13], the signal-to-noise ratio enhancement is provided by coherent detection : the backscattered wave is mixed with the light of a local oscillator of suitable wavelength, and the signal at the beating frequency is observed through an electrical spectrum analyzer.

A second, now widely recognized approach was presented in 1989 by Horiguchi *et al*. [14-16]. They named it BOTDA (Brillouin optical time-domain analysis). Rather than struggling to retrieve the weak product of spontaneous Brillouin scattering, they chose to take advantage of the much more efficient stimulated Brillouin scattering, and provided the required seed for the growth of the Stokes wave as a second, tunable laser source. Their idea was taken up by, among others, Niklès *et al*. [17], who proposed to use an electro-optical modulator to enhance the relative stability of the pump and probe waves, based on the reasons developed in chapter 3 in the framework of non-distributed measurements. Our group has been pursuing research in that direction under the acronym LASBI (local analysis of stimulated Brillouin interaction).

The principle of operation of such a sensor is depicted in figure 5-1. A pump pulse, whose width determines the spatial resolution of the measurements, is launched into the fiber. As in a standard OTDR, this triggers the acquisition of the backscattered optical power. But contrary to the OTDR case, the dominant component[1] of the backscattered light is the backward propagating signal wave amplified by Brillouin interaction when it crosses the pump pulse. By varying the frequency of the signal wave, it is possible to retrieve the Brillouin gain spectrum for every location along the fiber and ultimately the temperature[2], provided that the relation $\nu_B(T)$ is known for the considered fiber.

1. We will further see that some filtering before the detection remains necessary in order to get rid of Rayleigh scattering.

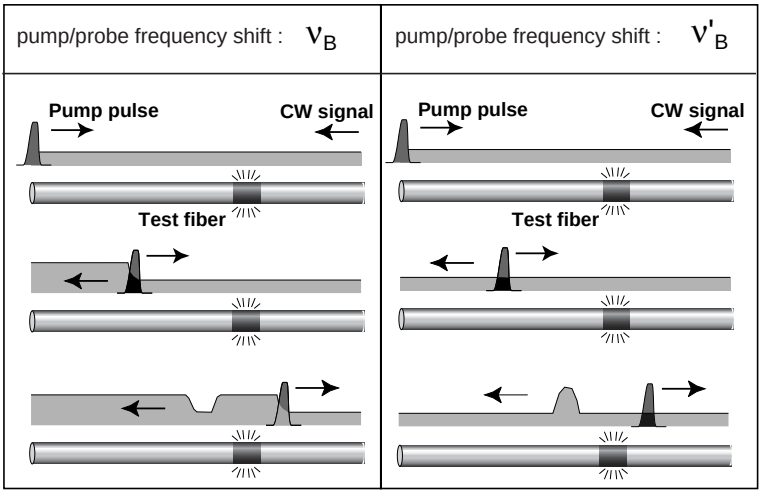

Figure 5-1. Principle of operation of a distributed sensor in a pulsed pump-CW signal configuration. Let us assume that the Brillouin shift of a fiber is ν_B under normal conditions, while its value shifts to ν'_B at some place due to heating. A frequency difference ν_B between the pump and the probe waves results in amplification of the probe everywhere but at the heated location; conversely, amplification takes place only there for a frequency difference ν'_B.

5.2.2 Setup and performances

The block diagram of our setup is represented in figure 5-2. In comparison with the setup for integral measurements (figure 4-3), the light source is a first difference : a DFB diode @ 1555 nm replaces the YAG laser; the main advantage of this substitution lies in the availability of optical amplifiers (EDFA) for this range of wavelengths, what enables us to launch pump pulses with peak powers in the Watt range. We refer to the next section for the reasons that justify this increase in the pump power.

2. Or any other parameter with an impact on the BGS, most notably applied strain. However, we here carry on concentrating on temperature sensing.

The key element of the setup is still an electro-optical modulator. Its versatility allows it to shape both the signal waves and the pump pulse when the electrical signals schematized in figure 5-3 are applied to it.

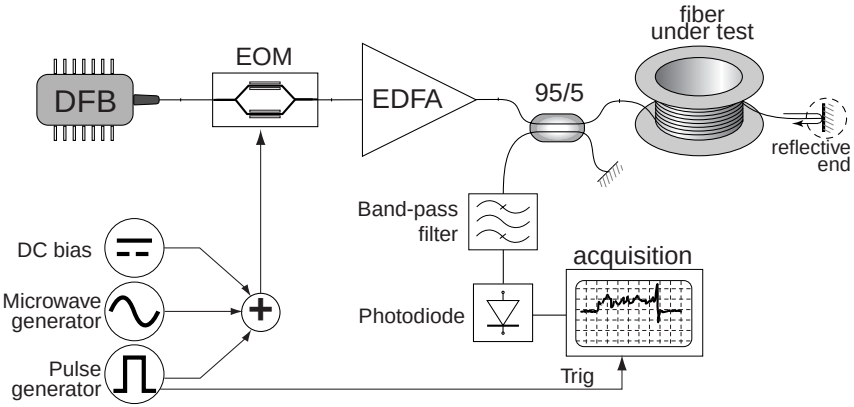

Figure 5-2. Simplified setup of the distributed Brillouin sensor.

The repetition rate of the pump pulses is low (typically a few kHz) and their duration short (typically 10 - 100 ns). Hence only the weak signal wave, always consisting in two symmetrical frequency components centered on the frequency of the unmodulated laser lightwave (figure 4-2b), propagates within the fiber most of the time. It has to be backward propagating (see figure 5-1); in the depicted configuration, this is simply ensured by a reflecting fiber end (either the natural reflection of about 4% at a plane silica-air interface, or some kind of mirror to increase this percentage). It would also be possible to use the second output of the 95/5 coupler by connecting it to the far end[1]. In accordance with the principle of operation outlined by figure 5-1, Brillouin amplification takes place when a pulse is launched, provided that the applied RF frequency falls within the BGS.

The anti-Stokes component has a detrimental effect on the contrast at the detection stage. Similarly, Rayleigh scattering of the pump pulses as well as the pulses themselves coming back after reflection at the end of the fiber have to be tossed aside before the optical-electrical transformation. We use an optical narrow bandpass filter - either a bulk Fabry-Pérot etalon, or an all-fiber Fabry-Pérot cavity or

1. At least in the laboratory. Depending on the application, only one fiber end may be accessible.

a unbalanced Mach-Zehnder interferometer [3] - to reject all frequencies but the amplified Stokes wave.

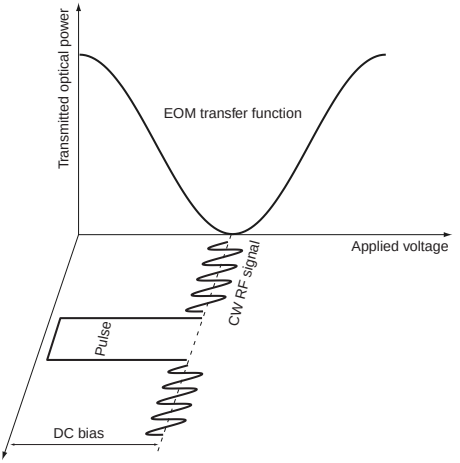

Figure 5-3. Driving electrical signals applied to the electro-optical modulator.

The measurements progress as follows :
- acquisition of spatial traces $g_B(\nu_k, z)$ for frequencies ν_k covering the BGS.
- at each position z_j, extraction of the parameters of the Lorentzian $g_B(\nu, z_j)$. The main parameter, in fact the only retrieved one in usual applications, is the central frequency of the curve, i.e. the Brillouin shift ν_B. Examples of 3D-representations of the surface $g_B(\nu, z)$ and end-product plots of $\nu_B(z)$ will be presented in the sections devoted to the applications.

In the course of the last few years, our Brillouin system underwent steady enhancement in terms of performances, reliability and ease-of-use. The company Omnisens S.A. has to be credited with the largest part of these improvements, since it tackled the somehow (intellectually...) unrewarding task of making a commercial instrument from our laboratory experiment. Thanks to their efforts, the system claims now the technical specifications summarized in table 5.1.

Measurement range	up to 25 km
Spatial resolution	1 m over 5 km 2 m over 10 km 5 m over 25 km
Temperature range	-270°C to 400°C
Temperature resolution	1°C
Sampling points	max 50'000 points
Acquisition time	2 min (typical)
Weight	< 20 kg
Dimensions	449 x 500 x 266 mm

Table 5.1. Technical specifications of the last generation of Brillouin measuring setup (DiTeSt fiber optics Brillouin analyzer, built by Omnisens SA)

5.2.3 Physical limitations to performances

In this section, we address the fundamental limitations of the traditional SBS analysis as a distributed sensing method when the spatial resolution is in the meter range. By doing so, we will prove that our experimental configuration reaches the best performances achievable for this kind of sensors.

Limitations due to spectrum broadening [18]

Let us remind the basic configuration of a distributed Brillouin sensor : a strong light pulse, hereafter called pump, is launched into the fiber. It crosses a weak CW lightwave, called signal or probe wave, that propagates in the backward direction. SBS occurs when pump and probe overlap, resulting in an amplification of the probe wave provided that the difference between the two frequencies lies within the Brillouin gain spectrum (BGS). This BGS shows a Lorentzian distribution centered on the Brillouin shift ν_B that is the quantity to determine. To obtain the BGS and thus determine ν_B, one simply measures the amplification of the Stokes wave while making a frequency scan. Let $g_B(\nu)$ be the gain spectrum; the net amplification of the signal wave after interaction with the pump pulse is given by

$$I_S = I_0 \exp[g_B(\nu) I_p L] \tag{5.1}$$

where the intensities are I_0 for the incident signal wave, I_S for the amplified signal wave and I_P for the pump, respectively. $L = \frac{1}{2} T v_g$ is the equivalent pump pulse length, with T the temporal width and v_g the group velocity of the pump light. Since the group velocity in silica is very close to $v_g \cong 2\times10^8$ m/s, we will use, as a rule of thumb, the correspondence 10 ns = 1 m. Fiber attenuation and polarization mixing efficiency are omitted here, because they are not relevant for the determination of the spatial resolution.

The spatial resolution for distributed measurements is directly related to the pulse length L. As shown in (5.1), the amplification of the Stokes waves exponentially decreases as L gets shorter. This could be compensated to a limited extent by increasing the detector sensitivity and by optimizing the data processing. A second possibility consists in increasing the pump intensity, so that the product $I_P L$ remains sufficiently high to obtain a good measurement contrast. This was the reason that led us to add an EDFA in our setup : it is able to provide pulses with peak powers up to a few Watts, contrary to the YAG laser of the initial 1319 nm setup, which has an upper boundary in the tens of mW range.

Nevertheless, fundamental limitations prevented us to increase the pump power as far as we could wish. One is the Raman threshold, that will be discussed later. But the most important one results from the pulsed nature of the pump wave, and that determines the ultimate resolution of the Brillouin sensor. In (5.1), it was assumed that the gain spectrum $g_B(\nu)$ does not depend on the length L of the pump pulse. This is no longer true for short pulses. The pulse narrowing induces a broadening of its spectrum, so that the effective BGS $\overline{g_B}(\nu)$ experienced by the signal wave is given by the convolution between the intrinsic $g_B(\nu)$ and the spectrum of the pump pulse. The subsequent broadening is similar to that caused by the finite linewidth of the light sources, despite the difference in the physical cause, and the same picture can represent both of them (see figure 4-4.) Assuming a perfectly rectangular pulse of duration T, the convolution yields the following expression :

$$\overline{g_B}(\nu) = \frac{g_B(\nu)}{\Delta\nu(\Delta\nu^2 + \nu'^2)}\left\{(\Delta\nu^2 - \nu'^2)\left(\Delta\nu + \frac{\exp(-\Delta\nu T)\cos(\nu' T) - 1}{T}\right) + 2\nu'\Delta\nu\left(\nu' - \frac{\exp(-\Delta\nu T)\sin(\nu' T)}{T}\right)\right\} \qquad (5.2)$$

where $\Delta\nu$ stands as usually for the half-width at half-maximum of the original Lorentzian and $\nu' = \nu - \nu_B$.

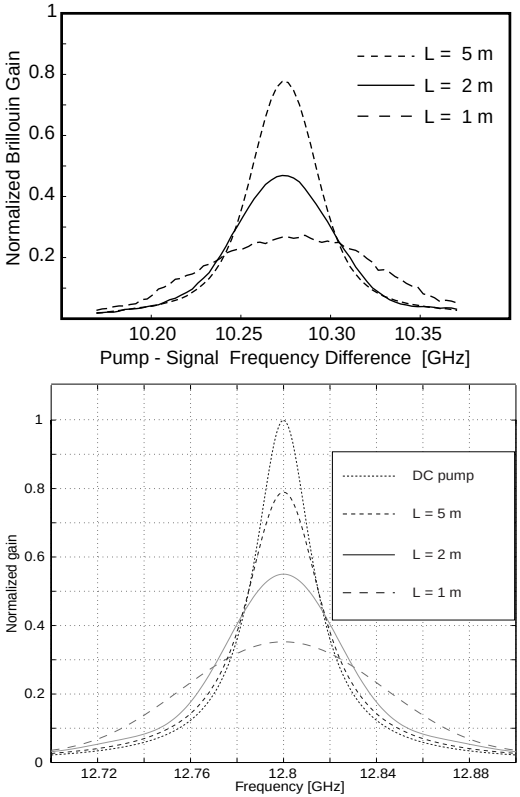

Figure 5-4. Measured (top) and calculated (bottom) effective Brillouin gain spectrum for different pulse widths. The curves are normalized with respect to the calculated gain for DC pump. Intrinsic half-linewidth : 15 MHz.

$\overline{g_B}(\nu)$ must replace the intrinsic Lorentzian spectrum $g_B(\nu)$ in (5.1) to calculate the actual amplification of the probe signal. Experimental evidence confirms the validity of our calculations, as can be inferred from the measured data of figure 5-4. They represent the effective BGS for three pulse widths. In total agreement with the curves calculated with (5.2), the spectra become broader for shorter pulses, resulting in a dramatic decrease of the peak gain, and of the mea-

sured signal. Moreover, this effect is detrimental for the frequency resolution of the measurements, the central frequency of such a spread distribution being determined with less accuracy. In figure 5-5, the flattening-out as well as the broadening of the BGS with decreasing pulse length are quantified.

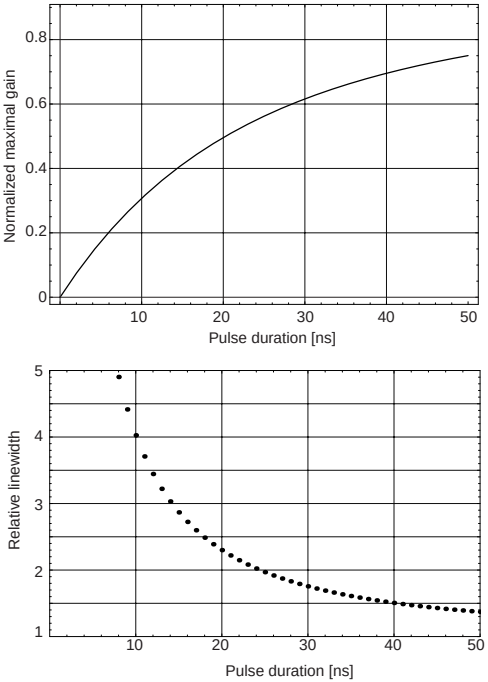

Figure 5-5. Maximal gain and linewidth as a function of the pulse duration. g_B = 1 and $\Delta\nu$ = 1 are the values for a DC pump.

In the temporal domain, the pulses are generally square-shaped, at least approximately (rise times cannot be strictly zero), and this form was assumed for the calculations shown so far. It could be interesting, as was recently suggested [19], to try other pulse shapes. It turns out that square pulses, because of their wide spectrum, have the worst shape as far as the broadening of BGS is concerned. For the same duration, triangular pulses are better, as are 'exponential' pulses (mathematical object consisting in an exponential rise followed without transition by an exponential decrease). The figure 5-6 shows this behavior which suggests that paying attention to this aspect of the measurement process could bring a non-negligible improvement to the signal-to-noise ratio.

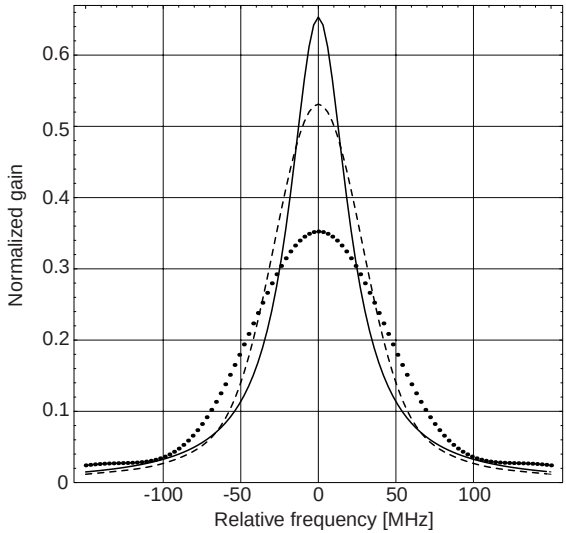

Figure 5-6. Calculated effective Brillouin gain spectrum for different pulse shapes : from top to bottom : exponential pulse, triangular pulse and square pulse. Characteristic time in each case : 10 ns. The full scale corresponds to a DC pump

It is possible to estimate the ultimate resolution of a distributed Brillouin sensor as a function of the fiber length : it is the minimal pulse length giving a sufficient amplification, say 2%, when the spreading of the gain spectrum and the effect of absorption are taken into account. With our system specifications, the calculation yields the figure of merit shown in figure 5-7. The most remarkable feature shown on this graph is the maintained resolution over a long distance : it remains below 3 meters over 50 km, as a consequence of the low loss at 1550 nm. On the other hand, the optimal resolution for very short fibers is slightly less than 1 m. The applications of this kind of sensors are thus definitely to be found in long range measurements with meter resolution and not when centimetric resolution is required.

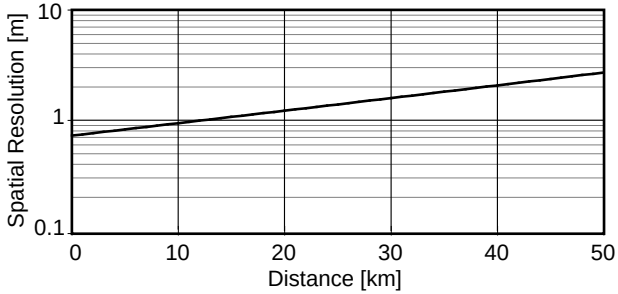

Figure 5-7. Spatial resolution leaving a sufficient amplification (2 %) vs distance along the fiber. Pump power : 6 W, attenuation : 0.22 dB/km and average linear Brillouin gain : $1 \cdot 10^{-11}$ W·m

The theoretical expectations for the best spatial resolution are fulfilled for short-range measurements. 80 cm resolution is effectively achieved by our systems for fiber lengths up to a few kilometers. On the other hand, the experimental values for the spatial resolution over long fiber spans do not yet reach their physical limits : current noise on the laser source, electronic noise at the detection stage and interferometric noise due to reflections of various origins along the optical path are hard to completely eliminate.

Limitations due to Raman scattering [20]

The Brillouin effect is the non-linear process showing the lowest power threshold; it has been however previously mentioned that an increase of the involved optical powers turns out to be necessary in order to achieve better performances in terms of spatial resolution and range.

In our pump-and-probe analyzer configuration, an EDFA is used to boost the pulses produced by a standard DFB laser diode at 1550 nm, giving a peak power in the range of a few Watts for pulses from 10 to 500 ns. Taking into account the very low silica absorption at this wavelength, such a high optical power should result in a metric resolution over a very long range. But it turns out that such ideal conditions are not practically fulfilled, as shown in figure 5-8. This figure shows the actual amplification of the probe signal through Brillouin interaction as a function of the position in a 25 km fiber. As it can be seen, the gain falls abruptly to zero at 10 km; after this position, varying between 10 and 20 km depending on the amount of pump power and the type of fiber, the measurement of the Bril-

louin frequency shift, and thus the determination of local temperature, are no longer possible. Besides, the initially square pump pulses undergo strong distorsions. Neither the linear absorption nor the pump depletion due to Brillouin scattering can explain this behavior.

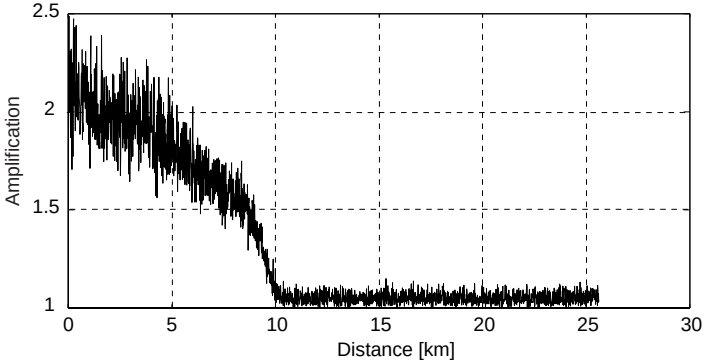

Figure 5-8. Amplification of the probe signal through Brillouin interaction as a function of distance, showing the pump depletion due to forward Raman scattering. The apparent noisy response in the initial section is actually due to birefringence induced changes in the states of polarization of the lightwaves.

A straightforward estimation would show that the combined effect of self-phase modulation and dispersion, though able to distort shorter pulses, is negligible for pulses equal to or longer than 10 ns, what leaves the Raman effect as unique possible cause. Raman scattering [21] has fundamental similarities with Brillouin scattering, both resulting from the interaction of light and phonons, but it shows distinct features. The most noticeable difference is the frequency shift experienced by the scattered light (13 THz for Raman, 11 GHz for Brillouin scattering), but equally important are the discrepancies in the cross section (two orders of magnitude smaller in the Raman case) and in the direction of scattered light (forward Raman scattering being possible while only backward Brillouin scattering is allowed in fibers). This last property is the key feature that makes it possible to reach the Raman threshold despite its high value : the initial pump pulse and the Raman-generated pulse being copropagative, they may interact over long distance, even the entire fiber length, unlike the case of Brillouin scattering where this interaction length is limited to the pump pulse width.

It has been shown [22] that the Raman power threshold is approximated by the expression

$$P_{Ra} \approx \frac{16A_{eff}}{g_R L_{eff}}, \tag{5.3}$$

where g_R is the Raman gain and the effective area and length are defined as in the case of Brillouin scattering. The Raman threshold is represented as the dashed curve in figure 5-9 for typical values at 1550 nm. The solid curves on the same graph show the required power for the measurement of the Brillouin amplification, depending on the pulse duration :

$$P_{Br} = \frac{\log(G)A_{eff}}{g_B L_p \exp(-\alpha z)} \tag{5.4}$$

Here g_B is the Brillouin gain, L_p the pulse length, and G the actual needed gain. G depends on the setup and is determined by the SNR at the detection. In this example, it has been set to 1.5 to be demonstrative. This value looks high at first glance, but is not far from reality for long-range measurement, mainly owing to the phase noise of the DFB laser source.

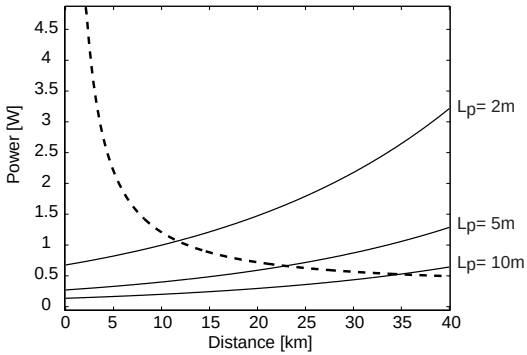

Figure 5-9. Raman threshold power (dashed curve) and minimal required power for Brillouin sensing for different pulse lengths (solid curves). The parameter G is 1.5. For a fixed pulse length, the useful part of the graph lies under the dashed curve and over the solid one.

The intersection of the dashed and solid curves corresponds to the maximal measurement range before pump depletion through Raman scattering takes place. The analytic expression of this distance, plotted in figure 5-10, is

$$z_{max} = -\frac{1}{\alpha}\log\left[\left(\frac{\alpha 16 g_B L_p}{\log(G) g_R} + 1\right)^{-1}\right]. \qquad (5.5)$$

For a fixed resolution, the only way to increase this range is to reduce the noise level so that a lower gain G is sufficient. For instance, a range of 50 km can be reached if the detection scheme is able to cope with a 2% (G=1.02) amplification.

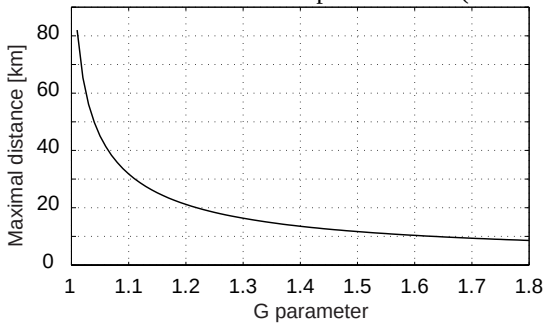

Figure 5-10. Maximal measurement range as a function of the parameter *G*.

So far, the pulsed nature of the pump and Raman lightwaves were not explicitly stated in the development. Actually, the expressions given above have been derived for the CW case; they are still valid, to a large extent, for pulses longer than 10 ns, as can be inferred from their good agreement with the measurements, but they fail to explain the pulse distortion resulting from Raman interaction. The additional quantity that has to be taken into account is the chromatic dispersion, which causes non-uniformities in the pulses evolution.

The propagation velocities of the pump and the Raman pulses differ from each other, owing to the large spectral distance between them (about 120 nm for a pump at 1550 nm). This difference actually ranges from 2 to 6 ns/km depending on the fiber. Since the relevant wavelengths lie in the anomalous dispersion regime, the pump pulse propagates faster than the Raman-generated wave signal. For very short pulses (L_p<5ns), this can lead to a prompt spatial separation of the pulses that quenches the Raman interaction between them. For longer pulses, such as those considered here, this walk-off is not entirely completed at the fiber end. But it results in pulse distortions, as shown in figure 5-11.

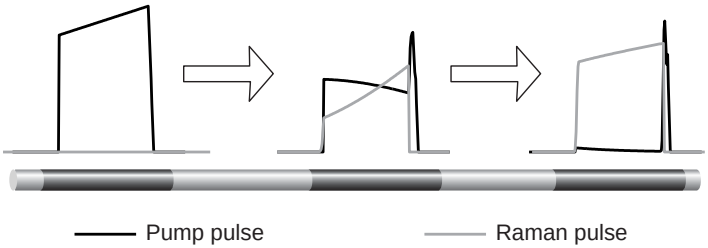

Figure 5-11. Simulated evolution of pump (black line) and Raman (grey line) pulses along a fiber, showing the effect of walk-off.

The leading edge of the pump pulse, being always ahead of the Raman pulse, undergoes only a negligible depletion due to spontaneous Raman scattering, while the rest of the pulse experiences the much more efficient stimulated Raman scattering made possible by the steady superposition of the two lightwaves. Consequently, the leading edge is the only part of the input pump pulse that remains unchanged if the fiber is long enough. The width of this unmodified part is related to both the difference in group velocities between the pump and Raman frequencies, and the intensity of the pump pulse, which sets the distance necessary to reach the Raman threshold. Eventually, the energy of the pump pulse is fully transferred to the Raman pulse, except in the narrow leading edge.

The figure 5-12 presents a demonstrative measurement of this walk-off effect. At the end of a 25 km fiber, the 100 ns pump pulse at 1550 nm has been fully depleted and its energy transferred to the 1670 nm Raman pulse, except the leading 5 ns. The probe wave does not coincide with this leading part of the pulse for a time long enough to build up and deplete the pump.

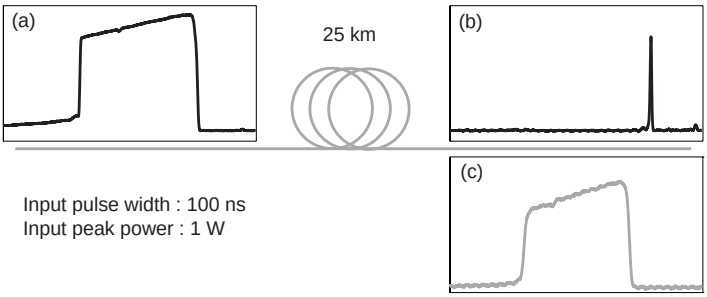

Figure 5-12. Measured time-domain waveforms of (a) an input pump pulse at 1550 nm, (b) the corresponding output pulse at the same wavelength after propagation along a 25 km fiber, and (c) the pulse generated by Raman scattering at 1670 nm. The vertical scales are arbitrary

One may think that advantage could be taken of this walk-off effect : all in all, it preserves short pulses from the depletion due to forward Raman scattering. From this point of view, fibers with high dispersion at the operating wavelength, like standard telecom fibers at 1550 nm, are more favorable than dispersion-shifted or other low-dispersion fibers

Unfortunately, in most cases, pulses short enough to avoid Raman scattering through walk-off effect turn out to be of no use in Brillouin sensing for reasons related to the physics of Brillouin scattering (the spectral broadening previously treated). The only solution is then to limit the optical pump (see figure 5-9). As a rough estimate, this must be kept below 0.5 W for a 40 km measurement range. Consequently, the resulting Brillouin amplification G will be low, what requires a properly designed detection stage and an efficient reflection suppression to avoid any interference.

5.3 Standard applications

In the last few years, many field demonstrations of distributed thermometry relying on Brillouin scattering in optical fibers have been carried out, and our group was involved in a non-negligible percentage of them. Our results were already presented in various conferences [23-26] (see also Facchini's thesis [3]), so there is no need to fully unfold them again here. We thus only briefly summarize in table 5.2 some information about the conditions of these measurements. Note also that these temperature measurements tests were supplemented by strain measurement tests.

Location	Type of installation	Cause of temperature variations
Versoix (GE)	installed underwater telecom fiber	seasonal variations of the water temperature on the bed of the lake of Geneva
Hauterive (FR)	fiber included in the insulating layer of a high-voltage distribution cable	possible anomalous heating due to defective power cable at 60 kV
Luzzone dam (TI)	fiber embedded in a large concrete slab	exothermic reaction during concrete setting
Chalet-à-Gobet (VD)	fiber attached to an ad-hoc scaffolding	daily variations of temperature at different heights in a forest
Pizzante (TI)	fiber laid on the gravel bed of a waste disposal site	exothermic reactions in the packed wastes

Table 5.2. Examples of application of Brillouin-based thermometry

Beside interesting results for each specific case, our field experiments gave us some general indications about the requirements of the measuring process itself. The most important one was certainly that measuring the Brillouin curves is just the easy part of the job[1]. What comes before (fiber installation) and after (data processing and shaping) is more intricate and, perhaps more annoyingly, strongly depends on the environment.

Apart from the occasional case where an already available telecom fiber has to be measured, the installation of the sensing fiber requires much care; the main

1. Of course, this is only true when you have a reliable instrument at your disposal.

weakness of distributed sensing, namely its total absence of redundancy[1], absolutely forbids any break of the fiber : without guided light, there is obviously no signal to detect and measure. Besides, the dependence on strain of the Brillouin shift makes it necessary to avoid, as far as possible, applying strain on any portion of the fiber if the temperature is the value of interest.

The often underestimated third part of the measuring process is equally important for the end-users of the system, that is the people who want to know the temperature. The Brillouin shift values have to be translated into temperature values; even in the linear region of the $\nu_B(T)$ curve, this implies a previous calibration of the fiber in laboratory. Moreover, the spatial coordinates of the fiber need also to be precisely known, so that any Brillouin gain curve can be assigned to its location. Spatial calibration, as well as user-friendly presentation of the measured *T(x)*, require a careful, case-specific work.

A section on practical applications would be somehow flimsy without any measured curve. Rather than presenting once more an old graph from the campaigns mentioned in table 5.2, we show in figure 5-13 a recent test of the last generation DiTeSt system of Omnisens SA that validates the spatial resolution limit claimed in table 5.1. There is a 18 MHz difference between the Brillouin shift of the fiber at ambient temperature and that of the fiber immersed in 5°C water. Events (i.e. cold sections) of lengths 10, 5 and 2 m are clearly resolved even for the greater pulse length (20 ns). For the 1 m and 50 cm events, we need to decrease the pulse length; otherwise the instrument is unable to give the true value of the Brillouin shift at these locations. Actually the 50 cm event is not perfectly measured, even with a 5 ns pulse. Notice also the expected increase in the noise of the measured values of ν_B with the decrease in the pulse duration. Everything considered, the value of 1 m for the spatial resolution over a short span of fiber is reasonable.

1. On the contrary, an array of point sensors, say thermocouples regularly spaced along a path, does not suffer from this weakness : in that case, a defective measuring point does not prevent the temperature to be measured elsewhere by the other sensors.

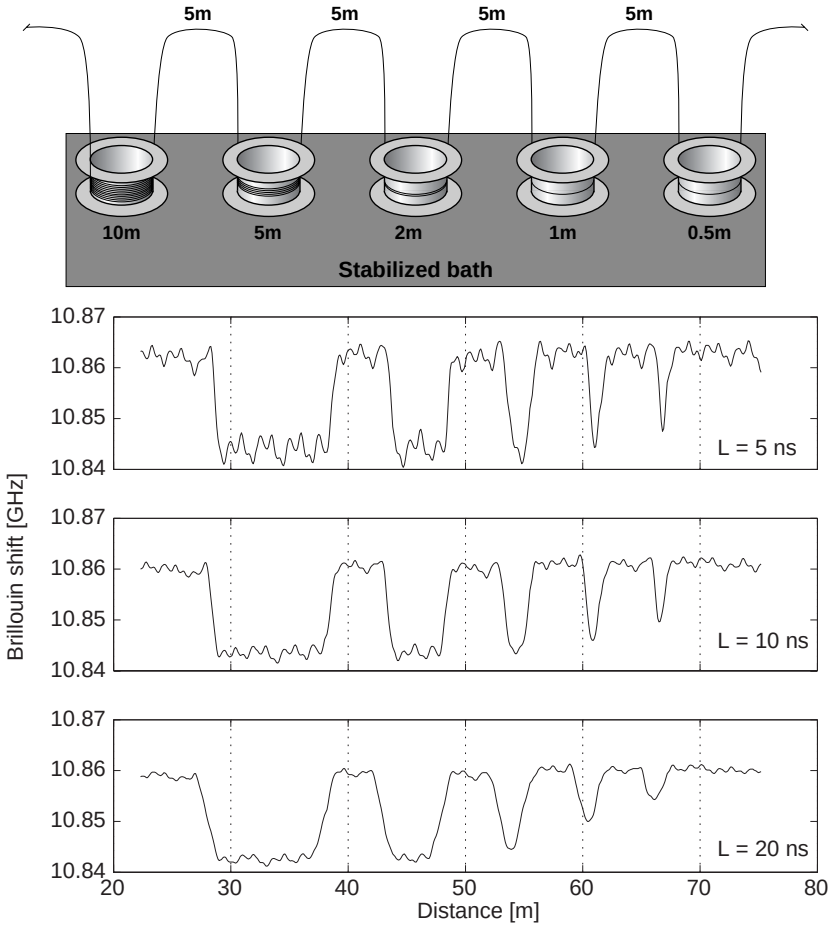

Figure 5-13. Measured Brillouin shift in a standard fiber for three different pulse lengths. The fiber consists in sections of various lengths immersed in cold water (5°C) separated by 5 m segments in the air (~20°C), with the indicated disposition (top).

5.4 Cryogenic applications

Cryogenic[1] distributed temperature sensing using Brillouin-based systems has seen much less real-size trials than sensing at ambient temperatures. Apart from our works [27, 28], we are not aware of other performed experiments.

Figure 5-14. One of the 1232 main superconducting dipoles of the future LHC, before the installation of the heat insulating layers. Mass : 23.8 t, length : 15 m.

Tests of distributed measurements were performed in real conditions by installing a fiber in a future magnet of the Large Hadron Collider at CERN, designed to operate at 1.9 K. The fiber was placed over the surface of the inner cold mass (figure 5-14) cooled by liquid helium, so that a direct monitoring of the actual temperature of the superconducting elements is achieved. Five coils of fibers are equally spaced along the cylinder-shaped magnet to improve the spatial accuracy of the measurement. Figure 5-15 shows (curves *a* to *d*) distributed measurements performed at successive times during the early stages of the vessel filling with liquid helium. Each horizontal section corresponds to one of the 20 m fiber coils. The temperature gradient along the vessel can be easily observed, the fill-

1. By 'cryogenic', we mean here the temperature range, below -50°C, that is unreachable without specialized techniques involving typically liquid nitrogen or liquid helium.

ing inlet being placed at the right side of the structure. It should be pointed out that the coldest temperature observed during this measurement is not below 50 K at this early stage of cooling down. The anomalous change of Brillouin shift is clearly highlighted on the final measurement (curve *e*) at a uniform temperature of 2 K and is observed as an upshifted Brillouin distribution.

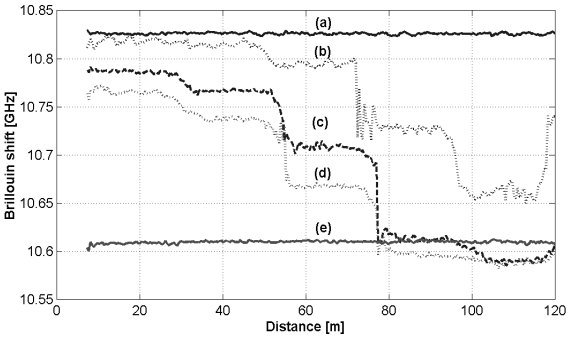

(a) magnet at room temperature (300 K)

(b) $t = t_0+120$ min

(c) $t = t_0+270$ min

(d) $t = t_0+370$ min

(e) cold magnet (2 K)

Figure 5-15. Brillouin shift variation during the cooling of a supraconducting magnet, measured @1555 nm.

This example shows that Brillouin temperature sensing can be used in cryogenics. Nevertheless, in comparison with the usual applications, two new problems arise, that are related to the shape of the $\nu_B(T)$ curve in this range (figure 4-12 or 4-15). The first is the ambiguity in the determination of the temperature from the measured acoustic velocity, distinct temperatures corresponding to identical velocities. The difficulty can be certainly removed by using also the linewidth information on the right part of the same figures, which does not need to be determined precisely for this purpose.

The second problem is the quasi-zero slope in the most interesting region between 1.5 and 5 K, due to the extremum around 5 K. Resorting to the linewidth is here of little interest, since its variation is also weak. Actually the problem is not as severe as expected at first glance, since the linewidth narrowing, quite evident in figure 4-13, results in a more precise determination of the centre of the Brillouin gain spectrum. A rough estimation shows that an accuracy of the order of 0.1 K can be achieved in the 1-10 K range. But the 10-fold decrease in the linewidth requires consequently longer pump pulses, so that the spectrum of the pulses remains narrower than the intrinsic Brillouin spectrum. This results in a

lower spatial resolution, that has to be compensated by a special fiber installation, such as the loops used in this case.

Unfortunately, we encountered many practical difficulties that now prevent us to present more detailed measurements about the LHC magnets. The stringent requirements for the building and the testing of the magnets were hardly reconcilable with our own needs, resulting ultimately in broken, unusable fibers. For a second example of cryogenic measurement, we thus have to resort to a more 'experiment-friendly' environment, namely the helium or nitrogen cryostat[1] we had already used for the acquisition of the data presented in the chapter 4.

The elements that fit into the cryostat are four copper plates, on which fibers can be laid. The natural temperature gradient occurring in the gas on top of the liquid helium or nitrogen bath, supplemented by heating resistances attached to the plates, takes care for the temperature variations we intend to detect. For this test, we take 90 m of fiber F1 (standard, polyimide-coated) and lay it on the upper plate. We also take 80 m of fiber F2 (standard, acrylate-coated), shared out into four coils we lay on each plate. Figure 5-16 shows the measured BGS of the concatenation of these two fibers.

In this example, the temperature decreases from the top to the bottom plate. Its values are 190 K, 174 K and 159 K on the first, second and fourth plates respectively (the thermistance on the third one was out of order). The perfect homogeneity of the fiber F1 is clearly shown by the 3D Brillouin curves and results in a constant shift. The two isolated peaks merely correspond to the short sections of fiber that lie outside the cryostat, that is at ambient temperature. As for the fiber F2, four steps are clearly distinguishable, mirroring the four different plate temperatures. Since we are here still in the region where the Brillouin shift increases with temperature, albeit non-linearly, figure 5-16 shows that the coldest part of the fiber is its first section.

1. In Cryolab, a centralized cryogenic facility of CERN.

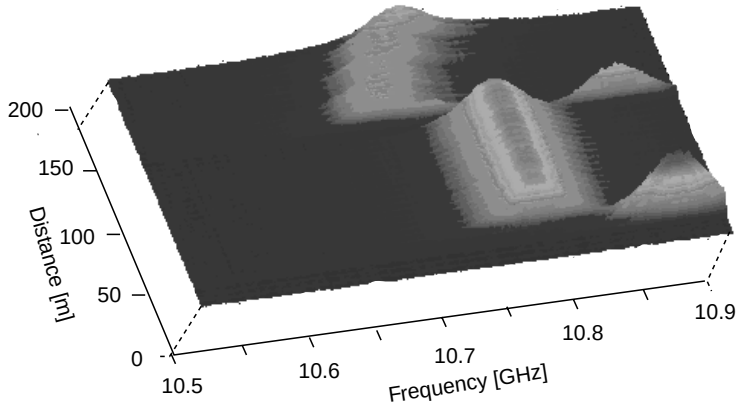

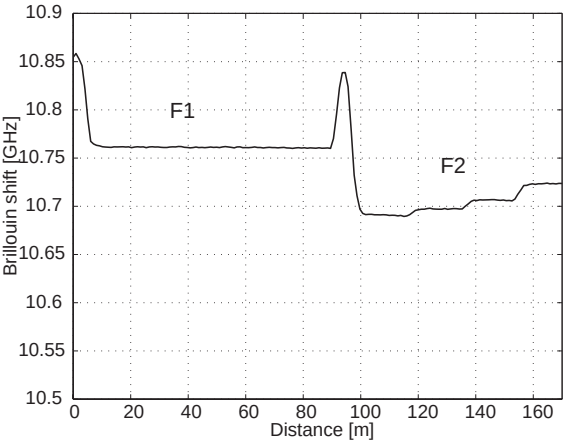

Figure 5-16. Raw measured surface $g_B(\nu, z)$ and processed Brillouin trace $\nu_B(z)$ for two concatenated fibers in cryogenic environment. See text for the description of the installation.

Our second example, with helium cooling, is plotted in figure 5-17. The same two concatenated fibers are measured while they are fully immersed in liquid helium and thus at uniform 4.2 K temperature. Also shown is a section of the lead fiber that connected the fibers under test to the instrument; the temperature of this section is about 20°C. Gain curves are obviously narrower at 4 K. Using the line-width information, it would be possible to discriminate between 4 K and the temperature in the 100 K range (see figure 4-12) for which the Brillouin central frequency is the same.

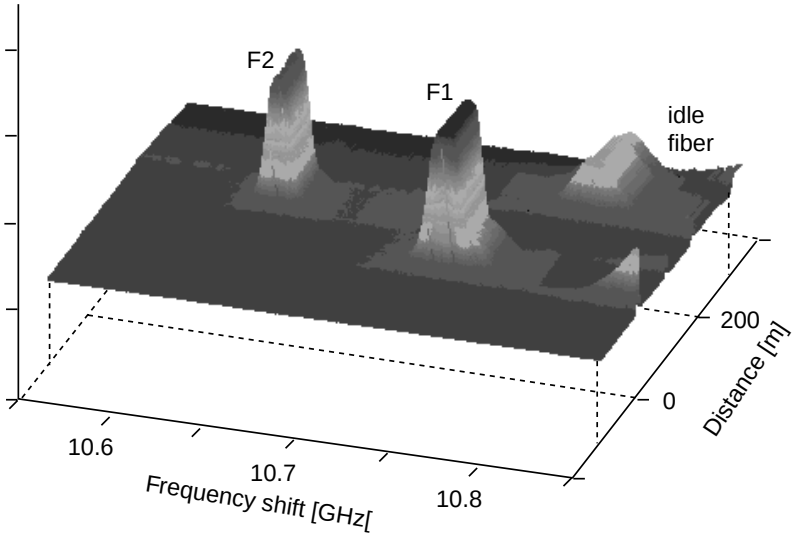

Figure 5-17. Raw measured surface $g_B(\nu, z)$ for the same two concatenated fibers as in figure 5-16 at uniform liquid helium temperature. The idle fiber shown for comparison lies outside the cryostat. Note the difference in the amplitude of the gain.

5.5 Advanced setups

Further enhancements of the LASBI (or now rather DiTeSt) measuring setup are now a matter for industrial development and optimization rather than for research. However, little explored pathways do still remain in the land of Brillouin scattering in fibers. We present here proofs of feasibility for two of the possible research directions, without going into too intricate details.

5.5.1 Injection-locking based setup

EOMs are very clever devices and can be rightly considered a workhorse of the optical telecoms. But they suffer from at least two drawbacks : first they remain rather expensive; and, what is more detrimental for our application, they paradoxically tend to become less efficient : tailored to the standardized requirements of the telecom industry, they do no longer exhibit as good extinction ratios as a

few years ago, so that the optical fundamental carrier is insufficiently attenuated in the spectrum of figure 4-2. It is thus worth exploring an alternative approach that would be able to provide the stable, while tunable, frequency difference between two lightwaves that is necessary for SBS generation.

Injection-locking has undoubtedly this potential. It is based on the observation that, when coherent light of one laser is coupled into the cavity of another laser, the latter may leave its own emission frequency and shift to the frequency of the injected lightwave. The two lasers are self-explanatorily called master and slave, respectively. In order to get this locking, two conditions must be fulfilled :

- the influence has to be unidirectional; proper isolation must prevent the light from the slave to be injected in the master's cavity.

- the detuning of the two natural frequencies of the cavities must be small; actually, there is only a limited frequency region around the free-running frequency of the slave, called the locking range, where locking is possible, provided additionally that enough power from the master is available. A lot of work has been devoted to the study of the locking conditions, the stability and quality of the slave's output lightwaves since the 1980's. We refer to Troger [29, 30] for a detailed presentation of these topics in the case of DFB diodes coupled by optical fiber links.

The figure 5-18 shows how we can take advantage of injection-locking to make distributed measurements of Brillouin gain spectra in fibers. It is based on two identical DFB @1555 nm, with a few mW output power. The light of the master is separated by an unbalanced coupler; the smaller part is directly launched into the fiber under test, where it will act as the probe wave for SBS. The greater percentage of power is injected into the cavity of the second laser to ensure locking. The slave is directly current-modulated by a RF generator at the frequencies of interest for Brillouin experiments (typically ν_B~10.8 GHz for standard fibers). Its spectrum, as can be seen in figure 5-19 consists in its natural frequency, a few GHz apart from the master's frequency and two modulation sidebands. As long as there is no locking, (upper part of figure 5-19) the respective frequencies of the lasers can drift without control, and stimulated Brillouin amplification is impossible. If we change briefly the supply current of the slave laser with the pulse generator, we may manage to shift its natural frequency by precisely the amount that puts the lower sideband (always at a distance of ν_B) within the lock-

ing-range. Locking takes place quasi-instantaneously (with respect to the duration of the applied pulses), which results in the central frequency of the slave being at the appropriate value to act as the pump for SBS (lower part offigure 5-19).

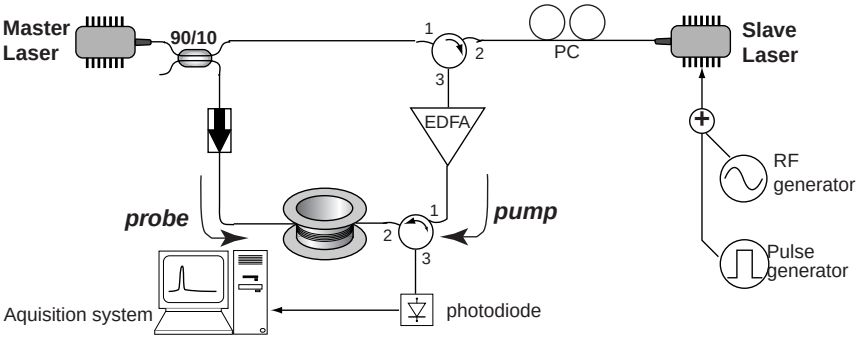

Figure 5-18. Experimental setup of an injection-locking based distributed Brillouin

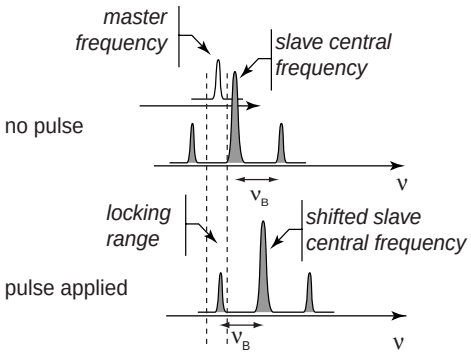

Figure 5-19. Spectra of the two lasers. In *a*) there is no locking. This is the normal situation. In *b*) a current pulse is applied to the slave laser, what slightly shifts its frequency, so that its sideband falls within the locking range of the master. The master and the slave are then able to interact through Brillouin effect.

To complete the setup, we still need an EDFA to boost the pump up to 60 mW, two circulators, an optical isolator and the detection stage. There is no need to insert a band-pass filter before the detection as in the standard setup (figure 5-2), since the pump, that is here the modulated wave, does not hit the detector.

Figure 5-20 shows an example of BGS measurement with the above described setup. It was carried out with 30 ns pulses, resulting in a nominal spatial resolution of 3 m. Nevertheless, the heated section of only 2 m is perfectly detected. Note incidentally the quality of the gain curves, at least comparable to those obtained with the last generation of BOTDA, but with a pulse power reaching only 60 mW, approximately one percent of that used in these other systems.

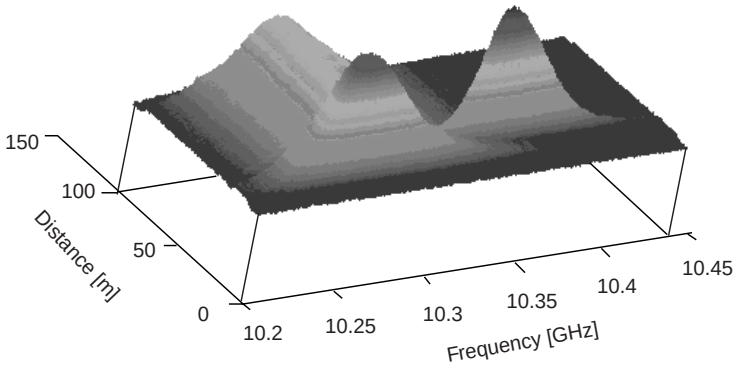

Figure 5-20. Example of measured Brillouin gain spectra as a function of distance with an injection-locking setup. Fiber length : ~100 m; hot point length : 2 m; pulse duration : 30 ns

5.5.2 Correlation-based technique

In the conventional, OTDR-like technique, distributed information about the temperature is obtained by launching a pulsed light and measuring the strength of the back-scattered light as a function of arrival time of the light. The spatial resolution in the pulse-based technique is proportional to the pulsewidth. If the pulse width is shorter than the acoustic damping time (~30 ns) in the fiber, the effectively measured Brillouin gain spectrum is flattened (figure 5-4). This phenomenon is described in section 5.2.3 and leads to a practical limitation in the spatial resolution of about 1 m.

To circumvent this limitation, Hotate proposed a few years ago [31-33] an elegant alternative technique in which the correlation between two continuous lightwaves is controlled so as to generate Brillouin scattering locally along the fiber, thus avoiding the use of a pulsed lightwave. Frequency modulation (FM) is the

technique that makes it possible to reach, according to recent reports [34, 35], centimetric spatial resolution.

To understand how that can work, we first remind that stimulated Brillouin scattering is strongly dependent on the correlation of the interacting lightwaves. Its efficiency deteriorates as soon as something, may it be polarization, phase or frequency mismatch, decreases this correlation. Basically, Hotate's trick is to artificially decrease the correlation in the fiber everywhere but at the precise location where Brillouin gain is to be measured.
So let us assume that we launch two identically frequency-modulated waves into the opposite ends of a fiber of length L. For given time t and position z, the fields are then

$$\begin{aligned} E_1 &= E_0 \exp[i(\omega_0 + \Delta f \cos(f_m t_1))t - kz] \\ E_2 &= E_0 \exp[i(\omega_0 + \Delta f \cos(f_m t_2))t + kz] \end{aligned} . \tag{5.6}$$

Δf is the maximal excursion of the instantaneous frequency, also called the modulation depth, while f_m is the modulation frequency. The times t_1 and t_2 depend on the position z and on the velocity of light as

$$\begin{aligned} t_1 &= t - z/v_g \\ t_2 &= t - (L - z)/v_g \end{aligned} \tag{5.7}$$

We now look at the instantaneous frequency difference between the two lightwaves Df_{inst}. It can be rewritten as

$$Df_{inst} = \Delta f(\cos(f_m t_1) - \cos(f_m t_2)) = -2\Delta f \sin\left(f_m \frac{t_1 - t_2}{2}\right) \sin\left(f_m \frac{t_1 + t_2}{2}\right) \tag{5.8}$$

Only the difference term depends on z. It is straightforward to check that there are values of z for which the frequency difference is null at any time t. These are given by

$$z = \frac{v_g}{2f_m} \equiv z_{max} \tag{5.9}$$

We plot in figure 5-21 $Df_{inst}(z)$. Each solid curve corresponds to a different value of the time t. We find, as expected, positions z where the frequency difference always cancels. At these locations, the correlation between the contrapropagative lightwaves is perfect, while it decreases quickly elsewhere. Besides, as the curves

for two values of f_m are represented, we can see that changing f_m results in a shift in the positions z_{max} of the correlation peaks. A spatial scan is thus possible without pulsed light.

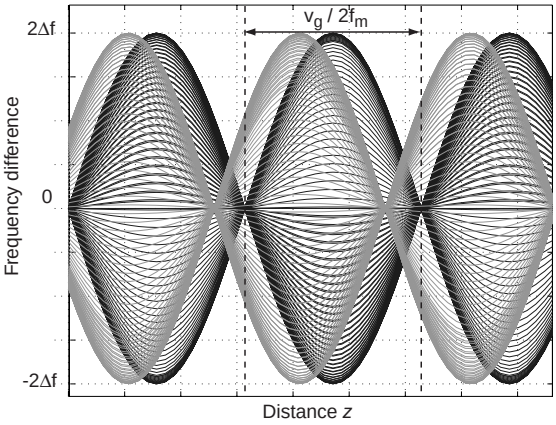

Figure 5-21. Instantaneous frequency difference between two contrapropagating FM lightwaves plotted at different times and for two modulation frequencies. Changing f_m results in a spatial shift of the high-correlation regions.

Qualitatively, it is obvious that the spectrum of the beating, while reduced to a Dirac distribution at the points z_{max}, becomes broader elsewhere. The measured BGS being the convolution of the intrinsic BGS and the spectrum of the probing lightwaves[1], we thus yield :

- at z_{max}, the intrinsic Brillouin gain curve, with the same width we would have measured with DC pump and probe over a very long span
- elsewhere, a wide, very low gain curve. The problem with this spurious contribution is that it piles up as the probe travels along the fiber and may reduce the contrast of the useful signal generated at the correlation peak.

Standard (using EOM) or injection-locking based pulsed Brillouin setup may be readily adapted to correlation-based measurements. We present in figure 5-22

1. We mean here the pump as well as the probe and include in general the intrinsic linewidths of each wave and their correlation spectrum. For a BOTDA setup, the broadening due to the pulsed nature of the pump replaces the latter.

our version of this kind of systems, based on the injection-locking setup of the figure 5-18.

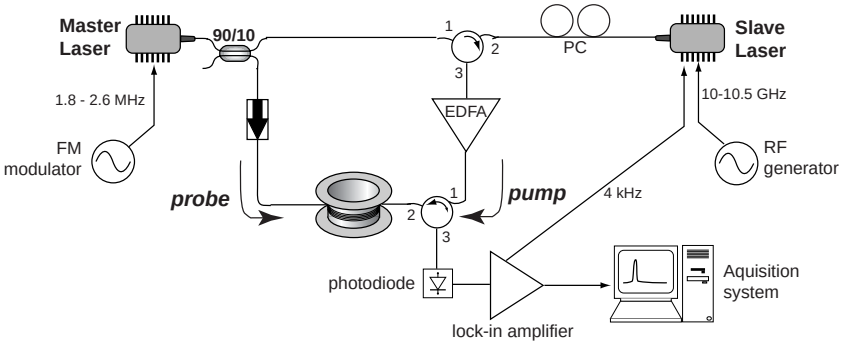

Figure 5-22. Experimental setup of a correlation-based Brillouin sensing experiment, also using locking-injection.

The FM modulation is applied to the master laser, that generates again the probe wave. Its spectrum is shown in figure 5-23; it has the typical horn-shaped overall look of broadband FM spectra. Its linewidth depends on the modulation depth Δf. As for the slave laser, it undergoes always the RF modulation that creates the sidebands at the Brillouin frequency from its central frequency. Contrary to the case described in section 5.5.1, the slave's lower sideband is now permanently injection-locked by the master, resulting in its spectrum mirroring that of the master.

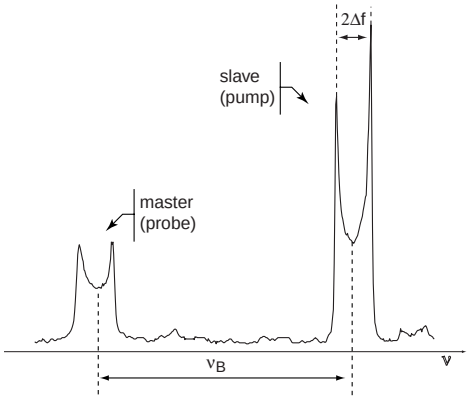

Figure 5-23. Spectra of the pump and probe waves in the setup represented in figure 5-22. The distance between the two peaks of each line is directly given by the modulation depth Δf that has values in the hundreds of MHz. Injection-locking occurs as a result of the same relative disposition of frequencies as in figure 5-18.

To acquire a full set of data $g_B(\nu, z)$, we have to perform a double scan; as before, the scan in frequency is obtained by modifying the RF frequency applied to the slave over the frequency range of interest (here around 10.8 GHz since the DFB emit at 1555 nm). The spatial scan is the result of sweeping of the FM frequency applied to the master, typically about 2 MHz. Actually, going from 1800 to 2600 kHz shifts here the position of the correlation peaks by 10 m[1].

The spatial resolution of measurements is [33, 36] :

$$\Delta z = \frac{v_g \Delta \nu}{2\pi f_m \Delta f}. \tag{5.10}$$

It depends on the intrinsic Brillouin linewidth; more important though is the fact that it is enhanced by increasing either the modulation depth or the modulation frequency.

Increasing the modulation frequency is quite easy, due to the large bandwidth of the available DFBs, but it has a major drawback : according to (5.9), the distance between two correlation peak decreases also as $1/f_m$. Since we absolutely need only one peak within the fiber, this reduces the maximal measurement range. Increasing the modulation depth brings a different kind of problems : the intensity modulation of the laser that is coupled to the FM modulation can no longer be neglected and complicates the analysis. As an order of magnitude, the best reported resolution to date is 1 cm [36]; in this case, the maximal length of the fiber is about 3 m.

Our group is still at the preliminary phase of research in that direction, so that we can not claim such an high spatial resolution. Figure 5-24 shows an early example of our results (courtesy of S. Le Floch). The fiber is the same that was measured in figure 5-20, with a 2 m heated section. The heated zone is detected indeed, but the Brillouin gain curves are much larger than was expected, probably as a result of the low but constant and occurring over longer distances amplification outside the correlation peaks. Clearly, much work is still needed.

1. We choose the modulation frequency and, if necessary, add idle fiber segments, so that only one correlation peak falls within the fiber under test. This is mandatory; otherwise, the signal detected would be the result of ‘multi-stage’ Brillouin amplifications, with possibly different BGS characteristics, taking place at each correlation peak.

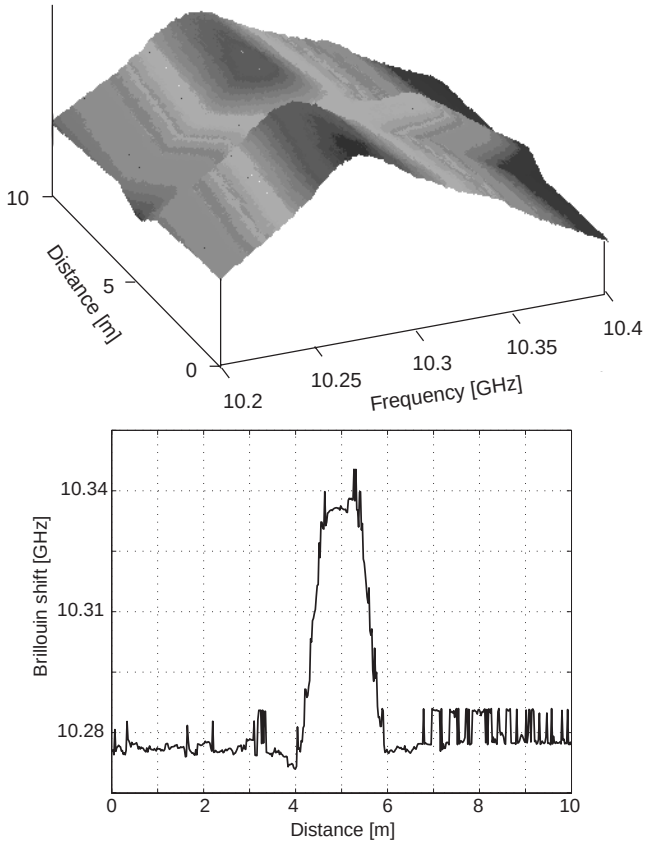

Figure 5-24. Raw measured surface $g_B(\nu, z)$ obtained with the setup of figure 5-22 (top) and corresponding Brillouin shift as a function of distance (bottom).

References

[1] *J.P. Dakin ed*
The distributed fibre optic sensing handbook
Springer, Berlin (1990).

[2] *J.P. Dakin, B. Culshaw ed*s
Optical fiber sensors. Vol. 4 : applications, analysis, and future trends
Artech House, Boston (1997).

[3] *M. Facchini*
Distributed optical fiber sensors based on Brillouin scattering
Ph.D. Thesis EPFL, Lausanne (2001).

[4] *M. Facchini, L. Thévenaz, A. Fellay, P.A. Robert*
Tensile tests on optical fibre cables using distributed Brillouin analysis
Proc. of the 5th Optical Fibre Measurement Conference, Nantes, France, p. 106-109 (1999).

[5] *M. Niklès, L. Thévenaz, A. Fellay, M. Facchini, P. Salina, P.A. Robert*
A novel surveillance system for installed fiber optics cables using stimulated Brillouin interaction
Proc. of the 46th International Wire and Cable Symposium, Philadelphia, p. 658-664 (1997).

[6] *M.K. Barnoski, S.M. Jensen*
Fiber waveguides : a novel technique for investigating attenuation characteristics
Appl. Opt., **15**, p. 2112-2115 (1976).

[7] *M.K. Barnoski, M.D. Rourke, S.M. Jensen, R.T. Melville*
Optical time domain reflectometer
Appl. Opt., **16**(9), p. 2375-2379 (1977).

[8] *E. Brinkmeyer*
Backscattering in single-mode fibres
Electron. Lett., **16**(9), p. 329-330 (1980).

[9] *E. Brinkmeyer*
Analysis of the backscattering method for single-mode optical fibers
J. Opt. Soc. Am., **70**(8), p. 1010-1012 (1980).

[10] *A.H. Hartog, M.P. Gold*
On the theory of backscattering in single-mode optical fibers
J. Lightwave Technol., **2**(2), p. 76-82 (1984).

[11] *J.P. Dakin, D.J. Pratt, G.W. Bibby, J.N. Ross*
Distributed optical fiber Raman temperature sensor using a semiconductor light-source and detector
Electron. Lett., **21**(13), p. 569-570 (1985).

[12] *J.P. Dakin*
Temperature measurement using intrinsic optical fibre sensors
in *The distributed fibre optic sensing handbook*, J.P. Dakin, Editor, Springer, Berlin (1990).

[13] *K. Shimizu, T. Horiguchi, Y. Koyamada, T. Kurashima*
Coherent self-heterodyne Brillouin OTDR for measurement of Brillouin frequency shift distribution in optical fibres
J. Lightwave Technol., **12**(5), p. 730-736 (1994).

[14] *T. Horiguchi, M. Tateda*
BOTDA - Nondestructive measurement of single-mode optical fiber attenuation characteristics using Brillouin interaction - theory
J. Lightwave Technol., **7**(8), p. 1170-1176 (1989).

[15] *T. Horiguchi, T. Kurashima, M. Tateda*
A technique to measure distributed strain in optical fibers
IEEE Photon. Technol. Lett., **2**(5), p. 352-354 (1990).

[16] *T. Horiguchi, K. Shimizu, T. Kurashima, M. Tateda, Y. Koyamada*
Developement of a distributed sensing technique using Brillouin scattering
J. Lightwave Technol., **13**(7), p. 1296-1302 (1995).

[17] *M. Niklès, L. Thévenaz, P.A. Robert*
Simple distributed fiber sensor based on Brillouin gain spectrum analysis
Opt. Lett., **21**(10), p. 758-760 (1996).

[18] *A. Fellay, L. Thévenaz, M. Facchini, M. Niklès, P.A. Robert*
Distributed sensing using stimulated Brillouin scattering : toward ultimate resolution
Proc. of the 12th Conference on Optical Fiber Sensors, Williamsburg Virginia, p. 324-327 (1997).

[19] *H. Naruse, M. Tateda*
Optimum temporal pulse shape of launched light for optical time domain reflectometry type sensors using Brillouin backscattering
Opt. Rev., **8**(2), p. 126-132 (2001).

[20] *A. Fellay, L. Thévenaz, M. Facchini, P.A. Robert*
Limitation of Brillouin time-domain analysis by Raman scattering
Proc. of the 5th Optical Fibre Measurement Conference, Nantes, France, p. 110-113 (1999).

[21] *G.P. Agrawal*
Nonlinear fiber optics
2nd ed. Academic Press, San Diego (1995).

[22] *R.G. Smith*
Optical power handling capacity of low loss optical fibers as determined by stimulated Raman and Brillouin scattering
Appl. Opt., **11**(11), p. 2489-2494 (1972).

[23] *M. Niklès*
La diffusion Brillouin dans les fibres optiques : étude et application aux capteurs distribués
Ph.D. Thesis EPFL, Lausanne (1997).

[24] *L. Thévenaz, M. Niklès, A. Fellay, M. Facchini, P.A. Robert*
Truly distributed strain and temperature sensing using embedded optical fibers
Proc. of the SPIE International Symposium on Smart Structures and Materials, San Diego, p. 301-314 (1998).

[25] *L. Thévenaz, M. Niklès, A. Fellay, M. Facchini, P.A. Robert*
Applications of distributed Brillouin fibre sensing
Proc. of the SPIE International Conference on Applied Optical Metrology, Balatonfüred, Hungary, p. 374-381 (1998).

[26] *L. Thévenaz, M. Facchini, A. Fellay, P.A. Robert, D. Inaudi, B. Dardel*
Monitoring of large structures using distributed Brillouin fibre sensing
Proc. of the 13th Conference on Optical Fiber Sensors, Kyongju, Korea, p. 345-348 (1999).

[27] *A. Fellay, L. Thévenaz, J. Garcia Perez, W. Scandale, M. Facchini, P.A. Robert*
Brillouin-based temperature sensing in optical fibers down to 1 K
Proc. of the 15th Conference on Optical Fiber Sensors, Portland, Oregon, p. 301-304 (2002).

[28] *A. Fellay, S. Le Floch, M. Facchini, L. Thévenaz, W. Scandale, P.A. Robert*
Brillouin gain curve measurements in fibers at cryogenic temperatures (3 K-140 K)
Proc. of the 6th Optical Fibre Measurement Conference, Cambridge UK, p. 55-58 (2001).

[29] *J. Troger*
Injection locking in semiconductor lasers
Ph.D. Thesis EPFL, Lausanne (1999).

[30] *J. Troger, P.-A. Nicati, L. Thévenaz, P.A. Robert*
Novel measurement scheme for injection-locking experiments
IEEE J. Quantum Electron., **35**(1), p. 32-38 (1999).

[31] *K. Hotate, T. Hasegawa*
Measurement of Brillouin gain spectrum distribution along an optical fiber with a high spatial resolution using a novel correlation-based technique - Demonstration of 45 cm resolution
Proc. of the 13th Conference on Optical Fiber Sensors, Kyungju, Korea, p. 337-340 (1999).

[32] *K. Hotate, T. Hasegawa*
Measurement of Brillouin gain spectrum distribution along an optical fiber with a high spatial resolution using a correlation-based technique - Proposal, experiment and simulation
IEICE Trans. Electron., **E83 C**(3), p. 405-411 (2000).

[33] *K. Hotate, T. Hasegawa*
A correlation-based continuous wave technique for measuring Brillouin gain spectrum distribution along an optical fiber with centimeter-order spatial resolution
Proc. of the 14th Conference on Optical Fiber Sensors, Venice, Italy, p. 651-661 (2001).

[34] *K. Hotate, M. Tanaka*
Distributed fiber Brillouin strain sensing with 1-cm spatial resolution by correlation-based continuous-wave technique
IEEE Photon. Technol. Lett., **14**(2), p. 179-181 (2002).

[35] *K. Hotate, M. Tanaka*
Application of correlation-based continuous-wave technique for fiber Brillouin sensing to measurement of strain distribution on a small size material
IEEE Photon. Technol. Lett., **14**(5), p. 675-677 (2002).

[36] *K. Hotate*
Recent progress in Brillouin based fiber sensor technology - Correlation-based continous-wave technique
Proc. of the 15th Conference on Optical Fiber Sensors, Portland, Oregon, p. 297-300 (2002).

Conclusion

This thesis deals with the temperature-induced variations of the characteristics of Brillouin scattering in optical fibers, from their causes deeply rooted in the disordered nature of amorphous silica to their use as a distributed sensing mechanism. In particular, we highlight the behavior at high (up to permanent structural damage to the fiber) and very low temperatures (down to 1 K). The linear variation of Brillouin shift that is a typical feature of Brillouin scattering around ambient temperature is no longer observed in both cases, in accordance with measurements carried out on bulk silica samples.

First intended as exploratory feasibility tests for the application of Brillouin sensing to cryogenic conditions, our experiments turned to systematic investigation of the Brillouin gain curves parameters in the fiber. This change in the course of measurements was triggered by the encouraging results of the first experiments, but was unfortunately not always accompanied by the necessary increase in precision and care, resulting in medium quality data. Actually, thanks to the acquired experience and the mistakes we did, we would be now in a far better position to tackle these measurements; proper calibration of the optical powers would be the first requirement, allowing us to measure also the absolute value of Brillouin gain. A quantitative analysis of the effect of Ge dopant would be possible too, provided we know its exact concentration profile in the fiber.

In spite of the above mentioned restrictions, our measurements show that Brillouin-based sensing is definitely good for thermometry at every temperature as long as fiber integrity is preserved, even if some complications may arise outside the linear region. Its known advantages in usual applications are retained in cryogenics : it is cost-effective, at least for a large number of measuring points, and enables remote sensing. Besides, the small size of the fibers minimizes the thermal bridges, and, contrary to the traditional point sensors who require individual calibration, a single calibration procedure suffices for a whole fiber.

Nevertheless, at the end of this work, we still face two problems of different nature :
- The first is conceptual : even if the knowledge of the exact mechanisms that cause the variations of sound velocity and sound attenuation in silica is not required to build sensors, it is intellectually frustrating not to understand them.

- The second may seem more superficial, but leads in practice to the greatest difficulties. It was mentioned for the standard applications but becomes still more acute when the environment gets harsher for the fiber. Simply stated, it is the problem of the installation. Numerous cases of broken fibers incite us to stress this aspect : even if fibers exhibit appreciable mechanical resistance, their integration as sensing elements always requires thoughtful design and great care.

Future of Brillouin sensing

'Traditional' Brillouin-based sensing devices seem to have a good chance of finding a commercial niche for applications where a spatial resolution of 1 meter and a temperature resolution of 1°C are required over a few kilometers (up to 30, maybe 50 km). As they will never be cheap instruments, their market will probably keep limited to the monitoring of large, expensive facilities like dams, bridges, tunnels or pipe-line, where their cost remains marginal. The extension of the temperature measurement range toward higher or lower temperature may add a few opportunities to this basis, like the monitoring of pipes in centralized heating installations at the town scale, or of large particle accelerators.

As for correlation-based Brillouin sensing, it is still not clear whether its performances, effective to date or theoretically possible (centimeter or even millimeter resolution over a few meters), meet a demand. What is clear however is that the basic idea behind this method is brilliant and that the concept deserves further work. Unforeseen applications may arise at any time; after all, there were 60 years between the prediction of the Brillouin effect and the first Brillouin distributed sensor.

Annex 1

Short biographical notice on Léon Brillouin (1889-1969)

The name of Brillouin is familiar to physicists in various fields - apart from the optical effect we have abundantly dealt with in this work, it appears in quantum perturbative methods, in information theory and above all in solid-state physics, where the Brillouin zones are one of the most used concepts. In spite of this widespread presence in the technical literature, the man behind the name is an unknown person to almost everybody[1]. My feeling is that I owe him a few lines of presentation, after years of blind use of his name. The pieces of information gathered hereunder are extracted from his only available, and luckily enough excellent biography, written by Rémy Mosseri [1].

Léon Brillouin was born on August, 7th 1889 in the suburbs of Paris, in what can be adequately described as a scientific dynasty. His father, Marcel Brillouin (1854-1948), was himself a renowned physicist, professor at the *Collège de France*, as his father-in-law Eleuthère Mascart (1837-1908) was before him. This place made them real leaders in the French physics of the time, and as such they met regularly people like Kelvin, Helmholtz, Langevin, Lorentz or Curie. In this context, it is no wonder that Léon Brillouin chose a scientific career, beginning with the *Ecole Normale Supérieure*. After his graduation, he spent a year in Munich, in Sommerfeld's laboratory, and, back to Paris, he began to work on the application of quantum theory to the solid state. The first World War, during which he was involved into wireless transmission, delayed the completion of his Ph.D. until 1920 [2]. Strangely, the last part of his thesis was not published at the time, but only two years later [3]; it includes the theoretical description of the effect that now bears his name.

During the 20's and the 30's, the scientific activity of Brillouin remained in the forefront of the extraordinary developments of the time, at the intersection of the dawning quantum theory and of the solid-state physics. In the attendants list of the famous 1927 Solvay conference, his name can be found next to those of Heisenberg, Pauli, Debye, Bragg, Dirac, Schrödinger, just to cite a few. His 1930 geometrical construction in the reciprocal space (figure A.1), both elegant and

1 Incidentally, personal recollection allows me to say that even the very pronunciation of this name seems to be unknown, at least for non french-speaking people in conferences.

insightful, was a major step in the comprehension of the electronic properties of crystals. In 1932, as his father retired, he took over his place at the *Collège de France*. At about the same time, and to further enhance his international reputation, the first experimental demonstration of the Brillouin effect was published by Debye and Sears[4].

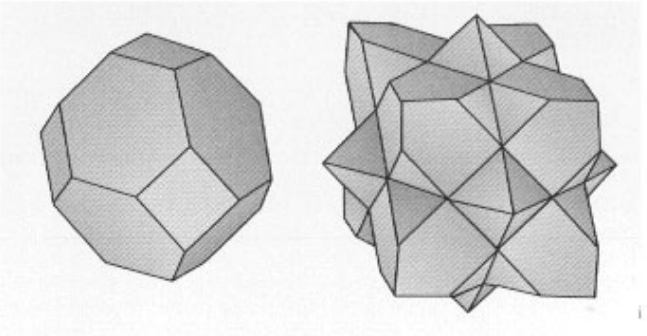

Figure A.1 First and second Brillouin zones of a face centered cubic crystal

His long-lasting interest in wireless transmission, going back to his WW I days, led Brillouin to a parenthesis in his scientific career. The circumstances made this break quite bitter. He was appointed head of the French national broadcasting in August 1939. In prevision of the threatening conflict with Germany, the French government recognized, though lately, the importance of the propaganda weapon, and Brillouin had to take care of the technical side of this effort. But neither the freshly installed new emitters of Brillouin nor the high-style speeches of dramatist Giraudoux, in charge of the information, - nor, by the way, the whole French army - could prevent the German tanks from invading the country. After the defeat in June 1940, Brillouin kept his position until May 1941, under the Vichy government; although he was on no account a collaborator of the occupying forces[1], this brought serious trouble to him after the liberation in 1945 : in the so-called purging process, over-zealous officials (or jealous colleagues ?) prevented him from getting back his pre-war position. In the meantime, he had emigrated to the USA and been actively involved in the war effort of various East-coast universities. Discouraged by the administrative difficulties he was facing in

1 In particular, he ordered the destruction of the emitters he was in charge of before their seizure by the enemy forces.

France, happily employed in Harvard and then by IBM, he eventually chose the US citizenship in 1949.

In the last, American part of his life, his interests shifted toward the links between entropy and information, the appearing computer sciences and the philosophy of sciences. He died in New York, on October 3rd 1969.

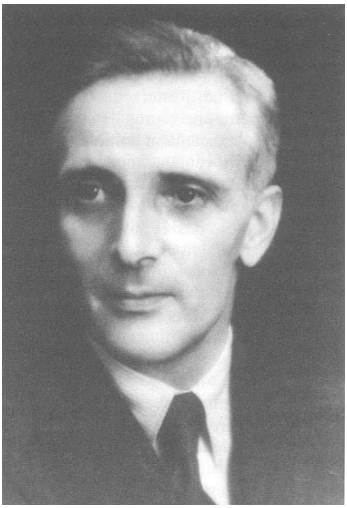

Figure A.2 Léon Brillouin in 1929

References

[1] *R. Mosseri*
Léon Brillouin, à la croisée des ondes
Un savant, une époque, Belin, Paris (1999).

[2] *L. Brillouin*
La théorie des solides et les quanta
Ph.D. Thesis Ecole Normale Supérieure, Paris (1920).

[3] *L. Brillouin*
Diffusion de la lumière et des rayons X par un corps transparent homogène : influence de l'agitation thermique
Annales de Physique, **17**, p. 88-122 (1922).

[4] *P. Debye, F.W. Sears*
On the scattering of light by supersonic waves
Proc. Nat. Acad. Sc., **18**, p. 409 (1932).

Annex 2

Phonons in crystalline materials

The aim of this appendix is to give a quick outline of the textbook presentation of vibration modes in crystals, after Ashcroft & Mermin [1] or Srivastava [2]. It will be helpful as a reference for the discussion of section 2-5 on the existence of phonons in amorphous solids.

Statement of the problem of lattice dynamics

From the outset, two important approximations are usually made :

- *the adiabatic approximation* : thanks to the large discrepancy in the masses of the ion cores and of the electrons, the motion of the latter can be treated separately. Actually, the electrons do not appear explicitly in the basic theory to which we restrict ourselves here[1].

- *the harmonic approximation* : only two-body interactions are considered, and the change in potential energy of any pair of atoms is quadratic in their respective displacement.

In a classical picture, the atoms of a crystal are represented by spheres joined by springs. The crystal dynamics is analyzed in terms of normal modes of vibration, that is of travelling wave of the form $A\exp[i(\mathbf{q}\,\mathbf{r}-\omega t)]$. The energies of the normal modes are quantized : for the q^{th} mode they are $\left(n_q + \frac{1}{2}\right)\hbar\omega(\boldsymbol{q})$, $n_q = 0, 1, 2, \ldots$ The quantum of energy $\hbar\omega$ is associated with an elementary excitation called a *phonon*[2]. The whole problem of lattice dynamics is to find the normal modes of a crystal; in other words, to calculate the energies (or frequencies) of the phonons as a function of their wave vector **q**. The relationship $\omega = \omega(\boldsymbol{q})$ is called *phonon dispersion*.

1. They become unavoidable, though, in any realistic model, since they play an essential role in shaping the potential landscape in which the ions move about.
2. The concept of a phonon is similar to that of a photon which is a quantum of energy in an electromagnetic field.

Dynamics of a monoatomic linear chain

The simplest imaginable system is the infinite one-dimensional chain of atoms represented in figure B.1. On top of the general approximations mentioned above, and to further simplify the situation, it is also assumed that only nearest-neighbor forces are significant.

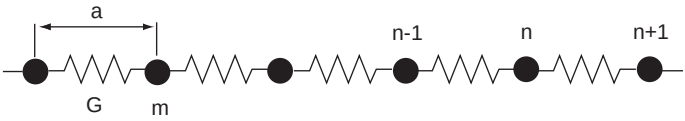

Figure B.1 A linear chain of N atoms of mass *m* linked by harmonic springs with constant *G*. The atoms are represented at their equilibrium position.

Suppose that at a particular time the n^{th} atom in the depicted chain has a displacement u_n from its equilibrium position. Then from Newton's second law and Hooke's law of springs, its equation of motion is

$$m\frac{d^2u_n}{dt^2} = G[(u_{n+1} - u_n) + (u_{n-1} - u_n)] \tag{B.1}$$

We take as trial solution

$$u_n = A\exp[i(qx - \omega t)] = A\exp[i(qna - \omega t)] \tag{B.2}$$

Here, *A* denotes the amplitude of the motion of the atom, and the wave "vector" *q* is scalar since the problem is unidimensional. With this, equation (B.1) becomes

$$\omega^2 A = \frac{2G}{m}(1 - \cos qa)A \tag{B.3}$$

For a non-trivial solution, this gives the following simple relation $\omega(q)$, plotted in figure B.2 :

$$\omega = 2\sqrt{\frac{G}{m}}\left|\sin\frac{qa}{2}\right| \tag{B.4}$$

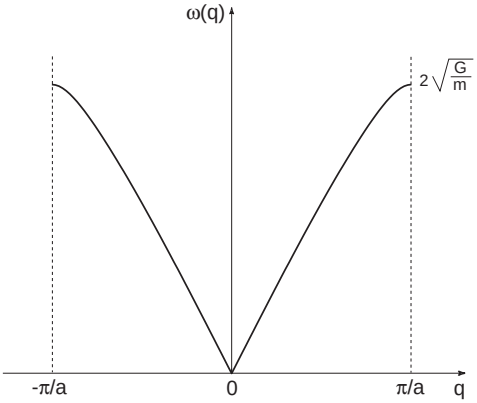

Figure B.2 Dispersion curve of the linear monoatomic chain of figure B.1 plotted in the first Brillouin zone.

Two types of velocity are defined for a phonon of wave vector q and frequency ω. $c_{p\,=\,\omega/q}$ is the phase velocity, while $c_g = (\partial\omega)/(\partial q)$ is the group velocity. Explicitly,

$$c_p = a\sqrt{\frac{G}{m}}\left(\frac{(\sin(qa/2))}{(qa/2)}\right), \text{ and } c_g = a\sqrt{\frac{G}{m}}\cos(qa/2) \qquad \text{(B.5)}$$

In the long-wavelength limit ($qa << 1$), $c_p = c_g = a\sqrt{\frac{G}{m}} = v$, where v is the sound velocity in the solid.

Dynamics of a diatomic linear chain

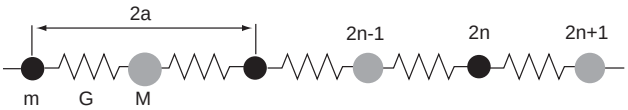

Figure B.3 A diatomic linear chain with alternating masses *m* and *M* (*m*<*M*) and spring constant *G*. The unit cell has length *2a*.

Now let us assume that the elementary cell of the lattice consists of two atoms with different masses *m* and *M* (*m* < *M*), the length and strength of the springs remaining unmodified. The equations of motion for the two types of atoms are

$$m\frac{d^2u_{2n}}{dt^2} = G[u'_{2n+1} + u'_{2n-1} - 2u_{2n}] \tag{B.6}$$

$$M\frac{d^2u'_{2n+1}}{dt^2} = G[u_{2n+2} + u_{2n} - 2u'_{2n+1}] \tag{B.7}$$

As before, we try travelling waves solutions of the form

$$\begin{aligned} u_{2n} &= A_1 \exp[i(2nqa - \omega t)] \\ u'_{2n+1} &= A_2 \exp[i((2n+1)qa - \omega t)] \end{aligned} \tag{B.8}$$

The ratio of the constants to be determined A_1 and A_2 will specify the relative amplitude and phase of the vibration of the ions within each primitive cell. With (B.8), (B.6) and (B.7) can be rewritten as the system of coupled equations

$$\omega^2 \begin{bmatrix} A_1 \\ A_2 \end{bmatrix} = \begin{bmatrix} 2G/m & -(2G/m)\cos qa) \\ -(2G/M)\cos qa) & 2G/M \end{bmatrix} \begin{bmatrix} A_1 \\ A_2 \end{bmatrix} \tag{B.9}$$

whose non-trivial solutions are

$$\omega^2 = G\left(\frac{1}{m} + \frac{1}{M}\right) \pm G\left[\left(\frac{1}{m} + \frac{1}{M}\right)^2 - \frac{4}{mM}\sin^2 qa\right]^{1/2} \tag{B.10}$$

Corresponding to the two signs in (B.10), there are two branches of the phonon dispersion curves plotted in figure B.4. To understand their physical meaning, the ratio A_1/A_2 will be useful.

$$\frac{A_1}{A_2} = \frac{2G\cos qa}{2G - m\omega^2} = \frac{2G - M\omega^2}{2G\cos qa} \tag{B.11}$$

Let us examine the solutions in the long-wavelength ($qa << 1$) limit. For the lower branch, $A_1/A_2 = 1$; both atoms in the unit cell move in phase with each other. This is fully comparable with the case of the monoatomic chain and is characteristic of a sound wave, hence its name of *acoustic* branch. For the upper branch, it is easy to verify that A_1 and A_2 have opposite signs, meaning that the two atoms in the unit cell move in opposite directions. Such a mode of vibration could be excited by an electric field of the appropriate frequency, provided that

the atoms carry opposite charges. For most crystals, this appropriate frequency turns out to lie in the infrared or visible range of the electromagnetic spectrum, justifying the terminology of *optical* phonons.

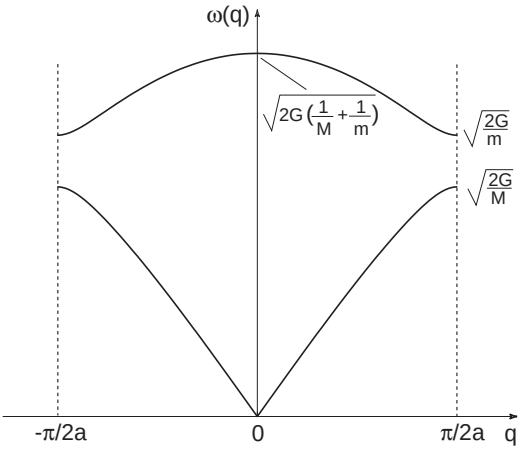

Figure B.4 The phonon dispersion spectrum of the diatomic linear chain plotted in the first Brillouin zone. The lower curve is the acoustic branch, the upper one the optical branch.

The difference between optical and acoustic modes of vibration becomes less clear for other values of *q*. Nevertheless, the following distinction makes sense in general, at least to give a first intuitive insight of what happens in more complex cases : an acoustic mode is one in which all atoms within a primitive cell move essentially in phase, as a whole, and the dynamics is dominated by interactions between cells; on the other hand, an optical mode is essentially a molecular vibratory mode within each primitive cell, which is broadened out into a band of frequencies by virtue of the intercellular interactions.

Dispersion curves of real 3-D crystals

In the three-dimensional case, considerable difficulties arise in the notation and the visualization of the dispersion curves, but there is nothing conceptually new with respect to the diatomic chain of the preceding paragraph. There are as many branches in the dispersion curves as there are degrees of liberty in the basic cell of the crystal. An example is shown in figure B.5 : for a crystal of bismuth, with two atoms in the unit cell, 3 acoustic and 3 optical modes exist. Here they are only represented along a particular path in the first Brillouin zone. A full picture

should give the frequencies ω corresponding to every 3D-wave vector $\boldsymbol{q}$ in the Brillouin zone. Both optical and acoustic branches can be further subdivided into *longitudinal* or *transverse* modes, depending on the respective directions of their eigenvectors and of $\boldsymbol{q}$, although the lattice vibrations are strictly longitudinal or transverse only at a few, high-symmetry points of the Brillouin zone.

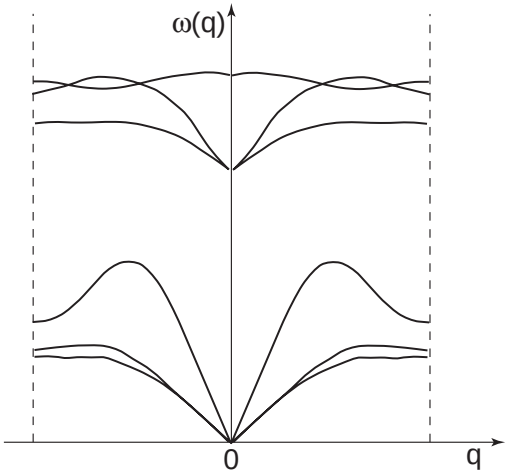

Figure B.5 Phonons dispersion curves along the direction [100] (or Γ-X) in the bismuth at 77 K. [3]

Density of states in crystals

The phonon dispersion curves are fundamental in the study of crystalline materials but, as showed in section 2.5.1, they become pretty useless in amorphous solids. The single most useful quantity to explain physical properties of both crystalline and non-crystalline materials is the density of normal modes $g(\omega)$, which is defined as the number of vibration modes between frequencies ω and ω+dω (or equivalently between wave vectors $\boldsymbol{q}$ and $\boldsymbol{q}$+d$\boldsymbol{q}$).

$$g(\omega) = \sum_s \int \frac{1}{2\pi^3} \delta(\omega - \omega_s(\boldsymbol{q})) d\boldsymbol{q} \qquad \text{(B.12)}$$

The sum has to be taken over all phonon polarizations, and the integral is the limit for an infinite lattice of the number of vectors $\boldsymbol{q}$ on the constant frequency surface $\omega = \omega_s(\boldsymbol{q})$. A more useful form of (B.12) is

$$g(\omega) = \sum_s \int \frac{1}{2\pi^3} \frac{1}{|\nabla \omega_s(\boldsymbol{q})|} dS \qquad \text{(B.13)}$$

Reflecting the fact that the phonon group velocity appears in the denominator of (B.13), the density of states exhibits singularities for frequencies where this velocity approaches (or is) zero in one branch of the dispersion curves. These are known as Van Hove singularities and are clearly visible in the figure B.6

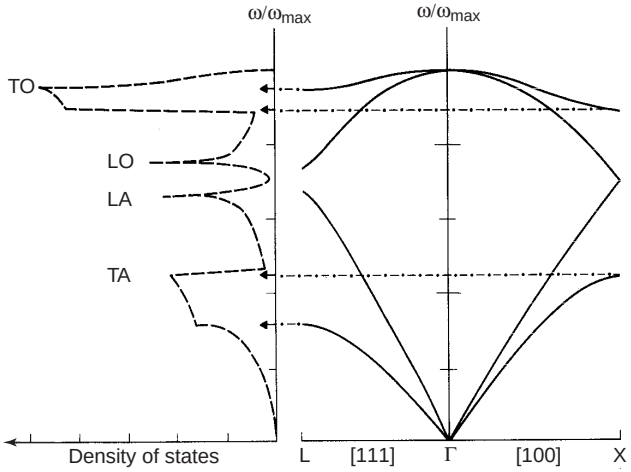

Figure B.6 Density of states (left) and phonon dispersion curves (right) for diamond cubic Si (or Ge), after [4]. The dotted lines indicate the origin in reciprocal space of some Van Hove singularities. Due to the degeneracy of the transverse branches, only four dispersion curves are visible.

References

[1] *N.W. Ashcroft, N.D. Mermin*
Solid state physics
Saunders, Philadelphia (1976).

[2] *G.P. Srivastava*
The physics of phonons
Adam Hilger, Bristol (1990).

[3] *G. Dolling*
Neutron spectroscopy
in *Dynamical properties of solids*, G.K. Horton and A.A. Maradudin, Editors, North Holland, Amsterdam (1980).

[4] *S.R. Elliott*
Physics of amorphous materials
Longman Inc., New York (1983).

Annex 3

List of acronyms

BGS	Brillouin-gain spectrum
CRN	continuous random network
DFB	distributed feedback (laser diode)
DFG	difference-frequency generation
DiTeSt	distributed temperature and strain analyzer
DOS	(vibrational) density of states
EDFA	erbium-doped fiber amplifier
EOM	electro-optic modulator
FWHM	full-width at half-maximum
FWM	four-wave mixing
INS	inelastic neutron scattering
IRS	infrared spectroscopy
LASBI	local analysis of stimulated Brillouin interaction
LHC	large-hadron collider
MCVD	modified chemical vapor deposition
MRO	medium-range order
OTDR	optical time-domain reflectometry
PC	polarization controller
RDF	radial distribution function
SBS	stimulated Brillouin scattering
SFG	sum-frequency generation
SHG	second-harmonic generation
SRO	short-range order
SRS	stimulated Raman scattering
TLS	two-level system

Remerciements

Ce travail a été réalisé pour l'essentiel au Laboratoire de Métrologie de l'EPFL, sous la responsabilité du Professeur Philippe Robert. Je le remercie sincèrement de m'avoir accueilli dans son équipe, me permettant ainsi d'effectuer cette thèse.

Toute ma gratitude va à Luc Thévenaz, qui m'a guidé et soutenu au cours de ces années. Elle va aussi à Walter Scandale, de la division Technologie des Accélérateurs du CERN, à qui revient le mérite d'avoir proposé les mesures en cryogénie et d'avoir permis leur réalisation.

J'ai eu la chance de pouvoir compter sur le soutien administratif, technique et humain de nombreuses personnes. Ce sont entre autres à Genève Juan Garcia Perez, qui a rendu possibles les mesures sur les aimants du LHC, et toute l'équipe du Cryolab, en particulier Giovanna Vandoni. A Lausanne, je devrais citer tous les membres passés et présents du MET; en voici la liste, au risque d'en oublier : Danielle Alvarez, Kamiar Aminian, Fabien Briffod, Caroline Brisson, Paolo Dainesi, Hooman Dejnabadi, Anne-Isabelle Desmangles, Jean Gramiger, Anisoara Ionescu, Pierre Jacquot, Alain Küng, Sébastien Le Floch, Pascal Morel, Bijan Najafi, Marianne Noè, Juraj Poliak, Arash Salarian, Jörg Troger. Un merci plus appuyé à mon colocataire de bureau Stéphane Schilt, ainsi qu'à Marc Niklès, premier prophète de Brillouin dans notre groupe, et Massimo Facchini, compagnon de laboratoire et de terrain.

Je ne saurais conclure sans mentionner tout ce que je dois à mes parents, dont les encouragements constants m'accompagnent depuis quelques décennies déjà, et à mes frères et soeurs. Je leur dédie cet ouvrage.

Enfin, une pensée particulière va évidemment à Angelika. Parmi les milliers de raisons que j'ai de la remercier, je ne citerai que la patience qui lui a permis de supporter la concurrence chronophage de Léon Brillouin ces derniers mois.

CV

FELLAY Alexandre

Rue du Maupas 13
1004 Lausanne
Suisse
021/693 56 04
079/745 08 41
E-mail : alexandre.fellay@epfl.ch

Ingénieur physicien diplômé EPFL
spécialisé en optique

Nationalité suisse
Né le 8 mars 1973 à Orsières (Valais)
Célibataire

Formation

1991-1996	Ecole Polytechnique Fédérale de Lausanne Diplôme d'ingénieur physicien
1986-1991	Collège de l'Abbaye de Saint-Maurice Maturité type Latin-Grec, avec option sciences

Expérience professionnelle

2002	*CERN* (Genève) Doctorant stagiaire au sein du groupe Main Magnet Systems
1996-2001	*ECOLE POLYTECHNIQUE FÉDÉRALE DE LAUSANNE* Assistant, puis assistant-doctorant au Laboratoire de Métrologie du Département d'Electricité. Recherche et développement dans le domaine des capteurs à fibre optique, y compris applications dans le génie civil et environnemental. Auteur d'une dizaine de publications présentées à des conférences internationalesd'optique. Supervision de plusieurs projets d'étudiants. Responsable du support informatique pour le Laboratoire.

Langues

Français	Langue maternelle
Anglais	Parlé et écrit : très bon niveau
Allemand	Parlé et écrit : bon niveau
Italien	Parlé et écrit : bases
Russe	Ecrit : bases

Centres d'intérêts extra-professionnels

Chant classique, en tant que membre voire président de choeurs, et en soliste
Littérature en général, histoire
Ski de randonnée, montagne, course à pied

List of publications

[1] *A. Fellay, F. Gagel, K. Maschke, A. Virlouvet, A. Khater*
Scattering of vibrational waves in perturbed quasi-one-dimensional multichannel waveguides
Phys. Rev. B, **55**(3), p. 1707-1717 (1997).

[2] *A. Fellay, L. Thévenaz, M. Facchini, M. Niklès, P.A. Robert*
Distributed sensing using stimulated Brillouin scattering : toward ultimate resolution
Proc. of the 12th Conference on Optical Fiber Sensors, Williamsburg Virginia, p. 324-327 (1997).

[3] *L. Thévenaz, M. Facchini, A. Fellay, M. Niklès, P.A. Robert*
Evaluation of local birefringence along fibers using Brillouin analysis
Proc. of the 4th Optical Fibre Measurement Conference, Teddington UK, p. 82-85 (1997).

[4] *M. Niklès, L. Thévenaz, A. Fellay, M. Facchini, P. Salina, P.A. Robert*
A novel surveillance system for installed fiber optics cables using stimulated Brillouin interaction
Proc. of the 46th International Wire and Cable Symposium, Philadelphia, p. 658-664 (1997).

[5] *L. Thévenaz, M. Niklès, A. Fellay, M. Facchini, P.A. Robert*
Truly distributed strain and temperature sensing using embedded optical fibers
Proc. of the SPIE International Symposium on Smart Structures and Materials, San Diego, p. 301-314 (1998).

[6] *A. Fellay, L. Thévenaz, M. Facchini, P.A. Robert*
Limitation of Brillouin time-domain analysis by Raman scattering
Proc. of the 5th Optical Fibre Measurement Conference, Nantes, France, p. 110-113 (1999).

[7] *M. Facchini, L. Thévenaz, A. Fellay, P.A. Robert*
Tensile tests on optical fibre cables using distributed Brillouin analysis
Proc. of the 5th Optical Fibre Measurement Conference, Nantes, France, p. 106-109 (1999).

[8] *L. Thévenaz, M. Facchini, A. Fellay, P.A. Robert, D. Inaudi, B. Dardel*
Monitoring of large structures using distributed Brillouin fibre sensing
Proc. of the 13th Conference on Optical Fiber Sensors, Kyongju, Korea, p. 345-348 (1999).

[9] *L. Thévenaz, M. Facchini, A. Fellay, M. Niklès, P.A. Robert*
Field tests of distributed temperature and strain measurement for smart structures
Proc. of the 4th Pacific Rim Conference on Lasers and Electro-Optics, Chiba, Japan, p. 490-491 (2001).

[10] *A. Fellay, S. Le Floch, M. Facchini, L. Thévenaz, W. Scandale, P.A. Robert*
Brillouin gain curve measurements in fibers at cryogenic temperatures (3 K-140 K)
Proc. of the 6th Optical Fibre Measurement Conference, Cambridge UK, p. 55-58 (2001).

[11] *L. Thévenaz, A. Fellay, M. Facchini, W. Scandale, M. Niklès, P.A. Robert*
Brillouin optical fiber sensor for cryogenic thermometry
Proc. of the Conference on Smart Sensors Technology, San Diego, California, p. 22-27 (2002)

[12] *A. Fellay, L. Thévenaz, J. Garcia Perez, W. Scandale, M. Facchini, P.A. Robert*
Brillouin-based temperature sensing in optical fibers down to 1 K
Proc. of the 15th Conference on Optical Fiber Sensors, Portland, Oregon, p.301-304, (2002).